Optical Properties of the Chalcopyrite Semiconductors $CuInSe_2$, $CuInS_2$ and $CuGaSe_2$

Franziska Luckert

A thesis presented in partial fulfillment
of the requirements for the degree of
Doctor of Philosophy

Department of Physics
University of Strathclyde

April 2012

This thesis is the result of the author's original research. It has been composed by the author and has not been previously submitted for examination which has lead to the award of a degree.

The copyright of this thesis belongs to the author under the terms of the United Kingdom Copyright Acts as qualified by University of Strathclyde Regulation 3.50. Due acknowledgment must always be made for the use of any material contained in, or derived from, this thesis.

Signed: Date:

Abstract

$CuInSe_2$, $CuInS_2$ and $CuGaSe_2$ are I-III-VI_2 compound semiconductors with a chalcopyrite structure. These ternary compounds exhibit favourable properties, such as direct band gaps and high absorption coefficients, for application as absorber layers in thin-film solar cells. Recently Cu(In,Ga)Se_2 based photovoltaic devices have demonstrated conversion efficiencies of 20.3 % which is the highest amongst polycrystalline thin-film solar cell technologies. This thesis describes a study of excitonic recombination processes in high quality $CuInSe_2$, $CuInS_2$ and $CuGaSe_2$ single crystals using photoluminescence (PL) spectroscopy as a function of excitation power, temperature and applied magnetic field. Excitation power dependent measurements confirm the identification of the free excitons in the PL spectra of the three chalcopyrite semiconductor compounds. Additional sharp lines in the PL spectra appear to be due to the radiative recombination of excitons bound to shallow hydrogenic defects. PL lines due to excitons bound to more complex defects with a low concentration of defects are also found in $CuInSe_2$ and $CuInS_2$. Analysis of the temperature dependent PL spectra lead to activation energies of the free and bound excitons in $CuInSe_2$, $CuInS_2$ and $CuGaSe_2$. In addition, phonon energies have been obtained from the temperature dependence of the free exciton spectral positions and of the full width at half maximum. PL spectra measured in applied magnetic fields allow estimation of the diamagnetic shift rates for $CuInSe_2$, $CuInS_2$ and $CuGaSe_2$. A first-order perturbation model leads to values for the excitonic reduced masses and the effective hole masses can be estimated. For $CuInSe_2$ a theoretically predicted anisotropy of the effective hole masses is demonstrated. The study of the excitonic states in $CuInSe_2$, $CuInS_2$ and $CuGaSe_2$ provides a deeper understanding of the electronic material properties which can facilitate further improvements in solar cell efficiencies.

Acknowledgments

There are many people who have contributed to this work and I would like to thank them for their help and encouragement.
This work would not have been possible without the guidance, patience and instructions of my supervisor Prof. Robert Martin. His support and encouragement have helped me through the completion of my research.
I am also grateful to Dr. Michael Yakushev for his introduction and guidance through the world of chalcopyrite semiconductors. In addition, I would like to thank him for his help and feedback on the analysis of the spectra as well as for his expertise and company throughout the stays at the GHMFL.
Thank you to Prof. Kevin O'Donnell for his advice and suggestions regarding my research. I also have to thank Dr. Clement Faugeras for his help and expertise throughout the experiments at the GHMFL.
In addition, I would like to say thank you to Paul for his help with the EPMA, CL and the SEM.
I am also grateful to all colleagues I shared my studies with: Lethy, Nils and Michael for their patience listening to my ideas and thoughts as well as for the good atmosphere. Thank you to Jochen, Carol and Naresh for their company, discussions and several coffee breaks on level 2.
I would like to thank Dave for his company as well as for his help with the setups and microscopes.
Last but not least, I would like to say thanks to all my friends which supported me during my PhD, especially Line and Mariana. Thank you to my parents, grandparents, Aileen and Douglas for their guidance and support in all situations.
To Richard, thank you for your patience, support and belief in me.
Thank you to all involved and apologies to anyone not mentioned by name.

List of Publications

1. F. Luckert, M. V. Yakushev, C. Faugeras, A. V.Karotki, A. V. Mudryi, R. W. Martin, "Excitation power and temperature dependence of excitons in $CuInSe_2$", J. Appl. Phys. **111** (2012) 093507

2. R. E. L. Powell, S. V. Novikov, F. Luckert, P. R. Edwards, A. V. Akimov, C. T. Foxon, R. W. Martin, A. J. Kent, "Carrier localization and related photoluminescence in cubic AlGaN epilayers", J. Appl. Phys. **110** (2011) 063517

3. H. Zachmann, S. Puttnins, M. V. Yakushev, F. Luckert, R. W. Martin, A. V. Karotki, V. F. Gremenok, A. V. Mudryi, "Fabrication and characterisation of $Cu(In,Ga)Se_2$ solar cells on polyimide" Thin Solid Films **519** (2011) 7264

4. F. Luckert, D. I. Hamilton, M. V. Yakushev, N. S. Beattie, G. Zoppi, M. Moynihan, I. Forbes, A. V. Karotki, A. V. Mudryi, M. Grossberg, J. Krustok, R. W. Martin, "Optical properties of high quality $Cu_2ZnSnSe_4$ thin films", Appl. Phys. Lett. **99** (2011) 062104

5. S. V. Novikov, C. R. Staddon, C. T. Foxon, K. M. Yu, R. Broesler, M. Hawkridge, Z. Liliental-Weber, J. Denlinger, I. Demchenko, F. Luckert, P. R. Edwards, R. W. Martin, W. Walukiewicz, "Growth by molecular beam epitaxy of amorphous and crystalline GaNAs alloys with band gaps from 3.4 to 0.8 eV for solar energy conversion devices", J. Cryst. Growth **323** (2011) 60

6. S. V. Novikov, C. R. Staddon, C. T. Foxon, F. Luckert, P. R. Edwards, R. W. Martin, A. J. Kent, "Molecular beam epitaxy as a method for the growth of free-standing bulk zinc-blende GaN and AlGaN crystals", J. Cryst. Growth **323** (2011) 80

7. M. V. Yakushev, F. Luckert, C. Faugeras, A. V. Karotki, A. V. Mudryi, R. W. Martin, "Excited States of the A and B Free Excitons in $CuInSe_2$", Jpn. J. Appl. Phys. **50** (2011) 05FC03

8. S. V. Novikov, C. R. Staddon, R. E. L. Powell, A. V. Akimov, F. Luckert, P. R. Edwards, R. W. Martin, A. J. Kent, C. T. Foxon, "Wurtzite $Al_xGa_{1-x}N$ bulk crystals grown by molecular beam epitaxy", J. Cryst. Growth **322** (2011) 23

9. A. V. Karotki, A. V. Mudryi, M. V. Yakushev, F. Luckert, R. W. Martin, "Structural and Optical Properties of CdS/Cu(In,Ga)Se_2 Heterostructures Irradiated by High-Energy Electrons", J. Appl. Spectr. **77** (2010) 668

10. F. Luckert, M. V. Yakushev, C. Faugeras, A. V. Karotki, A. V. Mudryi, R. W. Martin, "Diamagnetic shift of the A free exciton in CuGaSe(2) single crystals", Appl. Phys. Lett. **97** (2010) 162101

11. M. V. Yakushev, F. Luckert, C. Faugeras, A. V. Karotki, A. V. Mudryi, R. W. Martin, "Excited states of the free excitons in $CuInSe_2$ single crystals", Appl. Phys. Lett. **97** (2010) 152110

12. A. V. Mudryi, V. F. Gremenok, A. V. Karotki, V. B. Zalesski, M. V. Yakushev, F. Luckert, R. W. Martin, "Structural and optical properties of thin films of Cu(In,Ga)Se_2 semiconductor compounds", J. Appl. Spectr. **77** (2010) 371

13. K. M. Yu, S. V. Novikov, R. Broesler, I. N. Demchenko, J. D. Denlinger, Z. Liliental-Weber, F. Luckert, R. W. Martin, W. Walukiewicz, C. T. Foxon, "Highly mismatched crystalline and amorphous $GaN_{1-x}As_x$ alloys in the whole composition range", J. Appl. Phys. **106** (2009) 103709

14. M. V. Yakushev, F. Luckert, A. V. Rodina, C. Faugeras, A. V. Karotki, A. V. Mudryi, R. W. Martin, "Anisotropy of Effective Masses in $CuInSe_2$", in preparation

Contents

1 Introduction **1**

2 Background **9**

2.1 Crystal and Electronic Structure 9

2.1.1 Crystal Structure 9

2.1.2 Electronic Structure 11

2.2 Defects 16

2.3 Excitons 17

2.3.1 Free Excitons 19

2.3.2 Bound Exciton 19

2.4 Photoluminescence 20

2.4.1 Excitonic Line Shapes 21

2.4.2 Temperature Induced Quenching of Excitonic Lines 22

2.4.3 Excitation Power Dependence of Excitonic Lines 26

2.5 Excitons in Magnetic Fields 27

2.5.1 Diamagnetic shift of excitons 27

2.5.2 Zeeman Splitting 28

2.6 Polaritons 28

3 Experimental Techniques **31**

3.1 Sample Growth 31

3.1.1 Bridgman Method 31

3.1.2 Travelling Heater Method 32

3.2 X-Ray Crystal Orientation: Laue Method 32

3.3 Energy Dispersive X-Ray Spectroscopy 33

3.4 Photoluminescence Spectroscopy 34

3.4.1 PL-Set-up Strathclyde 35

3.4.2 PL-Set-up GHMFL 36

4 $CuInSe_2$ **39**
4.1 Excitons in $CuInSe_2$ . . . 39
4.2 Excitation Power Dependence . . . 43
4.2.1 Excitation Power Dependence of the Intensity . . . 43
4.3 Temperature Dependence . . . 47
4.3.1 Temperature Dependence of the Spectral Position of the A and B free excitons . . . 48
4.3.2 Temperature Dependence of the Intensity . . . 51
4.3.3 FWHM as a Function of Temperature . . . 56
4.4 Magneto-Photoluminescence of $CuInSe_2$ . . . 59
4.4.1 Diamagnetic Shift in an Anisotropic Crystal . . . 63
4.4.2 Effective Hole Masses In $CuInSe_2$ . . . 65
4.5 Summary . . . 67

5 $CuInS_2$ **69**
5.1 Excitons in $CuInS_2$ . . . 69
5.2 Excitation Power Dependence . . . 76
5.2.1 Emission Intensity as a Function of Excitation Power . . . 76
5.3 $CuInS_2$ Temperature Dependence . . . 79
5.3.1 Spectral Position of the A Free Exciton as a Function of Temperature . . . 80
5.3.2 Temperature Quenching of the Exciton PL Intensity . . . 85
5.3.3 FWHM as a Function of Temperature . . . 91
5.4 Magneto-Photoluminescence of $CuInS_2$ . . . 92
5.4.1 Diamagnetic Shift of Polaritons in $CuInS_2$ . . . 94
5.5 Summary . . . 97

6 $CuGaSe_2$ **98**
6.1 Excitons in $CuGaSe_2$ . . . 98
6.2 Excitation Power Dependent Photoluminescence . . . 101
6.2.1 Integrated Emission Intensity as a Function of Excitation Power . . . 101
6.3 Temperature Dependent Photoluminescence . . . 103
6.3.1 Spectral Position of the A exciton as a Function of Temperature . . . 103
6.3.2 Integrated Emission Intensity as a Function of Temperature 105

6.3.3 FWHM as a Function of Temperature 108
6.4 Magneto-Photoluminescence of $CuGaSe_2$ 109
6.4.1 Diamagnetic Shift of the A Free Exciton in $CuGaSe_2$ . . . 110
6.5 Summary 112

7 Discussion and Summary **113**
7.1 Excitation Power Dependent PL 113
7.2 Temperature Dependent PL 115
7.2.1 Temperature Dependence of the Spectral Position 115
7.2.2 Temperature Quenching of the Exciton PL Intensity 116
7.2.3 Temperature Dependence of the FWHM 118
7.3 Magneto-Photoluminescence 119
7.4 Future Work 121

List of Abbreviation/Acronyms

BE	Bound exciton
$CuIn_{1-x}Ga_xSe_2$	CIGS
DAP	Donor-acceptor pair
FE	Free exciton
FWHM	Full width at half maximum
LPB	Lower Polariton Branch
PL	Photoluminescence
THM	Travelling Heater Method
UPB	Upper Polariton Branch
RF	Reflectivity

Chapter 1

Introduction

$CuInSe_2$, $CuInS_2$ and $CuGaSe_2$ are I-III-VI_2 compound semiconductors that crystallise with a chalcopyrite structure. They exhibit favourable properties for application as absorber layers in thin film solar cells, such as a direct band gap and high absorption coefficients. Conversion efficiencies for $CuInSe_2$, $CuInS_2$ and $CuGaSe_2$ have been reported as ∼14 [1], ∼12 [2] and ∼10% [3], respectively. The $CuInS_2$ band gap of ∼1.55 eV is almost ideally matched to the solar spectrum. In contrast, the efficiency of $CuInSe_2$ (band gap of ∼1.05 eV) can be improved by alloying it with Ga to form $CuIn_{1-x}Ga_xSe_2$ (CIGS) which increases the band gap to ∼1.7 eV for x=*1*. The highest efficiencies of 20.3 % for CIGS-based solar cells were obtained by Zentrum für Sonnenenergie- und Wasserstoff-Forschung (ZSW) in Germany [4]. This efficiency is currently the highest amongst the thin-film photovoltaic technologies.

A typical single junction solar cell is basically a pn-junction with no voltage directly applied across the junction. It converts photon power into electrical power and delivers the power to a load. An energy band diagram of a pn-junction under solar radiation is shown in Fig. 1.1. Incident photons can create electron-hole pairs in the space charge region which will be swept out producing the photocurrent I_L in the reverse-bias direction. The photocurrent I_L produces a voltage (V) drop across across the resistive load which forward biases the pn-junction and a forward-bias current I_F is produced. The net pn-junction current, in reverse-bias direction, is given by [6, 7]):

$$I = I_L - I_F = I_L - I_S \left(e^{qV/kT} - 1\right) \tag{1.1}$$

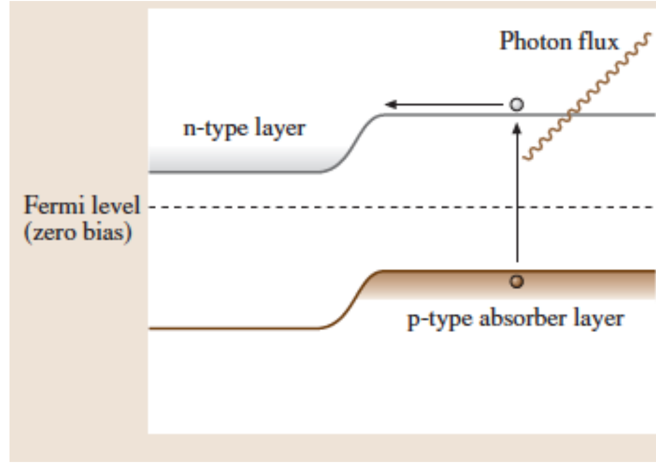

Figure 1.1: Schematic of an energy band diagram for a pn-junction solar cell, showing the absorption of a photon and the subsequent creation of an electron-hole pair which diffuses towards the pn-junction, taken from [5].

where I_S is the saturation current, q the elemental charge, k the Boltzmann constant and T the temperature. The saturation current I_S is given by:

$$I_S = AqN_C N_V \left(\frac{1}{N_A} \sqrt{\frac{D_n}{\tau_n}} + \frac{1}{N_D} \sqrt{\frac{D_p}{\tau_p}} \right) e^{-E_g/kT} \tag{1.2}$$

where A is the device area, N_C and N_V are the effective density of states in the conduction and valence band, N_D and N_A the donor and acceptor densities, D_n and D_p the electron and hole diffusion coefficients ($D_{n,p} = \left(\frac{kT}{q}\right) \mu_{n,p}$, where $\mu_{n,p}$ is the mobility of the electrons and holes) , τ_n and τ_p the minority carrier lifetime for electrons and holes and E_g the band gap of the solar cell absorber layer. Fig. 1.2 shows the J-V curve (J=I/A is the current density) of a solar cell under illumination. By properly choosing a load, close to 80 % of the product $J_{SC}V_{OC}$ (J_{SC} short-circuit current density) can be extracted. The short-circuit condition occurs when the load R_L=0 so that the voltage is equal to zero. The current in this case is referred to as the short-circuit current I_{SC}:

$$I = I_{SC} = I_L \tag{1.3}$$

The open-circuit condition occurs when $R_L \to \infty$. Then the net current is zero and the voltage produced is the open-circuit voltage V_{OC}:

$$I = 0 = I_L - I_S \left(e^{qV_{OC}/kT} - 1 \right) \tag{1.4}$$

The open-circuit voltage is then given by:

$$V_{OC} = \frac{kT}{q} ln \left(\frac{I_L}{I_S} + 1 \right) \tag{1.5}$$

For the ideal diode characteristics (Eq. 1.1) the power P is given by the following:

$$P = IV = I_L V - I_S V \left(e^{qV/kT} - 1 \right) \tag{1.6}$$

The condition for maximum power can be obtained when dP/dV=0. The maximum power output P_m, shaded area in Fig. 1.2, is then given by:

$$P_m = I_m V_m = I_L \left[V_{OC} - \frac{kT}{q} ln \left(1 + \frac{qV_m}{kT} \right) - \frac{kT}{q} \right] = I_L \left(E_m / q \right) \tag{1.7}$$

where E_m is the energy corresponding to the maximum energy that can be

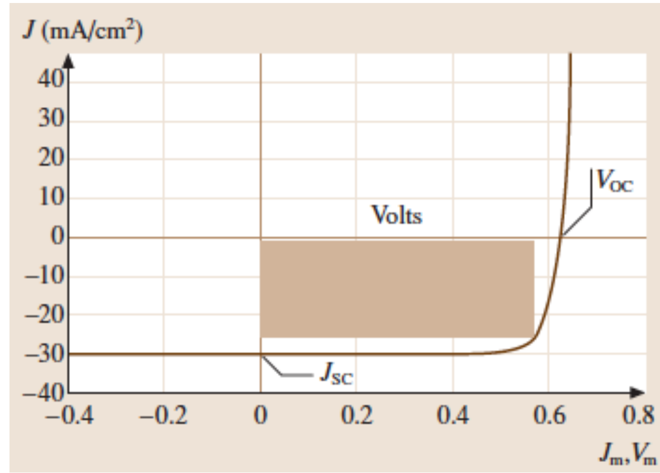

Figure 1.2: Ideal J-V characteristics for a solar cell according to Eq. 1.1 with J_S=30 mA/cm^{-2}, taken from [5]. The short-circuit current density J_{SC} and the open-voltage voltage V_{OC} are shown on the J-V curve. The maximum extracted power corresponds to the shaded area under the curve.

extracted per photon. The maximum power P_m and energy E_m both depend on I_L and I_S. For a given semiconductor I_S can be obtained from Eq. 1.2 whereas I_L can be obtained from the integration of solar spectrum for photon energies ranging from E_g to ∞. Once I_L and I_S are know, E_m can be calculated. Since I_S and therefore E_m depend on material properties such as the charge carrier lifetime τ, the diffusion coefficient D and therefore the mobility μ as well as the doping levels, the ideal efficiency corresponds to an optimum choice of material properties [7].

The conversion efficiency of a solar cell is defined as the ratio of output electric power P_m to incident optical power P_{in} [6, 7]:

$$\eta = \frac{P_m}{P_{in}} = \frac{I_L(E_m/q)}{P_{in}} = \left[V_m^2 I_S(q/kT)e^{qV_m/kT}\right]/P_{in} \tag{1.8}$$

P_m also depends on the maximum energy E_m that can be extracted per photon which in turn depends on the band gap of the semiconductor absorber layer. When a single junction solar cell is exposed to the solar spectrum, a photon with energy less than the band gap energy will have no effect on the electrical output power of the solar cell. Whereas a photon with energy larger than the band gap energy of the semiconductor will contribute to the output power. The fraction of the photon energy that is greater than the band gap energy will be dissipated as heat. The function of efficiency for semiconductors with different band gap energies is shown in Fig. 1.3. Fig. 1.3 shows that the highest efficiency of a single-junction solar cell occurs for semiconductors with a band gap in the near-infrared region around 1.2 to 1.5 eV. The maximum efficiency is predicted for Si, InP, GaAs and CdTe which are in the region of 30 % for 1.5 AM (solar radiation reaching the ground when the sun is at an angle of 45°) radiation [5].

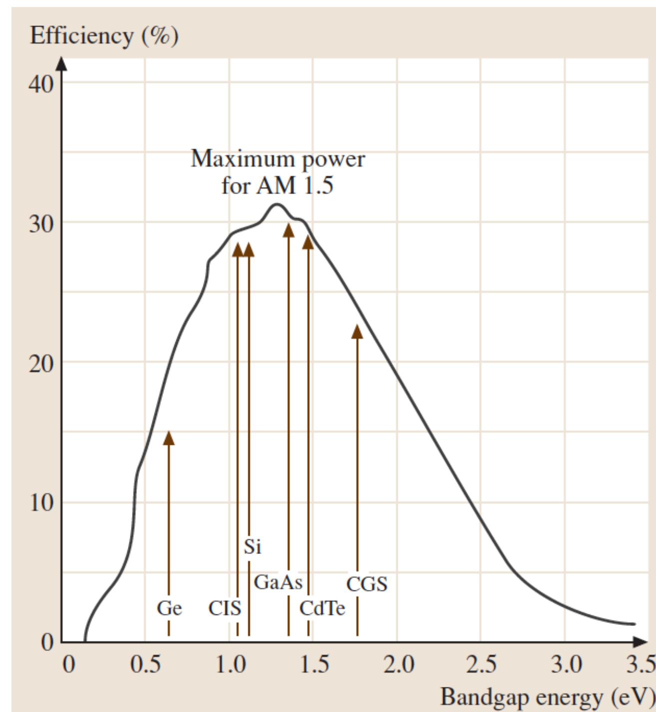

Figure 1.3: Ideal efficiency against band gap energy for a single-junction cell for AM 1.5 illumination conditions, taken from [5] after [8]. CIS and CGS are the abbreviations for $CuInSe_2$ and $CuGaSe_2$, repectively.

Current PV production is dominated by single-junction solar cells based on Si-wafers including single crystal and polycrystalline silicon with efficiencies of 25 and 20 % [9], respectively. Si-based solar cells, including crystalline, polycrystalline and amorphous silicon, account for nearly 90 % of the 2011 sales of photovoltaic products [1]. The disadvantage of crystalline and polycrystalline Si is the low absorption coefficient due to its indirect band gap. This requires material thickenesses in excess of 100 μm to absorb the solar radiation greater than the band gap energy. Using polycrystalline Si instead of crystalline can help to cut the costs. However, the grain boundaries cause the wafer to be mechanically weaker which results in a larger absorber thickness of about 300 μm. In addition, the grain boundaries can cause some loss of efficiency [5].
Thin-film technologies can provide a way of decreasing the costs. The aim is to use less material while still maintaining the efficiencies [10]. Thin-film technologies include amorphous-Si, CdTe and $Cu(Ga,In)Se_2$. These technologies work because these materials absorb the solar spectrum more efficiently than crystalline and polycrystalline Si due to their direct band gap and require only 1-10 μm thick active regions. Currently the efficiencies of amorphous-Si, CdTe and CIGS are $\sim$10 %, $\sim$16.7 % [9] and 20.3 % [4], respectively.
This chapter concentrates on single-junction solar cells. However, GaInP/GaAs/Ge triple-junction solar cells have shown conversion efficiencies of $\sim$32 % [9] but are too expensive for terrestrial applications. Concentrators, in which the solar radiation is optically concentrated onto the PV cells and the collection area can be much greater than the area of the expensive PV module, can provide the opportunity for terrestrial applications of these solar cells [5]. An illustration of the best efficiencies for various technologies and materials was compiled by the NREL (National Renewable Energy Laboratory)[2] and is shown in Fig. 1.4.

A schematic thin-film CIGS solar cell is shown in Fig. 1.5. The CIGS absorber layer is deposited onto molybdenum coated soda-lime glass, forming the back contact. The $CuIn_{1-x}Ga_xSe_2$ layer is p-type and has typically a thickness of 1.5 to 3 μm. The n-type CdS buffer layer is usually obtained by chemical bath deposition and has a thickness of about 50 nm. This layer is then followed by a ZnO

[1] http://www.nrel.gov/pv/silicon_materials_devices.html
[2] http://www.nrel.gov/ncpv/

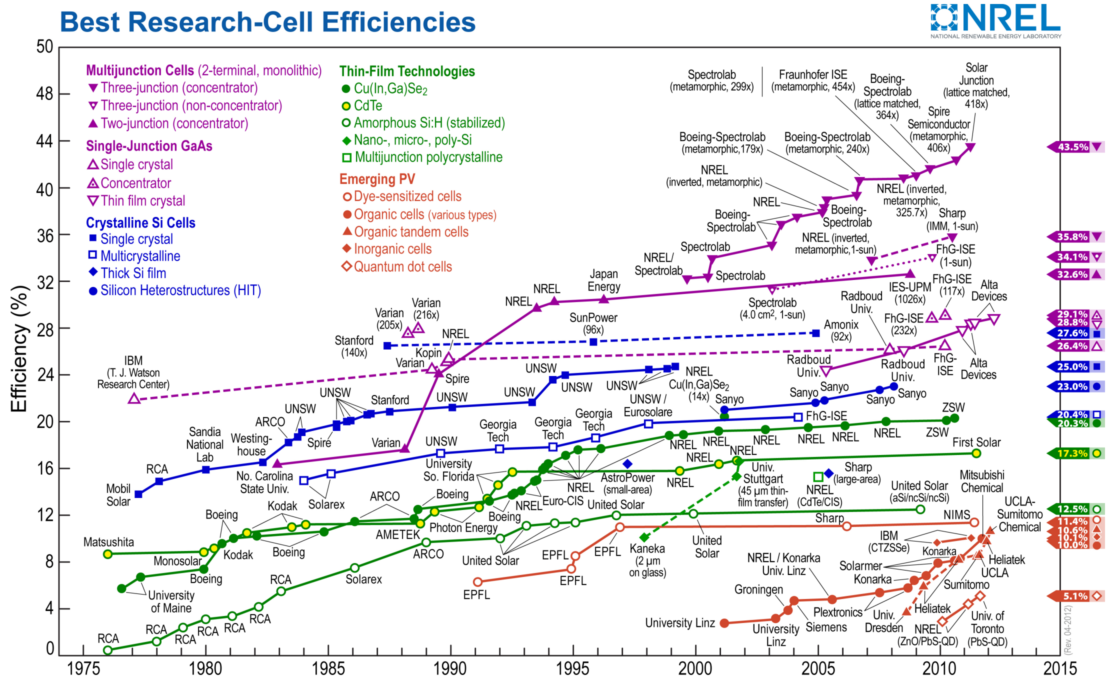

Figure 1.4: Best research-cell efficiencies compiled by the NREL.

window layer of a typical thickness of 0.5 to 2 μm which forms the front contact and is highly conducting and transparent [11]. The device is completed by the evaporation of an Al-grid. State of the art CIGS absorber layers (usually graded with high Ga content at the front) have an average band gap energy of ∼1.2 eV which corresponds to x=*0.3-0.4* [11, 12]. 20% efficiency cells can be produced with varying composition (Ga/(Ga+In) from 0.30 to 0.35 and Cu/(Ga+In) ratio from 0.80 to 0.92 [4].

The structure for CIGS on metal foils or polyimide is similar to those on Mo/glass. However, sodium, normally diffusing from the soda-lime glass, has to be put back into the structure to give the desired doping properties for the CIGS absorber layer [13]. The record efficiency achieved to date for CIGS-based solar cells on flexible metal foils is ∼15.2% [14] whereas on polyimide substrates it is ∼18.7% [12] as measured at simulated AM 1.5 standard test conditions. There are several advantages of depositing CIGS on flexible substrates such as a small weight and volume. In addition, the roll-to-roll deposition approach has the potential of lower manufacturing costs.

The efficiencies of $CuInSe_2$-, $CuInS_2$-, $CuGaSe_2$- and CIGS-based solar cells are still below the 30% predicted theoretically for a single junction solar cell [15]. Further improvements of the efficiencies will be facilitated by a deeper understanding

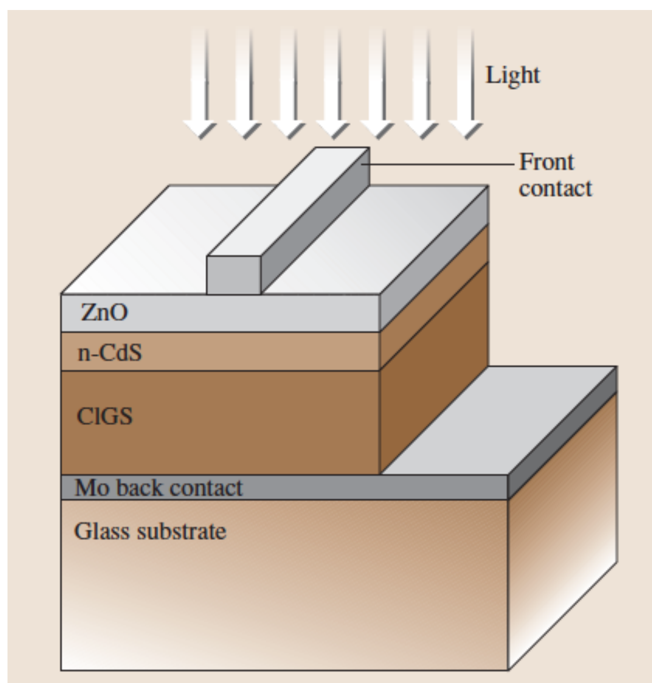

Figure 1.5: Schematic of a thin-film CIGS solar cells, taken from [5].

of the fundamental electronic material properties, in particular the nature of defects. The optical properties of $CuInSe_2$, $CuInS_2$, $CuGaSe_2$ are controlled by intrinsic defects. Small deviations from the ideal stochiometry result in a wide variety of such defects, [16] leading to challenges in their identification [17–19].
Optical spectroscopy is one of the most powerful tools to study defects in semiconductors. However, the reported photoluminescence spectra of $CuInSe_2$, $CuInS_2$, $CuGaSe_2$ mostly exhibit band-impurity (BI), donor-acceptor pair (DAP) and band-tail related recombination. [18, 20–24] This suggests that these studies involve material containing high concentrations of defects. If charged, such defects produce potential fluctuations causing broadening of the PL lines. The large spectral widths that result make it difficult to accurately determine the energy levels of the defect within the band gap. In the case of DAP transitions the involvement of two different defects further complicates their identification. In addition, screening effects caused by high concentrations of charge carriers add to the scatter of measured defect energy levels in the band gap. [17]
Study of the optical properties of excitonic states can provide reliable information on the electronic properties [25] and the nature of defects [26]. So far there are only a few reports on $CuInSe_2$, $CuInS_2$, $CuGaSe_2$ with clearly resolved excitonic features [26–33]. Temperature and excitation power dependent PL measurements of such excitonic features would provide important information about

the free excitons and on the nature of defects associated with the bound excitons. [26,31,32,34,35]
In addition, the effective mass of charge carriers is a fundamental concept in solid state physics. Its values and anisotropy have a profound influence on technologically important parameters such as conductivity, charge carrier mobilities, their densities of states and subsequently on the performance of electronic devices. The carrier effective masses and their anisotropy can be experimentally determined from magneto-PL measurements.

This work presents the studies of p-type $CuInSe_2$, $CuInS_2$ and $CuGaSe_2$ single crystals with ideal stoichiometry by means of photoluminesence spectroscopy. The photoluminescence of the three chalcopyrite semiconductors was studied as a function of excitation power, temperature and applied magnetic field.
The thesis consists of seven chapters. The present chapter has given a brief introduction to chalcopyrite semiconductors, their application as absorber layers in thin-film solar cells and the aim of this work. Chapter 2 presents the background of the three studied chalcopyrite semiconductors, in particular the crystal structure, the electronic structure as well as an introduction to excitons and their properties. Chapter 3 reveals the experimental techniques used to obtain the PL spectra under different conditions.
The experimental results are presented in chapters 4, 5 and 6. In Chapter 4 the excitation power and temperature dependence of the two free excitons as well as of a number of bound excitons is presented. Magneto-PL of the free excitons revealed an anisotropy of their reduced masses when the magnetic field is applied along different directions of the crystalline lattice. The excitation power and temperature dependence of the free and bound excitons in $CuInS_2$ is presented in Chapter 5. The $CuInS_2$ spectrum revealed lines due to exciton-polaritons and their properties were studied as a function of excitation power, temperature and applied magnetic field. From the magneto-PL of the exciton-polariton in $CuInS_2$ values for the effective hole mass are estimated. The results of the PL measurements as a function of excitation power, temperature and magnetic field in $CuGaSe_2$ are presented in Chapter 6.
Finally, the main results of the thesis are summarised and compared in Chapter 7. The thesis is concluded with suggestions for future work in Chapter 7.

Chapter 2

Background

This chapter provides information on the crystal structure and electronic properties of chalcopyrites. Furthermore, details on the defects in chalcopyrite semiconductors are given. The concept of excitons and their luminescence properties as well as their behaviour in magnetic fields are covered. The chapter concludes with information about polaritons which are a mixed-mode excitation.

2.1 Crystal and Electronic Structure

2.1.1 Crystal Structure

$CuInSe_2$, $CuInS_2$ and $CuGaSe_2$ are I-III-VI_2 (ABC_2) compounds and exhibit a chalcopyrite crystal lattice. Each A- and B-atom is tetrahedrally coordinated to four C-atoms while each C-atom is tetrahedrally coordinated to two A- and B-atoms. The chalcopyrite crystal lattice is shown in Fig. 2.1. If the cations A and B were randomly distributed a cubic zincblende structure would result. The chalcopyrite structure can be considered as a superlattice of the zincblende with the ratio of c/a being approximately 2, where c is the lattice constant along the z- and a is the lattice constant along the x- and y-direction, as shown in Fig. 2.1. One sub-lattice is occupied by cations and the other by anions. In comparison to the zincblende structure, the cations are replaced by one cation of higher valency and one of lower valency, which occupy the cation sub-lattice in an ordered manner, in the chalcopyrites.

The tetrahedral coordination indicates that the bonding is primarily covalent with sp^3 hybrid bonds and also an ionic character is present due to the different atoms [36]. The I-III-VI_2 compound has a binary II-VI analogue such as ZnSe. The

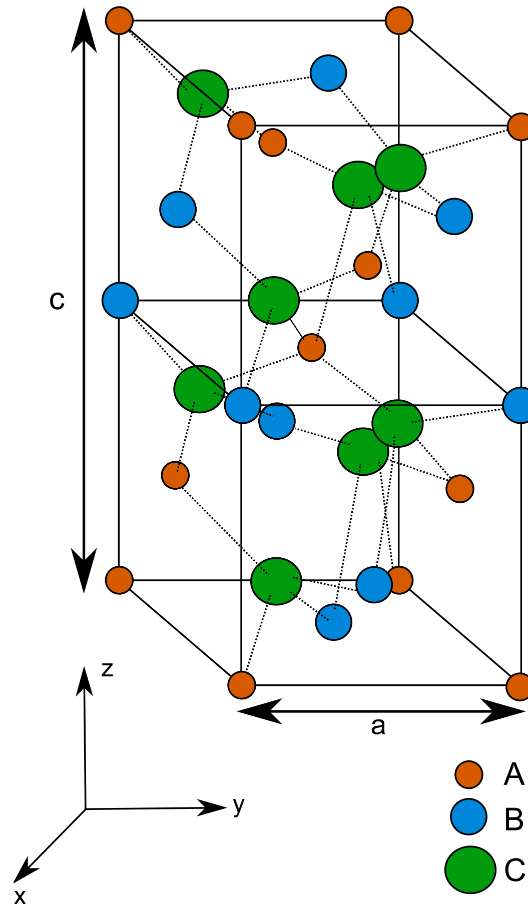

Figure 2.1: Crystal lattice of the chalcopyrite compounds $CuInSe_2$, $CuInS_2$ and $CuGaSe_2$.

ternary chalcopyrites have some structural anomalies compared to their binary analogues [37]

1. Rather than having a single cation, the ternary chalcopyrites have two cations. The atom arrangement starting from the A-atom and translating in the vertical direction in Fig. 2.1 through intervals of $c/2$ follows a ABAB sequence. In the horizontal direction, the order of the atoms follows an AAA sequence in intervals of a.

2. Chaclopyrite crystals often show a tetragonal distortion where the ratio of $\eta \equiv c/2a$ can differ from unity by up to 12 %.

3. In the chalcopyrite lattice the anions are displaced from their zincblende sites. In the binary AC zincblende compound each cation A has four anions C as nearest neighbors, whereas in a ternary chalcopyrite ABC_2 each cation A and B has 4 anions C as nearest neighbors, and each anion has two A and

Compound	a ($\AA$)	c ($\AA$)	c/a	u	Refs.
$CuGaSe_2$	5.607	10.99	1.960	0.25	[38]
	5.614	11.03	1.965	0.250	[39]
	5.5963	11.0036	1.96623	0.2431	[40]
$CuInS_2$	5.517	11.06	2.005	0.20	[38]
	5.523	11.12	2.013	0.214	[39]
	5.522	11.132	2.015	0.2295	[41]
$CuInSe_2$	5.773	11.55	2.001	0.22	[38]
	5.784	11.616	2.008	0.224	[39]
	5.782	11.620	2.009	0.235	[42]

Table 2.1: Compilation of experimental structural parameters a and c (lattice constants), u (anion displacement) and $2\eta \equiv c/a$ (tetragonal deformation) measured at room temperature for $CuInSe_2$, $CuInS_2$ and $CuGaSe_2$ and taken from Jaffe et al. [37].

two B cations as nearest neighbor. As a results, the anion C usually adopts an equilibrium position closer to one pair of cations than to the other. This leads to an unequal bond length:

$$R_{AC} \neq R_{BC} \tag{2.1}$$

and the nearest neighbour anion-cation bond lengths are given by [37]:

$$R_{AC} = \left[u^2 + \left(1 + \eta^2\right)/16\right]^{1/2} a \tag{2.2}$$

$$R_{BC} = \left[\left(u - \frac{1}{2}\right)^2 + \left(1 + \eta^2\right)/16\right]^{1/2} a \tag{2.3}$$

where u is the anion displacement $u - \frac{1}{4} = \left(R_{AC}^2 - R_{BC}^2\right)/a^2$ and $2\eta{=}c/a$ is the tetragonal deformation, sometimes re-expressed as the tetragonal distortion *2-(c/a)*.

Further details on the crystal structure can be found in Refs. [36, 37].

2.1.2 Electronic Structure

The uppermost valence bands of $CuInSe_2$, $CuInS_2$ and $CuGaSe_2$ are essentially p-like and are built up from the cation (Se or S) 4p states with admixture of Cu 3d states. In addition to the influence of the d-levels, the structural differences of the chalcopyrite lattice relative to the zincblende lattice contribute to a non-cubic crystal potential. According to the quasicubic model of Hopfield [43], the

triple degeneracy of the valence band at the Γ-point of the Brillouin zone in the zincblende compounds is lifted due to the simultaneous influence of the non-cubic crystal field and spin-orbit interactions. The crystal-field splitting Δ_{cf} and spin-orbit splitting Δ_{so} are determined from the observed valence band splitting and the energies are given by [43, 44]:

$$E_{1,2} = \frac{1}{2}(\Delta_{so} + \Delta_{cf}) \pm \frac{1}{2}[(\Delta_{so} + \Delta_{cf})^2 - \frac{8}{3}\Delta_{so}\Delta_{cf}] \tag{2.4}$$

Δ_{cf} and Δ_{so} can be estimated from the excitonic transitions related to the three valence bands to the conduction band and are summarised in Table 2.2. The sign and magnitude of the crystal field splitting Δ_{cf} is dominated by the built-in lattice compression:

$$\Delta_{cf} = \frac{3}{2}b(2 - \frac{c}{a}) \tag{2.5}$$

where b is the deformation potential which was estimated as $b \approx -1.0$ by Shay et al. [45] for Cu and Ag related chalcopyrite semiconductors. The diagrams of the $CuInSe_2$, $CuInS_2$ and $CuGaSe_2$ band structures are shown in Figs. 2.2, 2.3 and 2.4 respectively.

Compound	$\mathbf{\Delta_{cf}}$ **theo.** (meV)	$\mathbf{\Delta_{so}}$ **theo.** (meV)	**Ref.**	$\mathbf{\Delta_{cf}}$ **exp.** (meV)	$\mathbf{\Delta_{so}}$ **exp.** (meV)	**Ref.**
$CuInS_2$	5	-29	[46]	≤ 5	-19	[47]
$CuInSe_2$	7	193	[46]	6	233	[48]
$CuGaSe_2$	-104	210	[46]	-112	231	[49]

Table 2.2: Crystal-field Δ_{cf} and spin-orbit splittings Δ_{so} of the chalcopyrite compounds $CuInSe_2$, $CuInS_2$ and $CuGaSe_2$. The theoretical values have been calculated by Persson (Ref. [46]) using a full-potential linearised augmented plane wave method and are room temperature values. The experimental values have been taken from Refs. [47–49] and were determined from reflectivity measurements at 77 K.

2.1.2.1 $CuInSe_2$

In $CuInSe_2$ the triple degeneracy of the p-like valence bands is completely lifted due to the simultaneous effects of the non-cubic crystal field and spin-orbit interaction. This results in a splitting of the valence band into three sub-bands A, B and C. As seen from Eq. 2.5, in $CuInSe_2$ a small negative value in the tetragonal

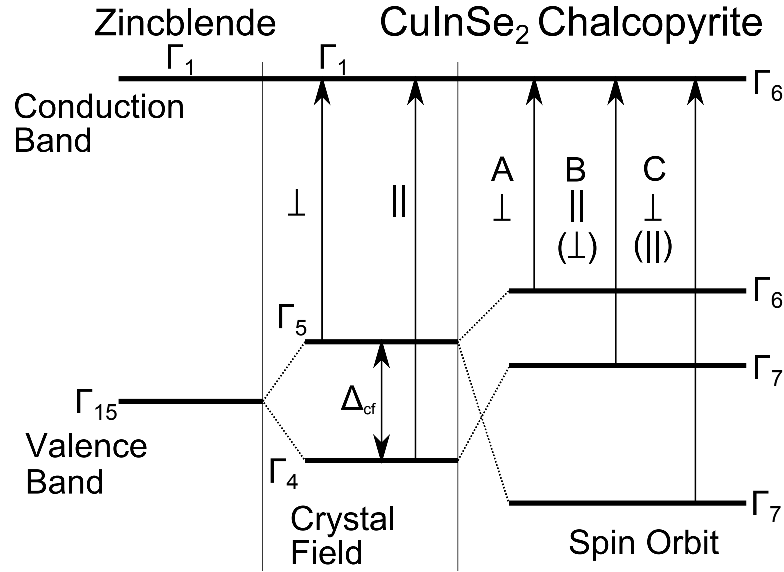

Figure 2.2: Band structure and selection rules for the transitions in $CuInSe_2$.

distortion *(2-c/a)* results in a small positive crystal field splitting.
Evolving from zincblende structure of for example ZnSe to $CuInSe_2$ as shown in Fig. 2.2, the Γ_{15} valence band splits into a doubly degenerated level Γ_5 lying above a nondegenerated Γ_4 due to the crystal field. Transitions from the Γ_4 valence band to the Γ_1 conduction band are only allowed for $E \| z$, and Γ_5 to Γ_1 transitions are only allowed fro $E \perp z$. The Γ_5 valence band further splits into Γ_6 and Γ_7 due to the spin-orbit interaction. The polarisation rules are then slightly relaxed as it can be seen in Fig. 2.2.
Shay et al. [48] observed the A, B and C transition in $CuInSe_2$ at 1.038, 1.042 and 1.273 eV, respectively, using reflectivity measurements at 77 K. The corresponding crystal-field and spin-orbit splitting were determined as Δ_{cf}=6 meV and Δ_{so}=233 meV, respectively. In addition, Mudryi et al. [30] measured the crystal-field and spin-orbit splitting as Δ_{cf}=5.3±0.3 meV and Δ_{so}=234.7±0.3 meV, respectively, at 4.2 K which is in good agreement with the values determined by Ref. [48].

2.1.2.2 $CuInS_2$

For $CuInS_2$ the value of the tetragonal distortion *(2-c/a)* is small and negative. The crystal field splitting in $CuInS_2$ is close to zero and thus degeneracy of the valence band is not completely lifted as seen in Fig. 2.3. In $CuInS_2$, the valence band splits into two sub-bands, a nondegenerated Γ_7 which corresponds to the A transition and a double degenerated Γ_6 Γ_7 which corresponds to the BC transition. Fig. 2.3 illustrates the $CuInS_2$ band structure and the selection rules. Due to the

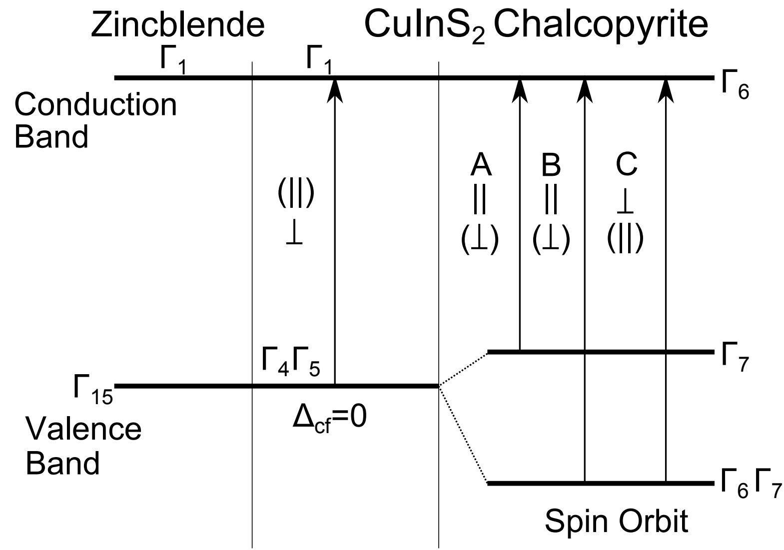

Figure 2.3: Band structure and selection rules for the transitions in $CuInS_2$.

Γ_7 symmetry of the upper valence band and the double degeneracy of the lower valence band, transitions to the conduction band are allowed for both E$\|$z and E$\perp$z. Shay et al. [47] determined a crystal-field splitting of $\mathbf{\Delta_{cf}} \leq 5$ meV and a spin-orbit splitting of $\mathbf{\Delta_{so}}$=-19 meV at 77 K using reflectivity measurements. Reflectivity measurements at 4.2 K by Yakushev et al. [33] measured a value of $\mathbf{\Delta_{so}}$=-18 meV for the spin-orbit splitting which is close to the result obtained by [47] but no crystal field splitting was observed.

2.1.2.3 $CuGaSe_2$

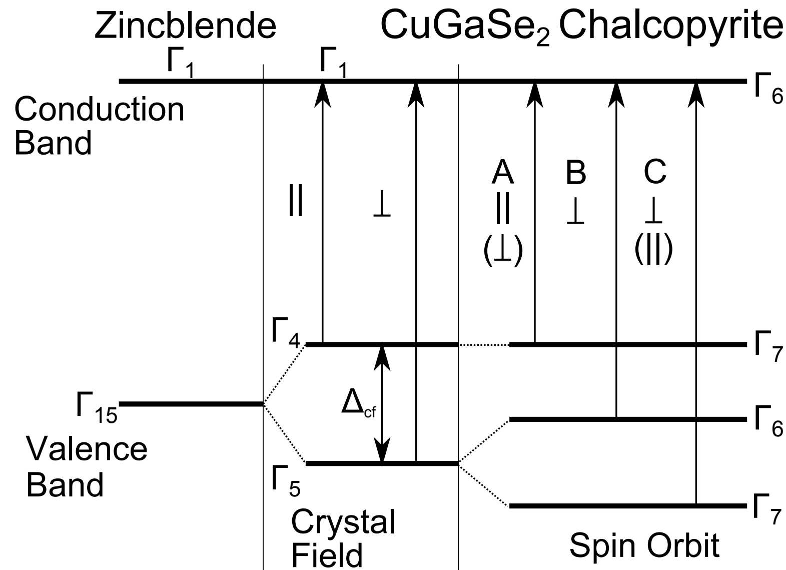

Figure 2.4: Band structure and selection rules for the transitions in $CuGaSe_2$.

The value of the tetragonal distortion *(2-c/a)* is positive and results in a negative crystal field splitting. Due to the crystal-field the valence band splits into a nondegenerated Γ_4 lying above a doubly degenerated Γ_5. The Γ_5 valence band further splits into Γ_6 and Γ_7 due to the spin-orbit interaction. The selection rules are then slightly relaxed as can be seen in Fig. 2.4. The ordering of the valence bands is inverse compared to that of $CuInSe_2$ with the Γ_7 sub-band being at the top as shown in Fig. 2.4.
Tell et al. [49] determined the energies of the A, B and C transitions as 1.729, 1.813 and 2.016 eV, respectively, at 77 K using reflectivity measurements. The crystal-field splitting was determined as Δ_{cf}=-112 meV and the spin-orbit splitting as Δ_{so}=231 meV.
In addition, it was observed by Shay et al. [47] that the energy gaps of the ternary compounds are less than the energy gaps of the respective binary analogues. It was also reported that the spin-orbit splitting Δ_{so} are considerably smaller than the values observed in the binary analogues. Ref. [47] suggested that these anomalies result from a hybridization of the p-like valence band with the metal d-levels. Fig. 2.5 displays the valence band with Copper d-levels present. The

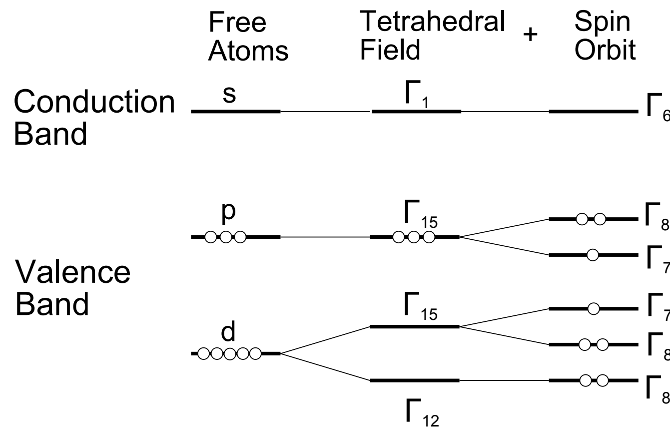

Figure 2.5: Sketch of the effect of d-levels in a tetrahedral field, after [36].

fivefold degenerated d-levels split into a threefold Γ_{15} and a twofold Γ_{12} in a tetrahedral field. The p-levels transform as Γ_{15}. Including spin-orbit interaction the Γ_{15} p-levels split into a doublet Γ_8 above a singlet Γ_7, whereas the d-like Γ_8 splits into a doublet below a singlet Γ_7. The interaction between the Γ_{15} levels in Fig. 2.5 will have two effects. The uppermost Γ_{15} will be raised to higher energy which results in a reduction of the band gap. In addition, the spin-orbit splitting of the uppermost valence bands will be reduced since the negative Δ_{so} of the d-levels partially cancels the positive Δ_{so} of the p-levels [36]. The uppermost

doublet Γ_8 and the singlet Γ_7 levels will further separate into Γ_7, Γ_6 and Γ_7 due to the crystal-field [50].

Jaffe et al. [51] reported that in addition to the p-d-hybridization other factors can have a smaller influence on the band gap anomaly in particular structural effects such as the non-ideal anion displacement (see Section 2.1.1).

2.2 Defects

In general defects can be classified into point and line defects. Point defects correspond to an isolated atom in a localised region of a host crystal. Line defects involve rows of atoms such as for example dislocations. In addition, defects composed of a small number of point defects are referred to as complexes. Point defects can be classified into the following kinds [52]

- Vacancy: Created by a missing atom A and labeled as V_A.
- Interstitial: An atom occupying an interstitial site and labeled as I_A.
- Substitutional: An atom C replacing a host atom A and labeled as C_A.
- Antisite: A special kind of substitutional defect in which a host atom B occupies the site of another host atom A and labelled as B_A.

Vacancies and antisites defects are intrinsic or native defects since they do not involve foreign atoms. Defects involving foreign atoms are called extrinsic defects. Defects can contribute electrons or holes to the host crystal and are then called donors or acceptor, respectively. When a substitutional impurity atom/defect has the same valence as the host atom it is referred to as an isoelectronic or isovalent center.

Shallow donors or acceptors can be described as hydrogenic centers. The Coulomb attraction between the donor electron and the positive charge in this hydrogen-like impurity is much weaker than the Coulomb attraction in the hydrogen atom since it is strongly screened by the large number of valence electrons of the host crystal. In order to calculate the ionisation energy of the donor electron, the free electron mass in the Rydberg energy m_e is subsituted by the effective mass m^* of the host crystal electrons and the dielectric constant ϵ_0 by $\epsilon_0\epsilon_{host}$:

$$E_i = \frac{m^* e^4}{2(4\pi\epsilon_0\epsilon_{host}\hbar)^2}\frac{1}{n^2} \tag{2.6}$$

The resulting energy level of the donor is located below the conduction band and the energy E_i is required to lift the electron into the conduction band, ionising the donor. Eq. 2.6 is equally valid for acceptors in which case the acceptor level is located just above the valence band.
In ternary compounds such as $CuInSe_2$, $CuInS_2$ and $CuGaSe_2$, 12 native defects are possible: 3 vacancies, 3 interstitials and 6 antisite defects. In addition, more complex defects combining these could occur. The defect physics of ternary chalcopyrite compounds shows unusual effects with respect to the binary II-VI analogues [16]:

- Structural tolerance to large off-stoichiometry towards Indium and Gallium excess:
  Unlike the II-VI analogues (ZnSe, CdS) $CuInSe_2$, $CuInS_2$ and $CuGaSe_2$ can tolerate a large range of anion-to-cation stoichiometry. The extreme limit of the "off-stoichiometry" manifests itself as a series of compounds with different anion-cation ratios such as $CuIn_5Se_8$ and $CuIn_3Se_5$.

- Ability to be doped via native defects:
  $CuInSe_2$ can be prepared with p-type conductivity under Se-excess and Cu-deficient growth conditions whereas n-type conductivity can be achieved under Cu-excess and Se-deficient conditions [11]. $CuInS_2$ can also be pepared n- and p-type [26]. Sulphur-rich samples are p-type whereas metal-rich sample are n-type. In contrast, $CuGaSe_2$ remains p-type under all stoichiometry deviations [19]. These defects are mainly shallow and their formation does not result in deep compensating defects.

- The electrically benign nature of the structural defects:
  In silicon and III-V semiconductors, polycrystallinity leads to a high concentration of electrically active defects which can have a detrimental effect on the performance of optoelectronic devices. In contrast, polycrystalline $CuInSe_2$ is as good an electronic material as its single crystal counterpart.

2.3 Excitons

The attractive Coulomb interaction between an electron in the conduction band and a hole in the valence band leads to the formation of an exciton [52–55]. There are Frenkel and Wannier-Mott excitons depending on the material properties. Frenkel excitons are tightly bound and within the same or nearest-neighbor

unit cell. They can be found in relatively ionic materials such as alkali halides. Materials showing Frenkel excitons exhibit a relatively low mobility and a small dielectric constant. The binding energy of Frenkel excitons is in the order of ~ 1 eV [53].

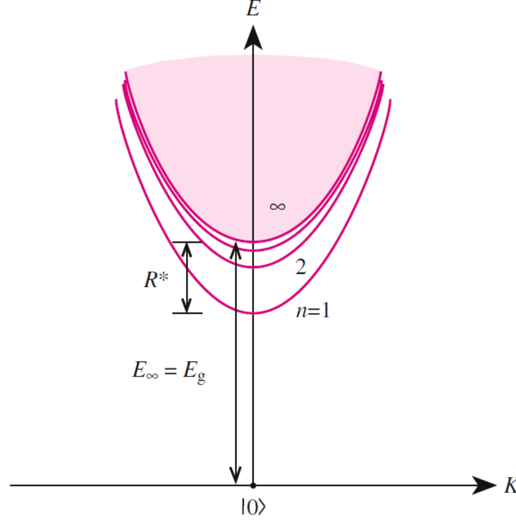

Figure 2.6: Exciton dispersion curve, taken from [52].

In contrast, Wannier-Mott excitons can be found in materials with a significant degree of covalent binding, a high mobility and a relatively large dielectric constant. The binding energy of a Wannier-Mott is only a few per cent of the value of the Frenkel exciton. For the Wannier-Mott exciton the wavefunction, describing the interaction electron and hole separation extends over a many unit cells of the crystal. The exciton forms a hydrogen like state within the band gap with the free electron mass m_0 is substituted by the reduced mass of the effective masses of the electrons m_e and holes m_h. Also, the dielectric constant of the vacuum is replaced by the dielectric constant of the semiconductor which takes the screening by the large number of valence electrons of the semiconductor into account. The exciton dispersion relation is shown in Fig. 2.6 and given by [52]:

$$E_X(n, \mathbf{K}) = E_g - Ry^* \frac{1}{n^2} + \frac{\hbar^2 \mathbf{K}^2}{2M} \tag{2.7}$$

where $M = m_e + m_h$ is the translational mass and $\mathbf{K} = \mathbf{k_e} + \mathbf{k_h}$ the wave vector of the exciton. The second term of Eq. 2.7 is the excitonic Rydberg energy given by:

$$Ry^* = 13.6eV \cdot \frac{\mu}{m_0} \frac{1}{\epsilon^2} \tag{2.8}$$

where ϵ is the dielectric constant of the semiconductor and μ is the reduced mass:

$$\mu = \frac{m_e m_h}{m_e + m_h} \tag{2.9}$$

The separation between the electron and hole is given by the exciton Bohr radius:

$$a_B = a_B^H \epsilon \frac{m_0}{\mu} \tag{2.10}$$

where a_B^H is the Bohr radius of the hydrogen atom.

2.3.1 Free Excitons

One of the principal features of free excitons is their ability to move through the crystal. Their energy consists of two parts, the Coulomb interaction between the electron and the hole and the translational kinetic energy of the system.
The conservation of momentum requires that only excitons with a momentum equal to that of photons can radiate. Since the photon momentum is nearly zero, only transitions involving nearly zero momentum excitons are allowed.
Free excitons can propagate through the crystal and it is possible to produce them in one part of the crystal and to detect them in another region. At liquid Helium temperatures ($\sim$1.4 to 4.2 K) the free exciton PL line has a temperature independent FWHM which depends only on interactions between excitons and impurities, resulting in a FWHM larger than kT [56]. With increasing temperature the FWHM generally increases due to the exciton-phonon interactions, which will be discussed in Section 2.4.1.

2.3.2 Bound Exciton

An exciton can also form a bound state with a defect. The binding energy is increased by the presence of a point defect, which can be a neutral or ionised impurity. If the total energy of the system is reduced, corresponding to an increase in binding energy, when the exciton is in the vicinity of the impurity then it is energetically favorable for the exciton to remain near the defect and the exciton becomes bound to the defect [57]. Haynes [58] found that the binding energy E_D of an exciton bound to a donor in silicon is increased by an amount proportional

to the donor ionisation energy E_i, which is known as Haynes'rule:

$$E_D = 0.1E_i \tag{2.11}$$

Hopfield [59] suggested that the increase in donor binding energy depends on the ratio $\sigma = \frac{m_e}{m_h}$ which is different for different impurities in a given material. Sharma [60] presented the first theoretical work which gives the binding energy of the bound exciton for various values of σ. The theoretically estimated value of the binding energy of an exciton bound to a donor/acceptor in silicon by Ref. [60] was found to be consistent with the experimental observation by Ref. [61]. The ratio of the effective masses was then calculated for charged [62] and neutral defects [62, 63].

The emission of bound excitons is characterised by a narrow spectral width at a lower photon energy than that of the FE [64]. This narrow FWHM, below kT, indicates that the excitons are localised to a defect and immobile [58]. Bound excitons do not experience broadening due to the kinetic energy anticipated for free excitons in a semiconductor with good mobility [53]. The momentum conservation rule is relaxed for localised excitons since the exciton wavevectors are reduced by the localisation. The value of the radiative decay time of a bound exciton is decreased with respect to the value of the radiative decay of free excitons, which results in a stronger luminescence than that of the free excitons [65] at low temperatures.

2.4 Photoluminescence

Photoluminescence spectroscopy is a very sensitive method to study optical transitions in semiconductors [52, 57, 66]. Photoluminescence is the radiation emitted by a physical system resulting from excitation to a nonequilibrium state by irradiation with light. Three processes are involved in the creation of PL:

- Excitation: Creation of electron-hole pairs by absorption of the exciting light.
- Thermalisation: Excited electron-hole pairs relax towards quasi-thermal equilibrium distribution.
- Recombination: The thermalised electron-hole pairs recombine radiatively to produce the emission which is then followed by the escape of the radiation

from the sample.

The exciting light is absorbed, creating electron-hole pairs with the greatest excitation of the sample being close to the surface. In attempting to regain equilibrium, the excess carriers will thermalise and accumulate at the conduction and valence band extrema where they may recombine.
By recombining, the electron-hole pairs produce spontaneous emission. Its rate can be described by the Einstein coefficient A. The conduction and valence band have a population N and the radiative emission rate is given by [66]:

$$\left(\frac{dN}{dt}\right)_{rad} = -AN \tag{2.12}$$

The number of photons emitted in a given time is proportional to the Einstein coefficient of the transition and also to its population. The rate equation can be solved, resulting in:

$$N(t) = N(0)e^{-At} = N(0)e^{-t/\tau_R} \tag{2.13}$$

where $\tau_R^{-1} = A$ is the radiative lifetime of the transition. The electron-hole pairs relax very rapidly to the lowest state of the conduction and valence band, respectively. The radiative recombination is not the only mechanism by which electron-hole pairs can recombine. Non-radiative recombination can occur when the charge carriers lose their energy as heat by emitting phonons or transfer their energy to impurities or defects. Taking the non-radiative radiation into account Eq. 2.12 can be rewritten to:

$$\left(\frac{dN}{dt}\right)_{total} = -\frac{N}{\tau_R} - \frac{N}{\tau_{NR}} = -N\left(\tau_R^{-1} + \tau_{NR}^{-1}\right) \tag{2.14}$$

The luminescent efficiency η_R is the ratio of the radiative emission (Eq. 2.12) and the total de-excitation, i.e. the rate at which the excited state decays, (Eq. 2.14) and is given by:

$$\eta_R = \frac{AN}{N\left(\frac{1}{\tau_R} + \frac{1}{\tau_{NR}}\right)} = \frac{1}{1 + \frac{\tau_R}{\tau_{NR}}} \tag{2.15}$$

2.4.1 Excitonic Line Shapes

The shape of excitonic lines have been calculated by Toyozawa [67]. He assumes that the linewidth is essentially determined by the lifetime of excitons at $\mathbf{K}$=0

before they are scattered by phonons to other momentum states. An eigenstate can only be perfectly sharp if its lifetime is infinite. However, if its lifetime is finite, according to the uncertainty principle ($\Delta E \Delta \tau > \hbar$), some uncertainty in its energy is necessary. Therefore the width of the excitonic line is determined by all processes, including phonon scattering, which limit the time that the exciton spends in the **K**=0 state. Toyozawa [67] discusses the cases of weak and strong phonon coupling. Weak phonon coupling results in a Lorentzian line shape whereas strong coupling leads to a Gaussian line shape. In addition to phonon coupling, other effects such as crystal imperfections, impurities and strain can cause inhomogeneous broadening of the exciton line and cause a Gaussian line shape. The FWHM becomes [57]:

$$\Gamma = \Gamma_0 + \Gamma_{ph} \tag{2.16}$$

where Γ_0 is the width due to inhomogeneous broadening and Γ_{ph} is the width due to phonon scattering.

The temperature dependence of Γ can be interpreted as a broadening due to exciton-phonon scattering [68–70] and can be described by:

$$\Gamma(T) = \Gamma_0 + \Gamma_a T + \frac{\Gamma_{LO}}{\left[exp\left(\frac{\hbar\omega_{LO}}{kT}\right) - 1\right]} \tag{2.17}$$

where Γ_a is the exciton-acoustic-phonon coupling strength, Γ_{LO} is a parameter describing the exciton-LO-phonon interactions and $\hbar\omega_{LO}$ is the LO (longitudinal optical) phonon energy.

At low temperatures $\Gamma(T)$ is usually determined by the scattering of excitons by acoustic phonons, accounted by the second term in Eq. 2.17. At higher temperatures the density of LO phonons increases and exciton-LO-phonon interaction dominates [70]. The exciton-LO-phonon interaction is determined by the third term in Eq. 2.17.

2.4.2 Temperature Induced Quenching of Excitonic Lines

The study of the temperature dependence of excitonic luminescence can provide information on the activation energy of the underlying process. With increasing temperature the spectral position of the excitonic luminescence follows the temperature dependence of the band gap. The intensity of the excitonic emission decreases as the thermal energy becomes greater than the exciton binding energy.

The temperature quenching of excitonic lines is due to the thermally activated depopulation of the excitonic level and/or to the activation of nonradiative recombination centres. Under injection, the population of a certain level is given by [71]

$$\frac{\delta n}{\delta t} = G - \frac{n}{\tau_R} - \frac{n}{\tau_{NR}} \tag{2.18}$$

where n is the density of the exciton concerned, G is the generation rate, τ_R and τ_{NR} are the radiative and non-radiative lifetimes. Non-radiative recombination rates are generally thermally activated:

$$\tau_{NR} = \tau_0 \cdot exp(E_{a1}/kT) \tag{2.19}$$

where τ_0 is the excess carrier lifetime, E_{a1} the activation energy and k is the Boltzmann constant. Under steady state, the left side of Eq. 2.18 becomes equal to zero. In addition PL intensities are proportional to n/τ_R which yields:

$$I = \frac{I_0}{[1 + a \cdot exp(-E_{a1}/kT)]} \tag{2.20}$$

where a=τ_R/τ_0. Eq. 2.20 works for some cases of thermal PL line quenching, for example for that of the low energy bound exciton lines in $CuInSe_2$ and $CuInS_2$ (see Chapter 4 and 5, respectively). The thermal quenching behaviour of the higher energy bound exciton lines in $CuInSe_2$, $CuInS_2$ and $CuGaSe_2$ requires the inclusion of a second competitive non-recombination channel which becomes effective at temperatures where the quenching of the free exciton PL lines is also effective. In this case Eq. 2.20 can be extended to [71, 72]:

$$I = \frac{I_0}{[1 + a_1 \cdot exp(-E_{a1}/kT) + a_2 \cdot exp(-E_{a2}/kT)]} \tag{2.21}$$

In the case of a thermal redistribution of charge carriers from bound exciton levels towards the free excitons as observed for $CuInS_2$ (Chapter 5) Eq. 2.20 needs to be modified as discussed in the following paragraph.

The calculations are based on those from Dr. M. Leroux (CRHEA-CNRS, Valbonne) for the polarised luminescence of free excitons in InGaN/GaN [73]. Assuming that an exciton 1 thermally redistributes to a higher energy exciton level 2, then the temperature dependence of the exciton line 2 consists of two contributions:

1. At sufficient temperatures, charge carriers from level 1 are lifted to the

higher energy level 2, which can result in an increase of intensity with respect to level 1 (I_2/I_1).

2. With further increasing temperature, exciton 2 will start to dissociate with its intensity decreasing according to Eq. 2.20.

The intensity of this system is then given by:

$$I(T)_{total} = \frac{I_2}{I_1} \cdot I(T)_2 \tag{2.22}$$

where the intensity ratio I_2/I_1 can be expressed by:

$$\frac{I_2}{I_1} = \left(\frac{n_2}{n_1}\right) \cdot \left(\frac{\tau_{R1}}{\tau_{R2}}\right) \tag{2.23}$$

A schematic of the system with the two levels 1 and 2 is shown in Fig. 2.7.

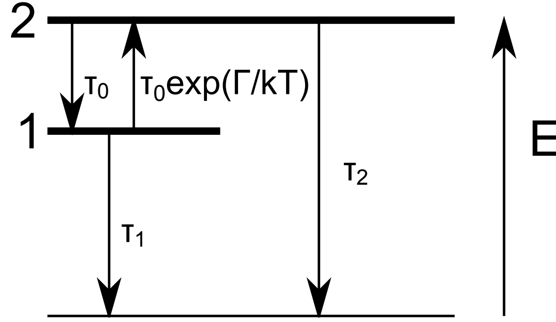

Figure 2.7: Schematic of the dissociation processes with two exciton energy levels 1 and 2.

In order to obtain the temperature dependent quenching of line 2, the following rate equations have to be solved:

$$\begin{aligned} \frac{dn_1}{dt} &= 0 = G_1 - \frac{n_1}{\tau_1} - \frac{n_1}{\tau_0 \cdot exp(\Gamma/kT)} + \frac{n_2}{\tau_0} \\ \frac{dn_2}{dt} &= 0 = G_2 - \frac{n_2}{\tau_2} - \frac{n_2}{\tau_0} + \frac{n_1}{\tau_0 \cdot exp(\Gamma/kT)} \end{aligned} \tag{2.24}$$

Γ is the energy separation between level 1 and 2. Rearrangement and combination of the equations in 2.24 yields:

$$n_2 = \tau_2(G_1 + G_2 - \frac{n_1}{\tau_1}) \tag{2.25}$$

and

$$n_1 \left[\frac{1}{\tau_1} + \frac{\tau_2}{\tau_0\tau_1} + \frac{1}{\tau_0 \cdot exp(\Gamma/kT)}\right] = G_1 + (G_1 + G_2)\frac{\tau_2}{\tau_0} \tag{2.26}$$

which can be rewritten to:

$$n_1 = \frac{G'AB}{[B + A \cdot exp(-\Gamma/kT)]} \tag{2.27}$$

with

$$\begin{aligned} G' &= G_1 = (G_1 + G_2)\frac{\tau_2}{\tau_0} \\ A &= \frac{\tau_0\tau_1}{\tau_0 + \tau_2} \\ B &= \tau_0 \end{aligned} \tag{2.28}$$

The formation of the ratio of the population of level 1 and 2 can be expressed by $\frac{\mathrm{n}_2}{\mathrm{n}_1}$:

$$\frac{n_2}{n_1} = \frac{G''\left[B + A \cdot exp(-\Gamma/kT)\right]}{G'AB - \left(\frac{\tau_2}{\tau_1}\right)} \tag{2.29}$$

with $G'' = \tau_2(G_1 + G_2)$ and inserting Eq. 2.29 into 2.23 gives:

$$\frac{I_2}{I_1} = \frac{G''\left[B + A \cdot exp(-\Gamma/kT)\right]}{G'AB - \left(\frac{\tau_2}{\tau_1}\right)}\left(\frac{\tau_{R1}}{\tau_{R2}}\right) \tag{2.30}$$

Eq. 2.30 is of the form of:

$$\frac{I_2}{I_1} = \left[\alpha + \beta \cdot exp(-\Gamma/kT)\right] \tag{2.31}$$

Inserting Eq. 2.31 into 2.22 yields:

$$I(T) = \frac{I_0\left[\alpha + \beta \cdot exp(-\Gamma/kT)\right]}{1 + \gamma \cdot exp(-E_{a1}/kT)} \tag{2.32}$$

where Γ is the energy separation between the two excitonic levels, E_{a1} is the activation energy and α, β and γ are the process parameters.
A thermal redistribution of excitons towards a higher energy level such as the UPB of the A exciton-polariton in $CuInS_2$ is observed in Chapter 5. Eq. 2.32 is used to describe the temperature dependence of the integrated intensity of the upper branch of the A exciton-polariton and values for Γ and E_{a1} are determined, as shown in Fig. 2.8. It was found that charge carriers from the bound exciton associated with PL line 2 thermally redistribute towards the UPB of the A exciton-polariton, causing an increase in intensity. A detailed explanation can

be found in Chapter 5.

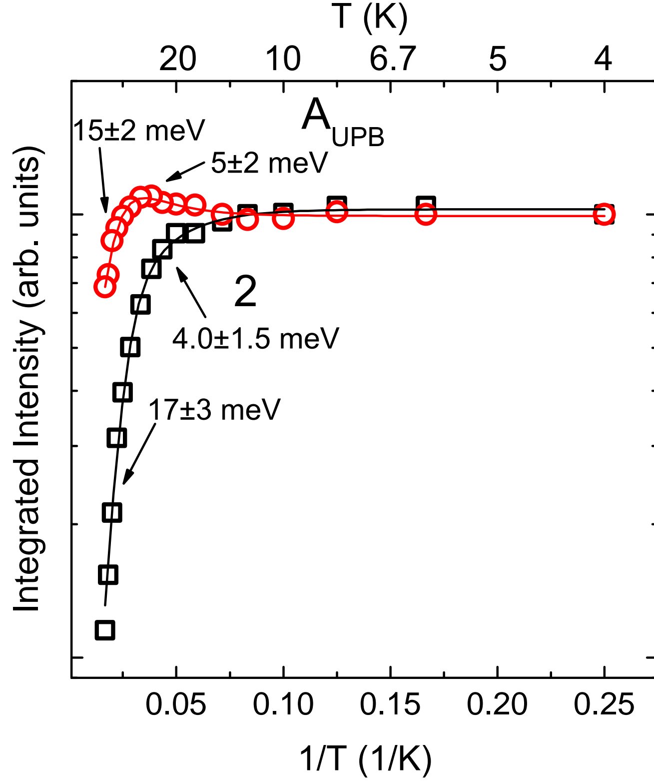

Figure 2.8: Arrhenius plot of the integrated PL intensity of the bound excitons 2 and A_{UPB} in $CuInS_2$ fitted using Eqs. 2.21 and 2.32, respectively.

2.4.3 Excitation Power Dependence of Excitonic Lines

The study of excitation power dependence of PL lines is important for the identification of the underlying recombination process [74]. The spectral position of excitonic emission does not depend on the excitation power P. In general the dependence of the integrated PL intensity I of the free and bound excitonic lines, on the laser excitation power P follows the power law $I \sim P^k$. A value of k between 1 and 2 is expected for free exciton transitions since their intensity is directly proportional to the total number of excitons, which in turn depends on the product of the number of holes and electrons, each of which is proportional to the excitation power P [74]. Since bound excitons are in thermal equilibrium with free excitons, the concentration of bound excitons is proportional to that of free excitons [32]. Therefore values of k between 1 and 2 are expected for bound exciton transitions, assuming the concentration of defects is high enough and no saturation occurs.

2.5 Excitons in Magnetic Fields

The application of high magnetic fields can provide information on the electronic properties of semiconductors. The strength of the magnetic field B can be characterised by the non-dimensional parameter γ given by [75]:

$$\gamma = \frac{\hbar e B}{2 R y^* \mu} \tag{2.33}$$

where $\hbar$ is the reduced Planck's constant, e is the electron charge, Ry^* is the excitonic Rydberg energy and $\mu = m_e m_h/(m_e + m_h)$ is the reduced mass of the exciton, m_e and m_h are the effective electron and hole mass, respectively. The low-field condition assumes $\gamma \ll 1$. In this region the Coloumb energy dominates and the magnetic field can be treated as a perturbation.

2.5.1 Diamagnetic shift of excitons

The interaction of an exciton in a magnetic field can be described in terms of a diamagnetic shift. The diamagnetic shift is caused by the deformation of the relative motion of the electron and hole in the exciton caused by Lorentz forces. For weak magnetic fields, the effects of such deformation can be treated as a perturbation. For the ground state, with an s-envelope wave-function and angular momentum of l = 0, this deformation can be described in terms of an admixture of the p-envelope functions with l = 1. As a result, the angular momentum of the exciton becomes proportional to the magnetic field strength B. The energy of a magnetic dipole in a magnetic field is also proportional to B, resulting in an overall quadratic dependence of the excitonic energy with respect to B for the low magnetic field region [54]

$$E(B) = E_0 + c_d B^2 \tag{2.34}$$

where E_0 is the zero-field spectral position of the exciton peak and c_d, the rate of the shift, is a material parameter proportional to the square of the size of the exciton wave-function in the plane perpendicular to the field.

A first-order perturbation approach has been used in Ref. [76] to evaluate the dependence of diamagnetic energy shifts ΔE_d on the Bohr radius a_B and reduced

mass μ for a hydrogen-like exciton in bulk semiconductors:

$$\Delta E_d = \left(\frac{e^2 a_B^2}{4\mu}\right) B^2 = \left(\frac{4\pi^2\hbar^4\epsilon^2\epsilon_0^2}{e^2\mu^3}\right) B^2 \tag{2.35}$$

Where ϵ and ϵ_0 are the static dielectric constants and permittivity of vacuum, respectively.

2.5.2 Zeeman Splitting

The Zeeman effect describes the splitting of degenerate magnetic levels when a magnetic field is applied [66]. Excitons with a non-vanishing magnetic momentum at B=0, which can come from the electron and hole spin, exhibit Zeeman splitting. For excitons with an s-envelope function the difference or the sum of the electron and hole g-factors enters:

$$\Delta E = \frac{1}{2}|g_e \pm g_h|\mu_B B \tag{2.36}$$

At weak magnetic fields the dependence of the exciton energy E_{ex} on the magnetic strength B can be described in terms of the combination of linear Zeeman effect and quadratic diamagnetic shift:

$$E_{ex}(B) = E_{ex}(0) \pm \frac{1}{2} g\mu_B B + c_d B^2 \tag{2.37}$$

2.6 Polaritons

In direct semiconductors with dipole-active excitons there exists a strong coupling of free excitons with photons of the same energy. This coupling has been pointed out by Hopfield [77]. The coupling of a photon with energy $E = \hbar ck$ and an exciton results in a mixed-mode excitation called an exciton-polariton with a two-branch dispersion curve in k-space and can be described in terms of the dielectric function $\epsilon(k, E)$ [78]:

$$\epsilon(k, E) = n^2(k, E) = \frac{\hbar^2 k^2 c^2}{E^2} = \epsilon_0 + \frac{4\pi\beta E_T(k)^2}{E_T(k)^2 - E^2} \tag{2.38}$$

where k and E are the polariton wave vector and energy, respectively. ϵ_0 is the dielectric constant and n is the refractive index. $4\pi\beta$ and $E_T(k)$ are the oscillator

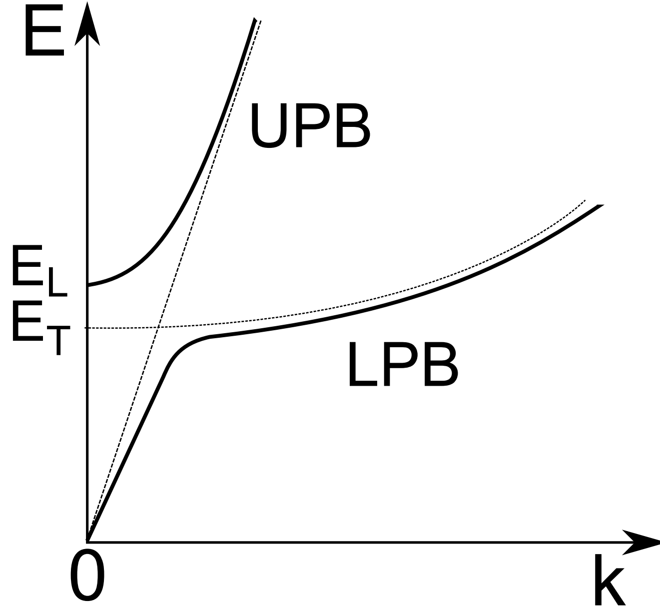

Figure 2.9: Dispersion curves for photons, free excitons (dashed curves) and polaritons (solid curves).

strength and the transverse exciton energy. In Chapter 5 $4\pi\beta$ is also referred to as polarisability according to Refs. [79, 80]. For a parabolic exciton band, $E_T(k) = E_T(0) + \frac{\hbar^2 k^2}{2\mu}$, where μ is the reduced mass of the exciton. The solutions of Eq. 2.38 lead to two polariton branches which are shown in Fig. 2.9. The two branches are called the upper and lower polariton branches and labelled UPB and LPB, respectively, in Fig. 2.9. The longitudinal exciton energy E_L can be determined from $\epsilon(0, E = E_L)$=0.

In the LPB the polaritons are predominately exciton-like at large wave vectors and photon-like at small wave vectors. This situation is inversed for the UPB. When excited, polaritons usually end up at the LPB. These polaritons relax towards lower energies (photon-like region) by scattering with phonons via their exciton component. These photon-like polaritons interact only weakly with the crystal and then rapidly exit the crystal. Toyozawa [81] pointed out that polaritons could accumulate at a "bottleneck" near the transverse exciton energy E_T where their lifetimes are the longest. The polaritons above this bottleneck posses a large exciton component and have short lifetime as a result of strong scattering with phonons. As the polaritons become more photon-like the scattering decreases. Once their energy is below E_T they can easily escape the sample. Thus the polariton distribution function has a peak near its bottleneck. In contrast polariton population in the UPB can directly contribute to the luminescence via

escape from the sample at the surface. UPB polaritons provide a path whereby LPB polaritons can rapidly escape the crystal if a mechanism exists which populates the UPB states.
Steiner el al. [82] suggested a scattering mechanism resulting from elastic neutral donor scattering in GaAs. In crystals with a large concentration of donors, polaritons having energies either above or below the bottleneck energy have a means of rapidly reaching the surface of the sample. The neutral donor scattering cross section for polaritons has a peak in the bottleneck region, which coupled with a smaller group velocity in this energy region results in a delay in the arrival of these polaritons at the sample surface. Thus these polaritons are impeded from diffusing to the surface by neutral donor scattering. The result is a dip in the exciton-polariton luminescence of samples with large donor concentrations, due to the slower journey of these polaritons depopulation by inelastic scattering or trapping occurs in this energy region. The result is a doublet lineshape. In samples with lower neutral donor concentration, dip polaritons reach the surface more easily, while high energy LPB polaritons cannot easily be scattered to the UPB hindering their escape from the crystal, resulting in a single peak in the luminescence spectrum [82].

Chapter 3

Experimental Techniques

This chapter presents details of the different experimental techniques used in this work to study the chalcopyrite semiconductors $CuInSe_2$, $CuInS_2$ and $CuGaSe_2$. It gives information on the crystal growth of the studied single crystals and explains the set-ups used to obtain their photoluminescence. The photoluminescence experiments were carried out at the University of Strathclyde and Grenoble High Magnetic Field Laboratory (GHMFL).

3.1 Sample Growth

The following sections deal with the growth of the studied chalcopyrite samples. The $CuInSe_2$ and $CuGaSe_2$ sample growth was performed by Dr. Yakushev at the University of Salford whereas the examined $CuInS_2$ crystals were grown in Dr. Alexander Mudryi's group at the Scientific-Practical Material Research Centre of the National Academy of Science of Belarus. The $CuInSe_2$ and $CuGaSe_2$ samples were grown by the vertical Bridgman method whereas for the growth of $CuInS_2$ the Travelling Heater Method (THM) was applied.

3.1.1 Bridgman Method

The crystal growth basically consisted of two steps in two different furnaces and is explained for $CuInSe_2$ with further details given by Ref. [83]. At first, the starting materials (purity of 99.999%) were mixed and introduced into a quartz ampoule which was then sealed under vacuum. The sealed ampoule was inserted into a horizontal rocking furnace and then heated to 200° C and maintained at this temperature for 4 hours. The temperature was then raised to 1080° C

($CuInSe_2$ melting point at $\sim 980^\circ$ C) and held at this temperature for 24 hours while simultaneously rocking the furnace to ensure complete mixing i.e. chemical reaction of the elements. After the heating treatment, the ampoule was rapidly cooled to room temperature.
For the second step of the sample growth, a two zone furnace is mounted on a lathe bed to give vertical translation with the ampoule fixed in position. The charge of pretreated $CuInSe_2$ was powdered and subsequently mounted in a thick walled quartz ampoule in the hot zone and heated to temperatures of 1050° C at a rate of 80° C/h. The temperature of the cold zone is about 900° C and the temperature gradient between both zones is between 15 and 20° C/cm. After 24h at 1050° C the temperature was dropped to 1000° C and the furnace was moved over the ampoule at a rate of 1mm/h until the whole ampoule is located in the cold zone. Following the crystal growth the ampoule is cooled at a rate of 1° C/h down to 750° C and then down to 650° C at a rate at 2° C/h. Below 400° C a higher cooling rate of 6° C/h was employed. The total furnace time is about 24 days.

3.1.2 Travelling Heater Method

The THM is a solution growth technique often referred to as "off-stoichiometric zone melting" [84]. The mechanism of zone melting with steady state crystallisation from a small liquid zone that is fed by a source ingot having the same composition as the crystal to be grown is used. This principle is combined with the advantage of low temperature growth from a suitable solution.
Indium as the zone solvent and the polycrystalline $CuInS_2$ ingots for the feed were inserted into a carbon coated quartz ampoule. The ampoule was subsequently evacuated and sealed. The ampoule was then placed in a vertical THM furnace with three coil heaters and the maximum temperature was set to the value where the Indium solution becomes a single liquid phase. The crystal growth is performed by lowering the ampoule by 4mm/day for 10 days where the temperature gradient at the point of growth was set to 40-80° C/cm [85].

3.2 X-Ray Crystal Orientation: Laue Method

The orientation of the three main cubic structure crystallographic axes <100>, <010> and <001> of the $CuInSe_2$ and $CuInS_2$ single crystals has been obtained

by the analysis of x-ray Laue patterns. The analysis was performed by Dr. Yakushev at the Scientific-Practical Material Research Centre of the National Academy of Science of Belarus. The Laue method is suitable for the determination of orientation and symmetry of single crystals. Fig. 3.1 shows a schematic of a typical Laue reflection setup. A parallel beam of polychromatic x-rays (continuous spectrum from, for example, a copper target tube running at 35 kV [86]) is directed onto the surface of a fixed single crystal. Each reflecting crystal plane selects a wavelength of the incident beam which satisfies Bragg's law. The diffracted beams, forming the diffraction pattern, reproduce the structural properties of the crystal. The Laue pattern can be recorded by a photographic film. The positions of the diffraction spots give the directions of the various diffracted beams and the resulting Laue pattern is a projection of the reciprocal crystal lattice. For the correct orientation of the single crystal its symmetry will be visible in the diffraction pattern. By placing the film on the same side as the X-ray beam in Fig. 3.1, back reflection patterns can be recorded. The back reflection configuration is used for thick samples where transmission is not possible. More details on the Laue method can be found in Refs. [86, 87].

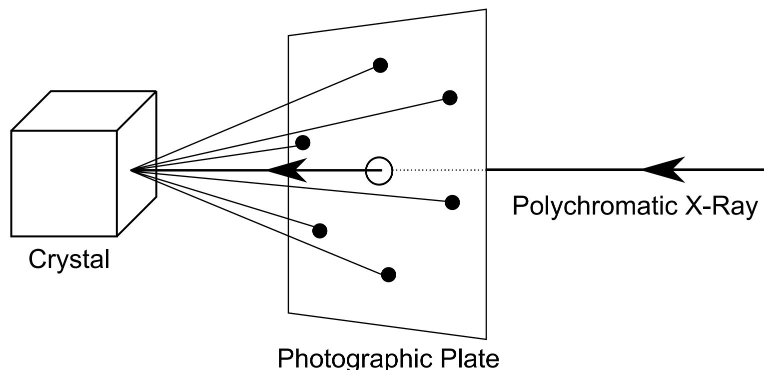

Figure 3.1: Schematic of the Laue method

3.3 Energy Dispersive X-Ray Spectroscopy

Energy dispersive x-ray spectroscopy (EDX) is an analytical technique which can be used for the chemical analysis of a sample in a scanning electron microscope and/or electron microprobe. EDX was used to determine the elemental composition of the studied chalopyrite single crystals. The EDX measurements of the $CuInSe_2$ and $CuInS_2$ single crystals were performed at the University of Salford and at the Scientific-Practical Material Research Centre of the National Academy

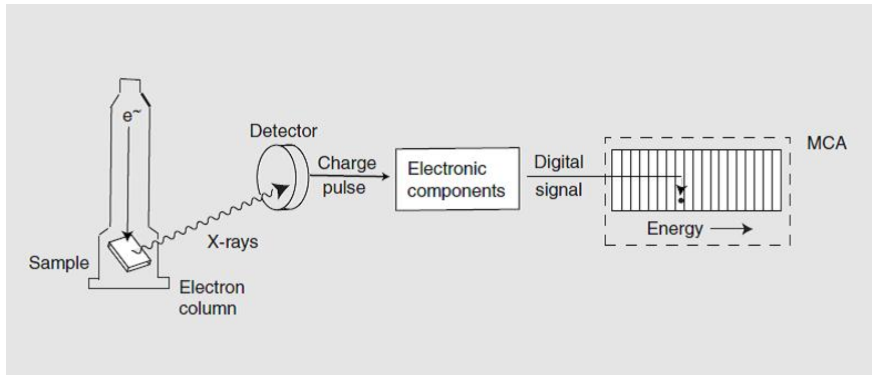

Figure 3.2: Schematic of a EDX detection system, taken from Ref. [88].

of Science of Belarus, respectively. EDX measures the energy and intensity distribution of an x-ray signal generated by a focused electron beam. With EDX the characteristic x-ray emission lines are sorted electronically rather than by means of a diffraction crystal as used in wavelength dispersive x-ray spectroscopy. The EDX detection system, schematically shown in Fig. 3.2, is responsible for the conversion of the x-ray emission to analysable data. An x-ray photon produces a charge pulse in a semiconductor detector. This charge pulse is then converted into a voltage pulse whose amplitude reflects the energy of the detected x-ray. The voltage pulse is converted into a digital signal which causes one count in a corresponding channel of a multichannel analyser. In order to extract quantitative information the analysis comprises of certain steps such as the accounting for false peaks, identification of the elements giving rise to the spectrum, background removal, resolution of the spectral peak and computation of the elemental concentrations. Further details on EDX can be found in Refs. [88, 89].

3.4 Photoluminescence Spectroscopy

This section presents the experimental set-ups used for the PL study of the chalcopyrite semiconductor. Temperature and excitation power dependent PL measurements were performed at the University of Strathclyde whereas additional excitation power and magnetic strength dependent PL measurements were taken at GHMFL. The PL data was collected during three visits to the GHMFL.

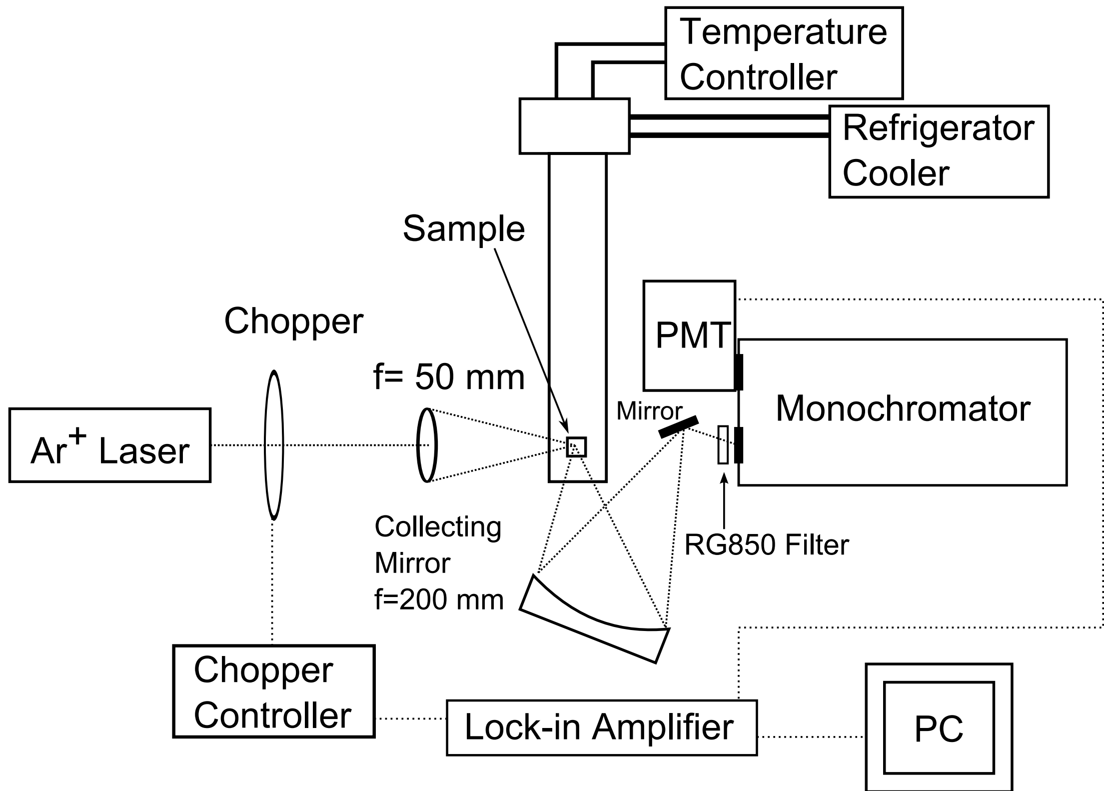

Figure 3.3: Schematic of the PL setup used in Strathclyde

3.4.1 PL-Set-up Strathclyde

An Ar^+ ion laser with an emission wavelength of 514 nm was used to excite the $CuInSe_2$, $CuInS_2$ and $CuGaSe_2$ samples. The excitation power was varied in the range from 20 mW to 200 mW (laser output) which corresponds to power densities from 43 to 430 W/cm^2 on the sample using an estimated laser spot diameter of 0.1 mm and accounting for the transmission through the chopper, filters and cryostat windows. Smaller excitation powers can be achieved by using a set of neutral density filters. The laser line was focused onto the sample by a single lens. The PL emission was collected by a concave mirror and then focused onto the slits of a 1 m single-grating monochromator (Monospec 1000) with a 600 grooves/mm (used for $CuInSe_2$) or 1200 grooves/mm grating (used for $CuInS_2$ and $CuGaSe_2$). Tables 3.1 and 3.2 summarise the spectral bandwidth for the different slit widths for the 600 grooves/mm and 1200 grooves/mm grating, respectively.
In order to cut off scattered laser light RG filters were placed in front of the monochromator entrance slit. A near-infrared photomultiplier tube (Hamamatsu H10330-75 for $CuInSe_2$ and Hamamatsu R636 $CuInS_2$ and $CuGaSe_2$) was used as a detector and the signal processed using a lock-in amplifier.

Slit Width (mm)	Spectral Resolution in nm	Spectral Resolution in meV
0.15	0.25	0.20
0.175	0.3	0.24
1.5	2.5	2.0

Table 3.1: The spectral bandwidths for the different slit widths of a 1 m single-grating monochromator with a 600 grooves/mm grating blazed at 1000 nm used for the $CuInSe_2$ PL spectra.

Slit Width (mm)	Spectral Resolution in nm	Spectral Resolution in meV
0.15	0.12	0.10
0.2	0.17	0.14
0.25	0.21	0.17
0.3	0.25	0.2
0.5	0.42	0.3

Table 3.2: The spectral bandwidth for different slit widths of a 1 m single-grating monochromator with a 1200 grooves/mm grating used for the $CuInS_2$ and $CuGaSe_2$ PL spectra.

The sample was cooled in a closed-cycle cryostat (Advanced Research Systems). The temperature in the cryostat was measured by a sensor placed at the sample holder and another one mounted on the cold-finger base. A temperature controller worked with the two sensors and a heater in order to adjust the temperature in a range of ∼5 K up to room temperature. The sample was measured under vacuum conditions, using a system with diffusion and rotary pumps. For the reflectivity measurements a 100 W tungsten halogen lamp was used instead of the laser.

3.4.2 PL-Set-up GHMFL

The magneto-optical PL measurements at GHMFL were carried out using a water cooled resistive magnet in a liquid helium bath cryostat, allowing magnetic fields up to 22 T at 4.2 K. The sample was mounted on a sample holder as shown in Fig. 3.5 and inserted into a shroud. The shroud was then evacuated and subsequently filled with Helium up to a pressure of ∼ 200 mbar. Fibre optics were used to transport the 514 nm line of an Ar^*/Kr laser to the sample and the PL to the entrance slit of a 0.5 m spectrometer. The diameters of the excitation and collection fibre were 0.2 mm and 0.3 mm, respectively. A photo of the sample holder and the optical fibres can be seen in Fig. 3.5.

In addition to the magneto-optical PL measurements, excitation power depen-

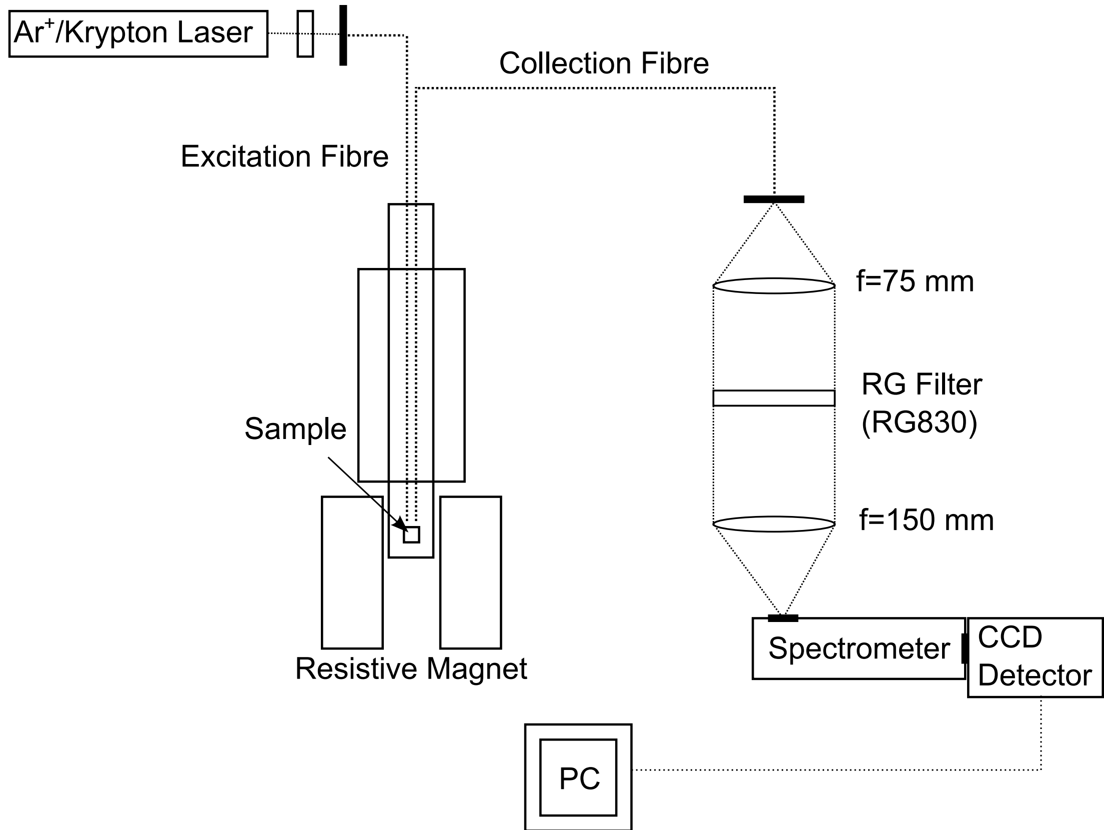

Figure 3.4: Schematic of the PL setup used at GHMFL

dent PL spectra were taken. Therefore excitation power was varied in the range of 5 mW to 50 mW, corresponding to power densities from 15 to 160 W/cm^2, by using a neutral density filter wheel.

The PL was focused as shown in Fig. 3.4 on the slits of 0.5 m triple-grating spectrometer (Princeton Instruments Acton SP2500i) with a 600 grooves/mm grating blazed at 750 nm. The dispersed light was then collected by a cooled 1024 element InGaAs array (Princeton Instruments Acton). The spectral resolution of this system is limited by the resolution[1] [2] of the array of 0.17 nm. For the detection of $CuInS_2$ and $CuGaSe_2$ PL the same spectrometer with a 1800 grooves/mm grating blazed at 500 nm was used. The dispersed light was detected by a cooled 1340 Si CCD (Princeton Instruments Acton) with a spectral resolution[3] of approximately 0.03 nm. Table 3.3 summarises the values of the spectral resolution.

[1]Assuming a bandwidth per pixel of 0.07 nm and a pixel resolution of 2.5 pixel for a 20μm slit

[2]http://www.princetoninstruments.com/spectroscopy/calculator/

[3]Assuming a bandwidth per pixel of 0.013 nm and a pixel resolution of 2.5 pixel for a 20μm slit

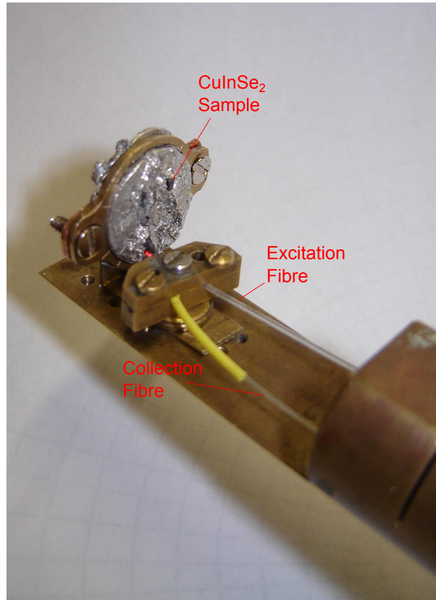

Figure 3.5: Photo of the sample holder and the optical fibers used at the GHMFL

Detector	Resolution in nm	Resolution in meV
InGaAs	0.17	0.14
Si	0.03	0.04

Table 3.3: The spectral resolution for the InGaAs and the Si CCD used at GHMFL.

Chapter 4

$CuInSe_2$

$CuInSe_2$ is a ternary chalcopyrite semiconductor with a direct band gap used in the absorber layers of solar cells currently holding the efficiency record of 20% for thin-film photovoltaic devices. In this chapter the results of temperature and excitation power dependent PL measurements of excitonic features in $CuInSe_2$ are presented which provide information about the free excitons and on the nature of defects associated with the bound excitons.
In addition, the results of the $CuInSe_2$ magneto-PL measurements which have been performed at the GHMFL are presented. The diamagnetic shift rates for different crystal directions of the A and B FE were used to calculate the reduced exciton masses.
Bulk single crystals of $CuInSe_2$ were cleaved from the central part of an ingot grown by the vertical Bridgman technique (Chapter 3.1.1). The typical elemental composition of the crystals was measured via EDX to be close to the ideal stoichiometry (Cu: 25, In: 25 and Se: 50 at. %). The EDX measurements were performed at the University of Salford.
The experimental results of this chapter have been accepted and prepared for publication in Refs. [90] and [91], respectively.

4.1 Excitons in $CuInSe_2$

The near band-edge reflectivity (RF) and PL spectra taken at 4.5 and 4.2 K, respectively, are shown in Fig. 4.1. The RF spectrum, Fig. 4.1 (a), contains two prominent resonances due to the A and B free excitons. This allows the two lines in the PL spectrum appearing at similar energies to be assigned to radiative recombination of free excitons associated with the A and B valence sub-bands

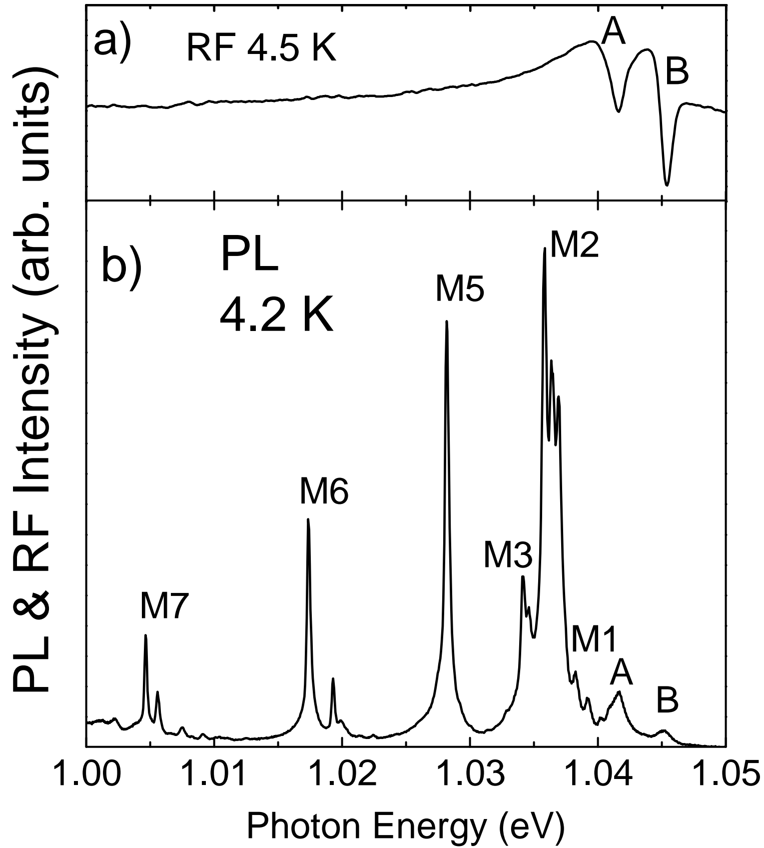

Figure 4.1: RF (a) and PL (b) near band-gap spectra for $CuInSe_2$ single crystals, taken at 4.5 K and 4.2 K, respectively.

(Chapter 2.1.2). The A and B lines occur at 1.0416 and 1.0451 eV, respectively. In addition to the free exciton lines, the PL spectrum reveals a number of sharp lines labelled M1 to M7. Some of these lines have been observed earlier [27, 29, 30, 92] and tentatively assigned to ground and excited states of excitons bound to shallow defects. The excitons appear as multiplets and the highest intensity lines are labelled as M1 (1.0383 eV), M2 (1.0358 eV), M3 (1.0341 eV), M5 (1.0282 eV), M6 (1.0174 eV) and M7 (1.0046 eV), using the notations introduced previously. [30,92] For a detailed analysis of the $CuInSe_2$ PL spectra the lines have been fitted with Lorentzian curves using the Levenberg-Marquardt least-square fitting method, as shown in Fig. 4.2. Generally, the line width of an exciton is determined by processes which limit the time that the exciton spends in the $\mathbf{k}=0$ state, including phonon scattering. For weak exciton-phonon coupling the line shape can be described by a Lorentzian curve, whereas a Gaussian curve occurs where there is strong exciton-phonon coupling (see Chapter 2.4.1) [67]. The Lorentzian shape of the observed excitonic PL lines suggests low exciton-phonon coupling and a low concentration of crystal imperfections and impurities. A Gaussian

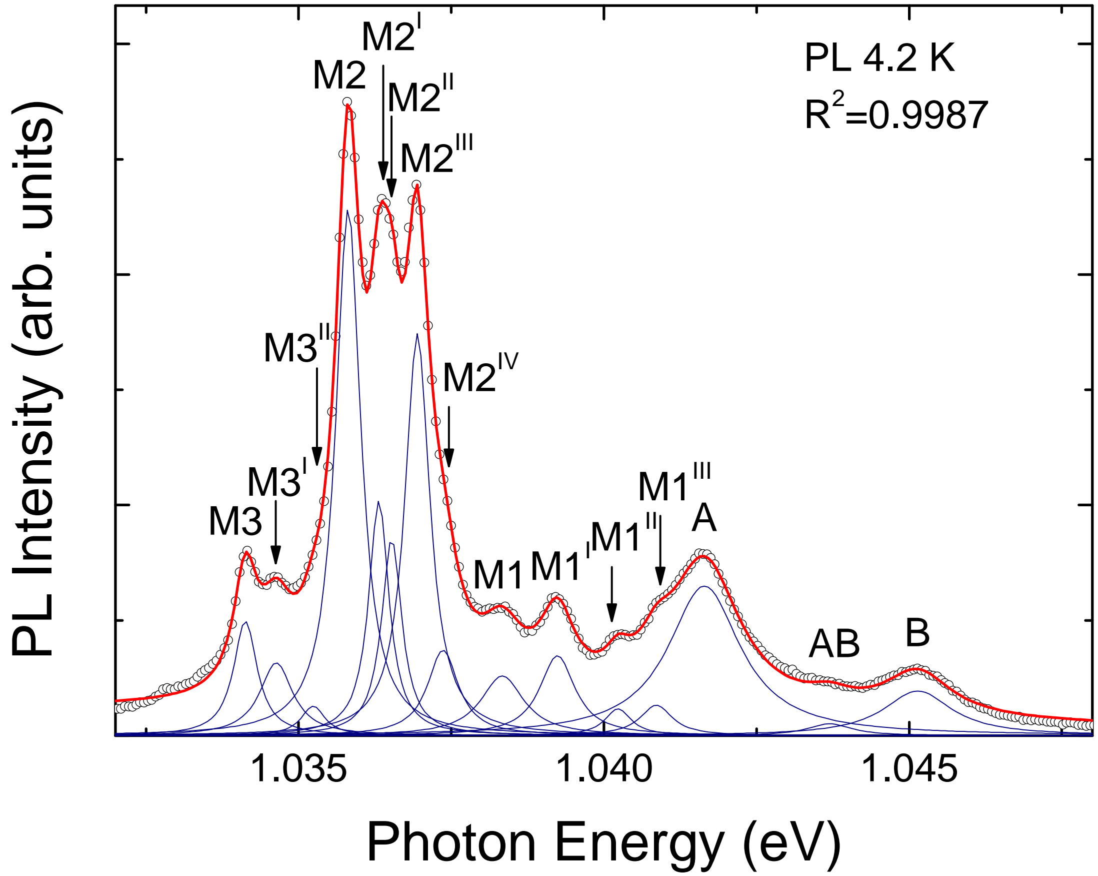

Figure 4.2: Fit of the high quality $CuInSe_2$ spectrum with Lorentzian line shapes (circles-data, blue-individual Lorentzian and red-fit line.

line shape of the A and B free exciton lines was reported by Chatraphorn et al. (Ref. [27]) and was attributed to a high concentration of defects rather than strong exciton-phonon coupling.

Fig. 4.2 shows that at low temperature the M1, M2 and M3 excitonic multiplets can be decomposed into 4, 5 and 3 peaks, respectively. Lines such as $M1^{III}$, $M2^{III}$, $M2^{IV}$, $M3^{II}$ and $M3^{I}$, which can be seen in Fig. 4.2, have not been reported previously. In addition, a broad and poorly resolved PL line, labelled as AB in Fig. 4.2, appears at 1.0435 eV between the two free exciton lines. This PL line could be tentatively associated with an unresolved polaritonic structure of the A and B free excitons. Polariton splitting of the A free exciton has been reported for $CuInS_2$ [33] and in Chapter 5. On the other hand, the AB line could be due to the radiative recombination of a biexciton related to the B free exciton. Biexciton recombination of the A free exciton has been observed in $CuInS_2$ by Wakita et al. [93].

The accuracy of the obtained fitting parameters as well as the quality of the fit is

indicated by the square of the correlation coefficient R^2=0.9987, whose value is very close to unity. However, with increasing temperatures the spectral position as well as the width of the excitonic lines change and it becomes more difficult to obtain accurate fitting information for the less resolved and/or low intensity lines such as AB, $M1^{III}$, $M1^{II}$, $M2^{IV}$, $M2^{II}$, $M3^{II}$ and $M3^{I}$. The spectral positions and FWHM of all the lines included in the fit to the PL spectrum in Fig. 4.2, are shown in Table 4.1. The FWHM of the M lines varies between 0.4 and 0.9 meV whereas it is about 1.4 meV for the A and B free excitons and 1.8 meV for the AB line. The small value of the FWHM of the M lines suggests that they are of bound excitonic nature.

The assignment of the M lines in Fig. 4.2 to phonon replica can be ruled out at this point. Tanino et al. (Ref. [94]) reported a minimum phonon energy of 7.44 meV for optical and acoustical phonons in $CuInSe_2$ whereas the examined spectral region is of about 7.6 meV. In order to clarify the nature of the excitonic lines shown in Fig. 4.2 excitation power and temperature dependent PL measurements have been performed.

PL line	**Energy (eV)**	**FWHM (meV)**	**Assignment**
B	1.0451	1.4	FE
AB	1.0435	1.8	FE
A	1.0416	1.4	FE
$M1^{III}$	1.0409	0.6	BE_1
$M1^{II}$	1.0402	0.5	BE_1
$M1^{I}$	1.0392	0.7	BE_1
M1	1.0383	0.9	BE_1
$M2^{IV}$	1.0374	0.6	BE_2
$M2^{III}$	1.0369	0.7	BE_2
$M2^{II}$	1.0365	0.4	BE_2
$M2^{I}$	1.0362	0.4	BE_2
M2	1.0358	0.5	BE_2
$M3^{II}$	1.0352	0.5	BE_3
$M3^{I}$	1.0346	0.7	BE_3
M3	1.0341	0.5	BE_3

Table 4.1: Spectral positions, FWHM and the assignment of the PL lines obtained by least-square fitting the $CuInSe_2$ spectrum, taken at 4.4 K, with Lorentzian curves.

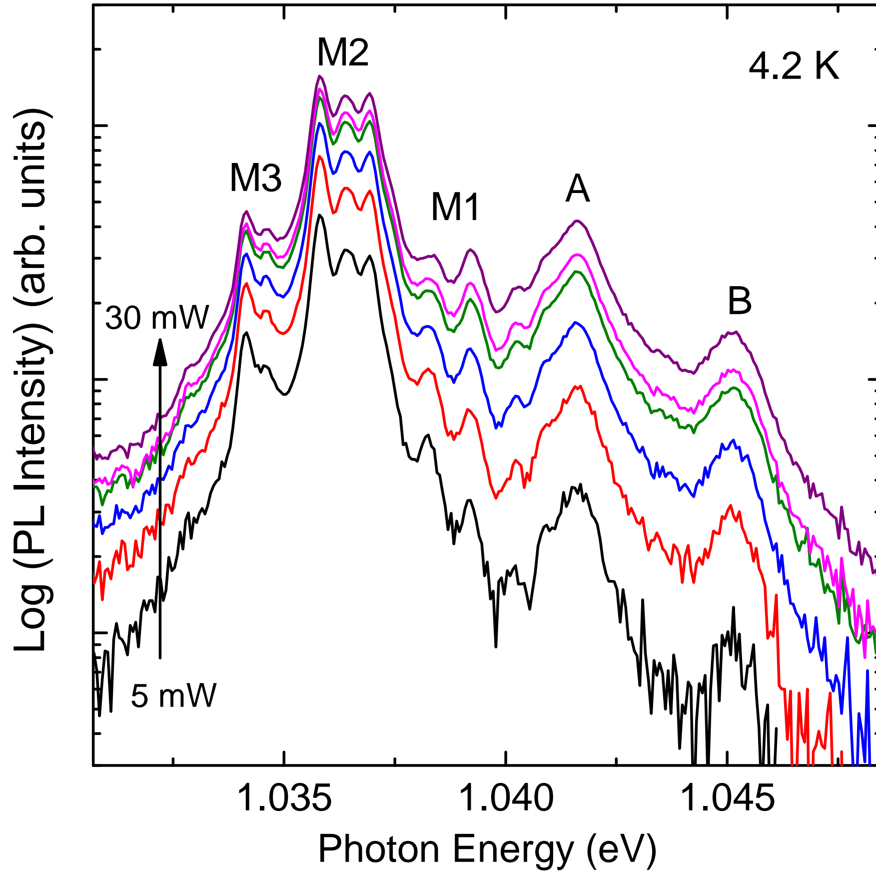

Figure 4.3: Excitation power dependence of the $CuInSe_2$ PL spectra, taken at 4.2 K.

4.2 Excitation Power Dependence

Excitation power dependent PL measurements were performed at liquid Helium temperature for excitation powers ranging from 5 to 30 mW (corresponding to a range from 16 to 100 W/cm^2) at the GHMFL and are shown in Fig. 4.2. As it can be seen in Fig. 4.2, the spectral position of the PL lines does not depend on the excitation power and changes in the line width are very small. For example the Lorentzian of the M2 excitonic line increases its FWHM from 0.45 to 0.49 meV with excitation densities increasing from 16 to 100 W/cm^2. This makes it possible to obtain reliable fitting parameters even for the less resolved PL lines.

4.2.1 Excitation Power Dependence of the Intensity

From the fit of each individual spectrum the dependencies of the integrated PL intensity I of the free and bound excitonic lines, on the laser excitation power P have been obtained, as plotted in Figs. 4.4 and 4.5. The dependencies follow

the power law $I \sim P^k$. A value of k between 1 and 2 is expected for free exciton transitions as mentioned in Chapter 2.4.3. Values of k between 1 and 2 are also expected for bound exciton transitions, assuming the concentration of defects is high enough and no saturation occurs. For the A and B free excitons, the AB line as well as for the components of the M1 bound exciton, power coefficients $1 < k_1 < 2$ have been determined, as summarised in Table 4.2. The dependence of the integrated intensity on the excitation power of the A, B, AB and M1 excitonic lines does not show any saturation which confirms that the sample temperature did not rise with increasing excitation and also indicates that the concentration of defects involved in the M1 bound exciton formation is high.

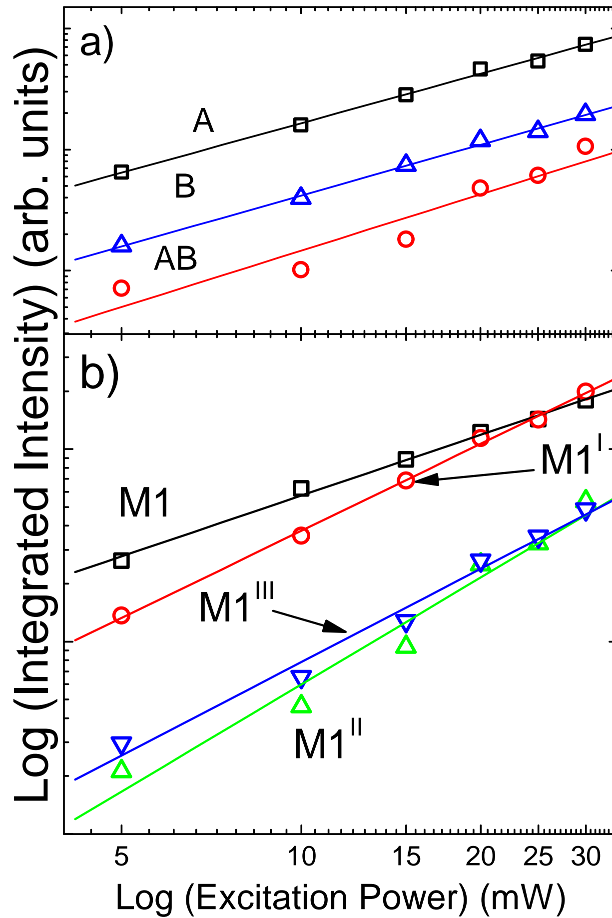

Figure 4.4: Dependence of the PL inetnsity on the excitation power of the free excitons (a) and the bound excitons involved in the M1 complex (b), fitted linearly

For the bound excitons involved in the M2 and M3 multiplets, with the exception of $M2^{IV}$, the power coefficients are smaller than unity. In addition, Fig. 4.5 shows a change in the excitation power dependence of the integrated intensity for these lines for powers above about 20 mW. The k coefficients for the M2

and M3 excitonic multiplets are summarised in Table 4.2, where k_1 corresponds to excitation powers below 20 mW and k_2 to excitation powers above 20 mW. Weber et al. [95] have reported similar behaviour, namely changes of the slope of the line in the logarithmic plot and $k < 1$, for excitons bound to isoelectronic defects in silicon. These similarities suggest that the M2 and M3 luminescence might originate from excitons bound to isoelectronic defects (see Chapter 2.2).

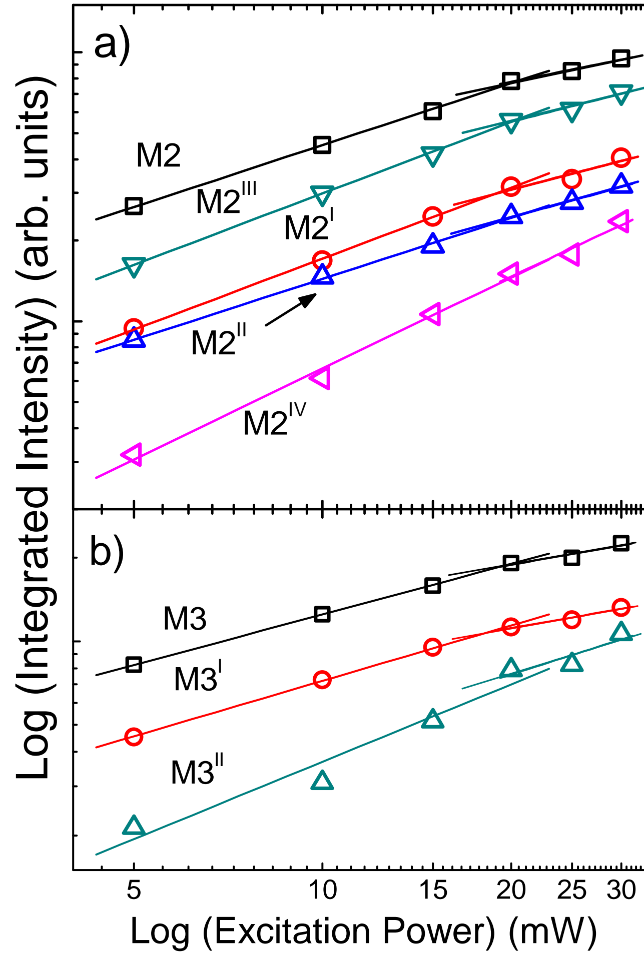

Figure 4.5: Dependence of the PL intensity on the excitation power of the M2 exciton (a) and M3 exciton complex, fitted linearly

Isoelectronic traps first capture a charge carrier to form an intermediate charged state which then attracts the opposite charge carrier forming a bound exciton. The number of excitons bound to isoelectronic defects is proportional to the concentration of either the electrons or holes and the number of defects, which produces a linear dependence of PL intensity on excitation power ($k \leq 1$). The change of slope at higher excitation powers can be explained by the saturation of the defects involved. In silicon these defects are foreign atoms isoelectronically

substituting host atoms, binding either holes or electrons to form a state in the forbidden gap [96]. For the chalcopyrite compound $CuInS_2$, which is closely related to $CuInSe_2$, Krustok et al. [97] reported emission of excitons bound to defects acting as isoelectronic traps, which were closely situated donor-acceptor pairs acting as neutral centers.

As seen in Fig. 4.5 (a) the excitation power dependence of the $M2^{IV}$ line differs from that of the other excitonic components of M2. A power coefficient $k > 1$ was obtained and $M2^{IV}$ does not saturate above 20 mW. These properties resemble those of the M1 excitons which indicates, that $M2^{IV}$ could be another M1 excitonic component or a separate exciton.

Thus the excitation power dependent PL measurements show that the A, AB and B lines can be associated with free excitons whereas the M1 components are excitons bound to shallow hydrogenic defects which have a high concentration. With the exception of $M2^{IV}$, the components of the M2 and M3 excitons seem to be bound to more complex defects which may have an isoelectronic nature and whose concentrations are lower than those associated with the M1 exciton.

PL line	**Energy (eV)**	$\mathbf{k_1}$	$\mathbf{k_2}$
B	1.0451	1.40	
AB	1.0435	1.55	
A	1.0416	1.36	
$M1^{III}$	1.0409	1.61	
$M1^{II}$	1.0402	1.85	
$M1^{I}$	1.0392	1.50	
M1	1.0383	1.05	
$M2^{IV}$	1.0374	1.12	
$M2^{III}$	1.0369	0.88	0.6
$M2^{II}$	1.0365	0.75	0.6
$M2^{I}$	1.0362	0.88	0.6
M2	1.0358	0.77	0.5
$M3^{II}$	1.0352	0.93	0.7
$M3^{I}$	1.0346	0.66	0.4
M3	1.0341	0.61	0.4

Table 4.2: Spectral positions and power coeffcients k_1 and k_2 (where k_1 corresponds to excitation powers below 20 mW and k_2 to excitation powers above 20 mW for the M2 and M3 excitons) of the $CuInSe_2$ PL lines obtained by fitting the data in Figs. 4.4 and 4.5 linearly.

4.3 Temperature Dependence

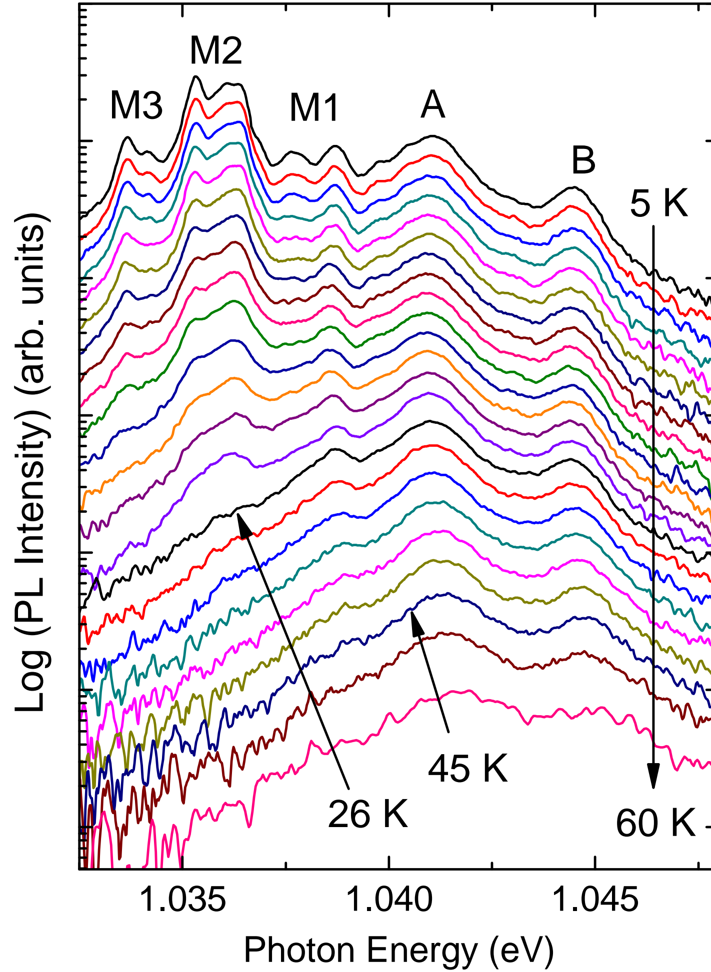

Figure 4.6: Evolution of the $CuInSe_2$ PL spectrum with temperatures increasing from 5 to 60 K

The temperature evolution of the PL spectra has been studied for a number of $CuInSe_2$ single crystals. Fig. 4.6 shows the evolution of the near band-edge PL spectrum with temperature increasing from 5 to 60 K for the highest quality sample. The rapid thermal quenching of the M lines confirms their assignment to the radiative recombination of bound excitons [27, 29, 30, 35]. In contrast to the M lines, the intensities of the A and B peaks decrease more slowly with increasing temperature and are still present at 60 K. This behaviour confirms the assignment of the A and B lines to free excitons associated with the A and B valence sub-bands.

The different M-lines are seen to quench at different rates. Fig. 4.6 shows that the

M2 and M3 lines have nearly disappeared by about 26 K, whereas the M1 lines are still visible up to about 45 K. The M1 multiplet has a spectral position very close to that of the A free exciton and, if these excitons are associated with the A valence-band, a fast thermal quenching of the M1 lines would be expected. Their slow quenching suggests that a free exciton associated with the B valence sub-band is involved in the formation of the M1 bound exciton, as will be discussed further below.

With increasing temperature, the PL lines change their spectral positions and broaden. Therefore the following more detailed analysis has been restricted to the most intense and clearly resolved excitonic PL lines: A, B, $M1^{I}$, M1, $M2^{III}$, $M2^{II}$, M2 and M3.

4.3.1 Temperature Dependence of the Spectral Position of the A and B free excitons

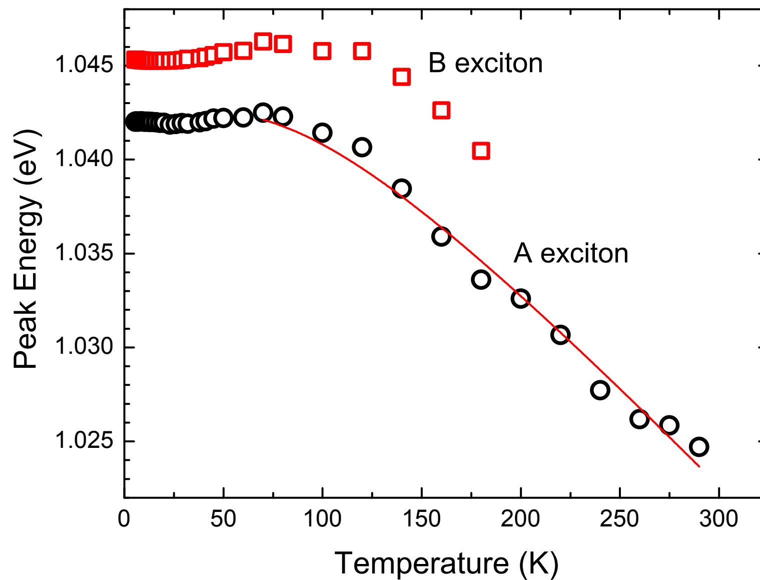

Figure 4.7: Temperature dependence of the A and B free exciton peak position with temperature increasing from 5 to 290 K (circles and squares - data and red- fit line with Eq. 4.1.

The evolution of the spectral position of the A and B free exciton peak under increasing temperature from 5.6 to 290 K is shown in Fig. 4.7. Up to 23 K no significant changes of the A and B FE peak position can be seen. For temperatures higher than 23 K, a blueshift of the A and B FE peak can be observed. At 70 K the value of the peak energy reaches its maximum before decreasing for higher temperatures. For temperatures above 70 K the peak position of the A and B free

exciton decreases due to phonon-electron interaction and the thermal expansion of the lattice, which result in a reduced bond energy of the crystal lattice and therefore lead to a red shift. The temperature dependent behaviour of the FE lines reflects the temperature dependence of the $CuInSe_2$ band gap. The temperature dependence of the A exciton for temperatures higher than 70 K can be described by [98]:

$$E_A(T) = E_A(0) - S\langle\hbar\omega\rangle\left[coth\left(\langle\hbar\omega\rangle/2kT\right) - 1\right] \tag{4.1}$$

where $E_A(0)$ is the exciton peak energy at 0 K, S a dimensionless electron-phonon coupling parameter (Huang-Rhys) and $\langle\hbar\omega\rangle$ is the average phonon energy. The fit resulted in S=0.66 ±0.05 and $\langle\hbar\omega\rangle$=26 ± 3 meV.

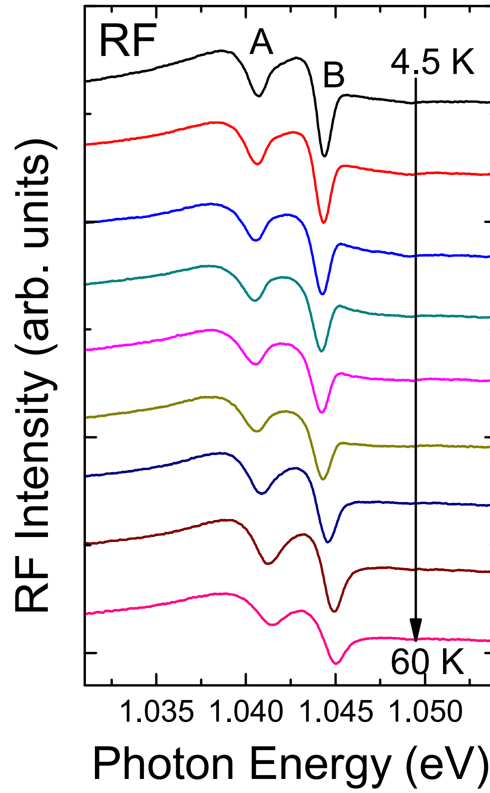

Figure 4.8: Evolution of the $CuInSe_2$ RF spectrum with temperature increasing from 4.5 to 60 K.

Tanino et al. [94] reported 13 optical phonon modes at 100 K, varying from 60 (7.4 meV) to 233 cm^{-1} (28.9 meV). The strongest mode was found at 178 cm^{-1} which corresponds to 22.1 meV which is close to the value of 26 ± 3 meV obtained by the fit to Eq. 4.1. Further optical phonon modes with energies ranging from 23.3 to 28.8 meV were found and are in good agreement with the value determined by the fit.

From Fig. 4.7 it can be seen that Eq. 4.1 describes the experimental points for temperatures higher than 70 K well. However, for temperatures below 70 K the temperature dependence of the FE peaks shows an anomalous behaviour as reported earlier by Binsma [26] and also observed in this work (Chapter 5.3.1) for $CuInS_2$. A possible explanation for the blueshift of the A and B FE peak for temperatures greater than 26 K is given by Deus et al. [99]. The authors reported a negative expansion coefficient of the lattice parameters a and c of $CuInSe_2$ at temperatures of 60 and 80 K, respectively. For temperatures below 60 and 80 K, the determination of the the expansion coefficient became inaccurate. However, negative thermal expansion coefficients were also reported for $CuInS_2$ for temperatures below 100 K [100]. In Chapter 2.1.2 it was mentioned that the anomalous

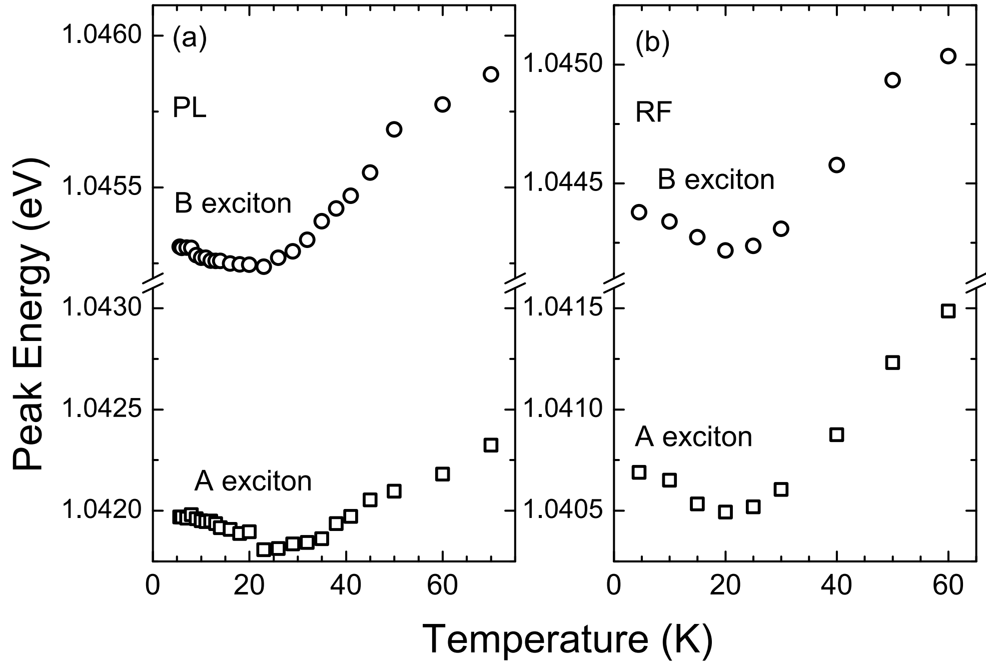

Figure 4.9: Temperature dependence of the A and B free exciton peak position with temperatures increasing from 5.6 to 70 K (a) from the PL spectra in Fig. 4.6 and (b) from the RF spectra in Fig. 4.8.

behaviour of the band gap could be influenced by the p-d hybridization. With increasing temperature, the lattice expands and the distance between the atoms increases which result in a decrease of the p-d hybridization and thus an increase of the band gap occurs. Both possible explanations are based on the thermal expansion of the lattice which are of opposite character.

In Fig. 4.8 the evolution of the $CuInSe_2$ RF spectrum is shown with temperatures increasing from 4.5 to 60 K. It can be seen in this figure that the resonance of

both excitons exhibit a temperature dependent shift of their spectral position and broadening. In order to fully describe the temperature dependent behaviour of the FE resonance a theoretical model is needed which will be the subject of future work. In order to examine the temperature dependence of the spectral positions of the FE resonances their minimum has been plotted versus temperature in Fig. 4.9 (b).

The evolution of the PL peak positions of the A and B free excitons with temperature increasing from 5.6 to 70 K is shown in Fig. 4.9 (a). Fig. 4.9 (b) shows the temperature dependence of the spectral position of the minimum of the A and B FE RF resonances for a temperature range of 4.5 to 60 K. As can be seen in Fig. 4.9 (a) and (b), the dependence of the spectral positions on temperature of the PL peaks and the minimum of the RF resonances for the A and B FE are in good agreement.

For both excitons a redshift of $\sim$ 0.1 meV and $\sim$ 0.2 meV can be observed for temperatures up to 23 K and 20 K in Fig. 4.9 (a) and (b), respectively. This redshift is then followed by a blue shift up to 70 K (60 K in Fig. 4.9 (b)). Alloy broadening and fluctuations in the $CuInSe_2$ composition can cause potential fluctuations and lower energy tail states. At low temperatures (5.6 to 23 K for the PL) charges carriers can relax into these lower energy tails states before they recombine and thus, produce a red shift. A similar behaviour has been observed in $CuInS_2$ (Chapter 5) and in ternary III-Nitride alloys such as InGaN [101] or AlGaN [102].

4.3.2 Temperature Dependence of the Intensity

This section deals with the dependence of the integrated intensity of the FE and BE (M1 to M3) on the temperature. As mentioned in Section 2.4.2 the study of the temperature dependence of excitonic luminescence can provide information on the activation energy of the underlying process.

4.3.2.1 Free Excitons

Fig. 4.10 plots the integrated intensity of the A and B free exciton lines versus inverse sample temperature. The temperature quenching of excitonic lines is due to the thermally activated depopulation of the excitonic level and/or to the activation of nonradiative recombination centres [71]. An Arrhenius plot can be used to determine the activation energies E_{a1} of the processes involved. Assuming only

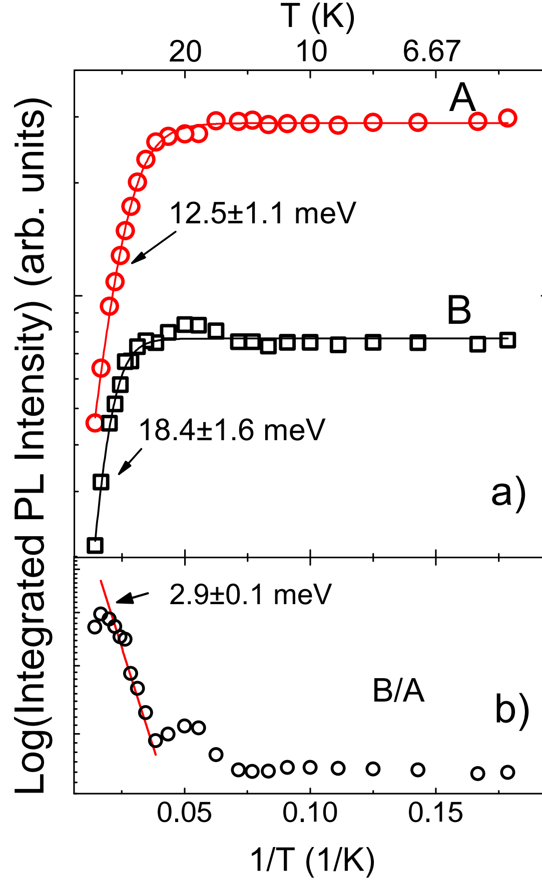

Figure 4.10: Arrhenius plot of integrated intensity of the A and B free excitons, fitted with Eq.2.20 (a) and the ratio of the integrated intensities of the B and A free excitons (b).

one nonradiative activation channel, the dependence of the integrated intensity I on the temperature T can be described by Eq. 2.20 in Chapter 2.4.2.
Measurements on other semiconductor materials, such as GaN, have demonstrated values of activation energies for the A exciton that are closely matched to the binding energy of the A exciton [71].
The values of E_{a1} and a_1 obtained by the least-square fit of the $CuInSe_2$ data shown in Fig. 4.10, are given in Table 4.3. The best fit to the experimental points for the A exciton in this $CuInSe_2$ single crystal yields an activation energy of 12.5 meV. Chatraphorn et al. [27] determined a value of 12 meV for the activation energy of the A exciton which is in good agreement with this value. However, the temperature quenching analysis of the A free exciton line of lower quality $CuInSe_2$ crystals resulted in smaller activation energies with a minimum value of about 6 meV. In addition, Yakushev el al. [35] reported an activation energy of 7.7 meV for a $CuInSe_2$ sample of a lower quality. Thus, values for E_{a1}

for this material are spread over quite a range and are not well matched to the value of the binding energy of the A free exciton, which has been determined as 8.5 meV from the spectral position of the excited states [103]. The temperature

PL line	$\mathbf{E_{a1}}$ (meV)	$\mathbf{a_1}$
B	18.4	52
A	12.5	43

Table 4.3: Activation energy E_{a1} and process parameter a_1 of the A and B FE in $CuInSe_2$ determined from the fit in Fig. 4.10 with Eq. 2.20.

dependence of the integrated intensity of the B exciton has also been fitted using Eq. 2.20. An activation energy of 18.4 meV was obtained for the highest quality $CuInSe_2$ single crystal, whereas smaller values down to 7 meV were determined for crystals of lower quality. Literature values of the B exciton activation energy determined from the temperature quenching, range from 7.9 [35] to 17 meV [27]. As with the A exciton the value of the binding energy of the B exciton (8.4 meV Ref. [103]) occurs at a considerably lower energy than E_{a1} for the best crystals. There are a number of possible explanations for the observed scatter of measured activation energies and the differences from the exciton binding energies. The A and B free excitons are separated by a very small energy splitting (3.3 meV in Fig. 4.6 and 3.5 meV in Fig. 4.2) and the thermal transfer of A excitons towards B has not been taken into account in Eq. 2.20. In Chapter 2.4.2 Eq. 2.32 has been derived for the thermal redistribution of charge carriers from a lower (A) to a higher energy level (B). However, in $CuInSe_2$ excitons redistributing from A to B as well as bound excitons can contribute to the B exciton luminescence. Therefore a combination of charge carriers from the lower energy levels (A FE and BE) can redistribute towards the B exciton. Thermal redistribution from multiple energy levels has not been taken into account in Eq. 2.32.
In addition, the AB peak observed between the A and B exciton lines at low temperatures could have an influence on the E_{a1} values. The $M1^{II}$ and $M1^{III}$ lines can also be seen resolved on the low energy side of the A exciton suggesting the possibility of bound excitons redistributing towards the free excitons, as mentioned before. These effects are likely to be the reason for the scatter of the fitted E_{a1} values and the difference of the values measured in the best samples from the exciton binding energy.
An increase of the B exciton intensity above 14 K (~0.07 K^{-1}) which is followed

by a decrease above 32 K (~0.03 K^{-1}) can be seen in Fig. 4.10 (a). This increase could be associated with a thermal transfer of A excitons or/and dissociation of bound excitons towards the B exciton. Fig. 4.10 (b) shows an Arrhenius plot of I_B/I_A, the intensity ratio of the A and B excitons. A significant increase of the B exciton intensity with respect to A above 23 K (~0.04 K^{-1}) can be seen. For temperatures greater than 23 K the B/A ratio corresponds to a Boltzmann factor $exp(\Delta/k_BT)$ with an activation energy of $\Delta = 2.9 \pm 0.1$ meV which is close to the spectral distance between the A and B PL lines. Such an agreement confirms the thermalisation process of A excitons towards B excitons. A similar thermalisation has been reported for GaN (Ref. [71]), where the spectral distance between the A and B free exciton is of the order of 7-8meV [71]. As seen in Fig. 4.10 (b) the thermal transfer of A excitons towards the B exciton takes place at temperatures greater than 23 K, which indicates that the observed increase of the B exciton intensity above 14 K is due to the dissociation of bound excitons towards the B free exciton.

4.3.2.2 Bound Excitons

The Arrhenius plot of the integrated intensity of the B free exciton in comparison with that of the M1 and $M1^I$ components of the M1 bound exciton is shown in Fig. 4.11. Using Eq. 2.20 to describe the experimental points of the M1 and $M1^I$ integrated intensity did not result in a satisfactory fit. A much improved fit is achieved by assuming a dissociation process involving two non-radiative activation channels, as suggested by Bimberg et al. for bound excitons in GaAs, [72] and described by (see also Chapter 2.4.2):

$$I = \frac{I_0}{[1 + a_1 \cdot exp(-E_{a1}/kT) + a_2 \cdot exp(-E_{a2}/kT)]} \tag{4.2}$$

Fitting the experimental points of the integrated intensities of the M1 and $M1^I$ excitons by Eq. 4.2, resulted in the two activation energies E_{a1} and E_{a2}, as presented in Table 4.4 together with the spectral distances between the M1, $M1^I$ and the A, B free excitons. For temperatures below 32 K (~0.03 1/K) activation energies E_{a1} of 7.6 and 6.8 meV have been determined for the M1 and $M1^I$ excitons, respectively. These values are close to those of the spectral distances between the M1 and $M1^I$ and the B free exciton, which suggest that these excitons can be composed of a conduction band electron and a hole from the B valence

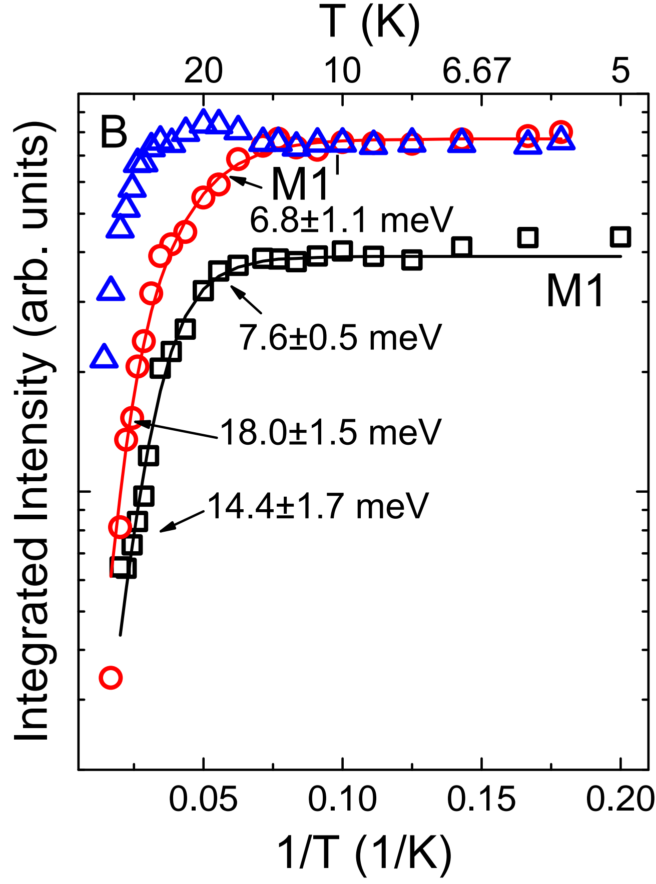

Figure 4.11: Arrhenius plot of the integrated PL intensities of the B free exciton and the bound excitons M1 and M1$^{\mathrm{I}}$, least-square fitted using Eq. 2.21.

sub-band. Such an assignment was proposed earlier in Ref. [35]. Therefore the first decrease of the M1 and M1$^{\mathrm{I}}$ lines intensities can be interpreted as thermal detrapping of these excitons towards the B free exciton. This process also leads to the intensity increase of the B exciton at temperatures above 14 K (∼0.07 1/K) as seen in Fig. 4.11. The second activation energy E_{a2} has been determined as 14.4 and 18.0 meV for the M1 and M1$^{\mathrm{I}}$ excitons, respectively. This second non-radiative activation channel becomes effective at temperatures above 32 K (∼0.03 1/K) where the quenching of the PL intensity of the free B exciton is also effective. The dissociation of the B free exciton into one free electron and one free hole would suggest that E_{a2}=E_{a1}+E_a^B with the dissociation energy [72] of the B free exciton being E_a^B = 18.4±1.6 meV as described earlier in this chapter. The values in Table 4.4 show that the sum $E_{a1} + E_a^B$ is larger than E_{a2} for both the M1 and M1$^{\mathrm{I}}$ exciton. However, this difference could be explained by the fact that Eq. 2.21 does not take into account the interaction between the A and B free excitons. The integrated intensities of the M2 and M3 excitons are plotted

PL line	$\mathbf{E_{A-BE}}$ (meV)	$\mathbf{E_{B-BE}}$ (meV)	$\mathbf{E_{a1}}$ (meV)	$\mathbf{a_1}$	$\mathbf{E_{a2}}$ (meV)	$\mathbf{a_1}$
M1	3.4	6.8	7.6±0.5	8.6	14.4±1.7	175
$M1^I$	2.4	5.8	6.8±1.1	11	18.0±1.5	314

Table 4.4: Spectral distances of the M1 and $M1^I$ bound excitons from the A and B excitons, E_{A-BE} and E_{B-BE}, respectively, the activation energies E_{a1} and E_{a2} obtained from the Arrhenius quenching analysis of the integrated PL intensities, using Eq. 2.21.

against inverse temperature in Fig. 4.12. The M2, $M2^{II}$, $M2^{III}$ and M3 PL lines have nearly disappeared at temperatures about 26 K. At this temperature the free excitons have only just started to quench and thus have a very small influence on the quenching of the M2, $M2^{II}$, $M2^{III}$ and M3 lines. The experimental data in Fig. 4.12 can be well fitted with Eq. 2.20. Table 4.5 gives the spectral distances between the M2, $M2^{II}$, $M2^{III}$ and M3 lines and the A and B free excitons in comparison with the activation energies E_{a1}.

As can be seen in Tables 4.4 and 4.5 the process parameters of the M2, $M2^{II}$, $M2^{III}$ and M3 lines are significantly greater than those of the M1 and free excitons. Since these parameters can provide indications of the nature of defect involved in the formation of bound excitons [104] it becomes apparent that the nature of defect involved in the M1 bound exciton is different from that of the M2 and M3 bound excitons.

The M2 and M3 excitonic lines have previously been associated with the A free exciton [35]. The close comparison between the spectral distances of these lines from the A exciton with the determined activation energies of 6.0±0.6 meV and 6.4±0.4 meV, respectively, agrees with this assignment. In addition, it can be seen from Table 4.5 that the $M2^{II}$ line can also be associated with the A free exciton. However, the activation energy obtained for $M2^{III}$ is closer to the spectral distance of this line from the B exciton rather than from the A exciton, which suggests a different nature of $M2^{III}$ compared to the other excitons belonging to the M2 excitonic complex.

4.3.3 FWHM as a Function of Temperature

The evolution of the FWHMs of the A and B free excitons with temperature increasing from 5.6 to 70 K are shown in Fig. 4.13 (a) and (b), respectively. The FWHM of both excitons increases with increasing temperature due to exciton-phonon scattering. For the A exciton only small changes in the FWHM can

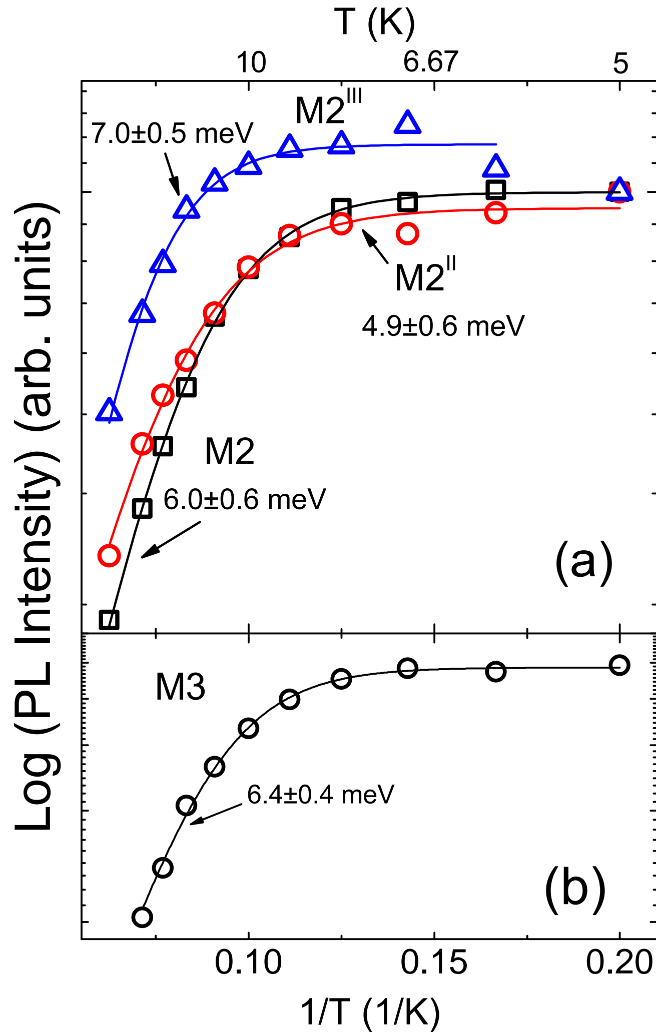

Figure 4.12: Arrhenius plot of the integrated PL intensities of the M2, $M2^{II}$ and $M2^{III}$ (a) and M3 (b) bound excitons, least-square fitted using Eq. 2.20.

be seen in Fig. 4.13 (a) for temperatures up to 20 K. For temperatures higher than 20 K, the FWHM seems to change in steps up to 50 K before drastically increasing for temperatures higher than 60 K. In contrast, the FWHM of the B exciton shows a linear increase up to 45 K in Fig. 4.13 (b).The linear increase of the B FWHM for temperatures up to 45 K suggests that acoustical phonon scattering is dominant [69]. The experimental points in Fig. 4.13 (b) can be described by (first and second term of Eq.2.17 in Chapter 2.4.1):

$$\Gamma(T) = \Gamma_0 + \Gamma_a T \tag{4.3}$$

where Γ_0 is the zero temperature broadening parameter which accounts for exciton-exciton interaction and defect scattering. Γ_a is the coupling strength of the

PL line	$\mathbf{E_{A-BE}}$ (meV)	$\mathbf{E_{B-BE}}$ (meV)	$\mathbf{E_{a1}}$ (meV)	$\mathbf{a_1}$	Valence sub-band
$M2^{III}$	4.7	8.1	7.0±0.5	312	B
$M2^{II}$	5.1	8.4	4.9±0.6	97	A
M2	5.8	9.2	6.0±0.6	202	A
M3	7.5	10.8	6.4±0.4	615	A

Table 4.5: Spectral distances of the M2, $M2^{II}$, $M2^{III}$ and M3 bound excitons from the A and B excitons, E_{A-BE} and E_{B-BE}, respectively, activation energies E_{a1} obtained from the thermal quenching analysis of the integrated PL intensities and the assignment of the valence sub-band for holes involved in the exciton formation.

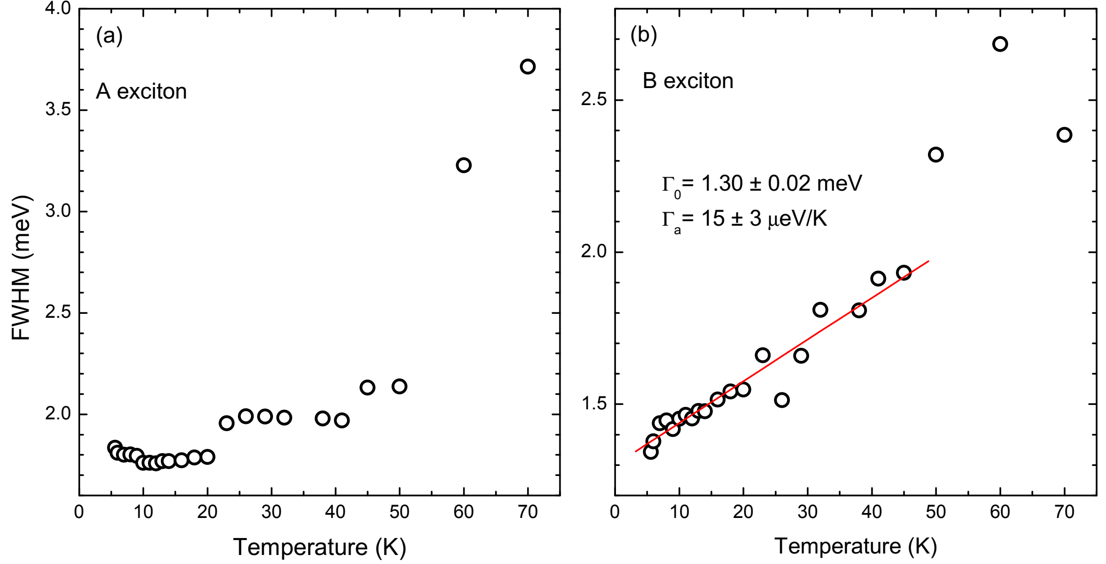

Figure 4.13: Evolution of the FWHM of the A and B free exciton PL lines (a) and (b), respectively, with temperatures increasing from 5.6 to 70 K, fitted with Eq. 2.1

exciton-acoustic-phonon interaction. The linear fit of the experimental points in Fig. 4.13 (b) resulted in a coupling strength of Γ_a= 15± 3 μeV/K and a broadening parameter of Γ_0= 1.30± 0.02 meV for the B free exciton. For the A free exciton this analysis is not possible since its FWHM does not show a linear dependence below 50 K. The bound excitons of the M1 multiplet are energetically very close to the A FE and therefore possibly influence its FWHM.

For temperatures greater than 45 K the influence of optical phonons increases which results in an exponential temperature dependence of the FWHM. For both the A and B free exciton a significant increase can be seen in Fig.4.13 (a) and (b), respectively. However, there are not enough experimental points above 45 K to estimate the optical phonon energy.

4.4 Magneto-Photoluminescence of $CuInSe_2$

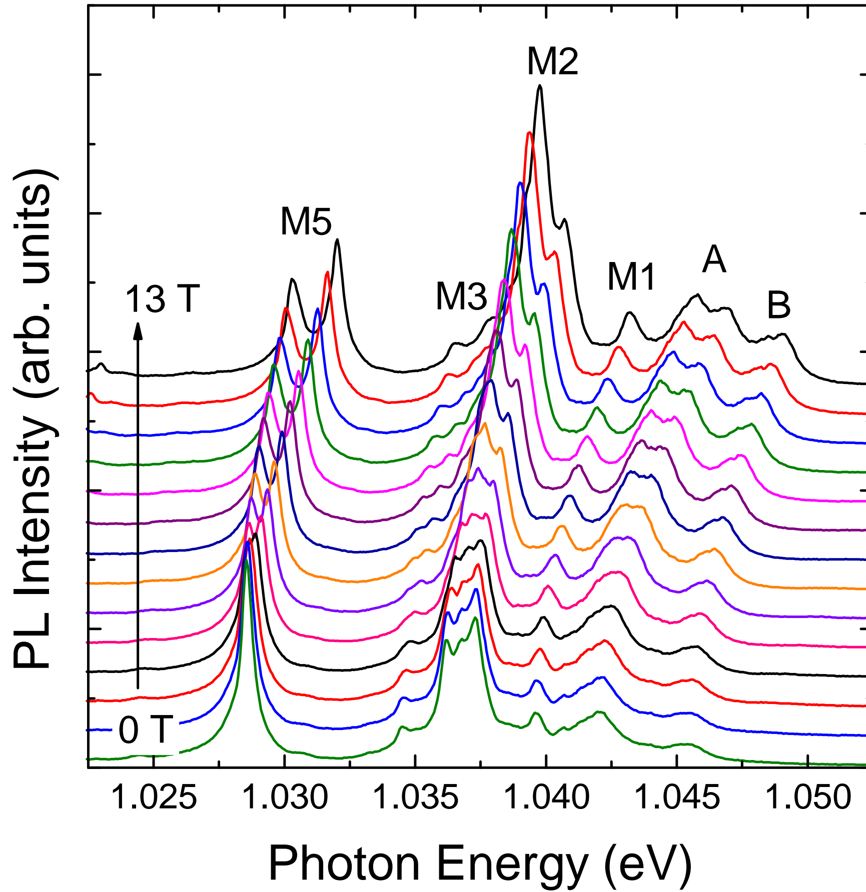

Figure 4.14: Evolution of the $CuInSe_2$ PL spectrum for magnetic fields applied along B$\|z$, increasing from 0 to 13 T.

The evolution of the $CuInSe_2$ spectra under the influence of an applied magnetic field from 0 to 13 T, taken at 4.2 K, is shown in Fig. 4.14. The application of a magnetic field results in a non-linear blue shift of the A and B free excitons and the M1-M5 bound excitons. In addition, it can be seen from Fig. 4.14 that the free and bound excitons exhibit Zeeman splitting (Chapter 2.5.2). The magnetic field has been applied parallel to the three crystal axes x, y and z (x and y are perpendicular to the c-axis whilst z is parallel, see also Fig. 2.1). Fig. 4.15 (a) and (b) shows the PL spectra measured for magnetic fields applied along the x- (B$\perp$z) and z-directions (B$\|$z). The $CuInSe_2$ spectra measured in the perpendicular orientation (B$\|x$ and y) reveal the same diamagnetic shift rate. However, the diamagnetic shift rate measured for the parallel orientation of the magnetic field is larger than the perpendicular one. This effect can be clearly seen in Fig. 4.16, which shows the $CuInSe_2$ PL spectra at 13 T with magnetic

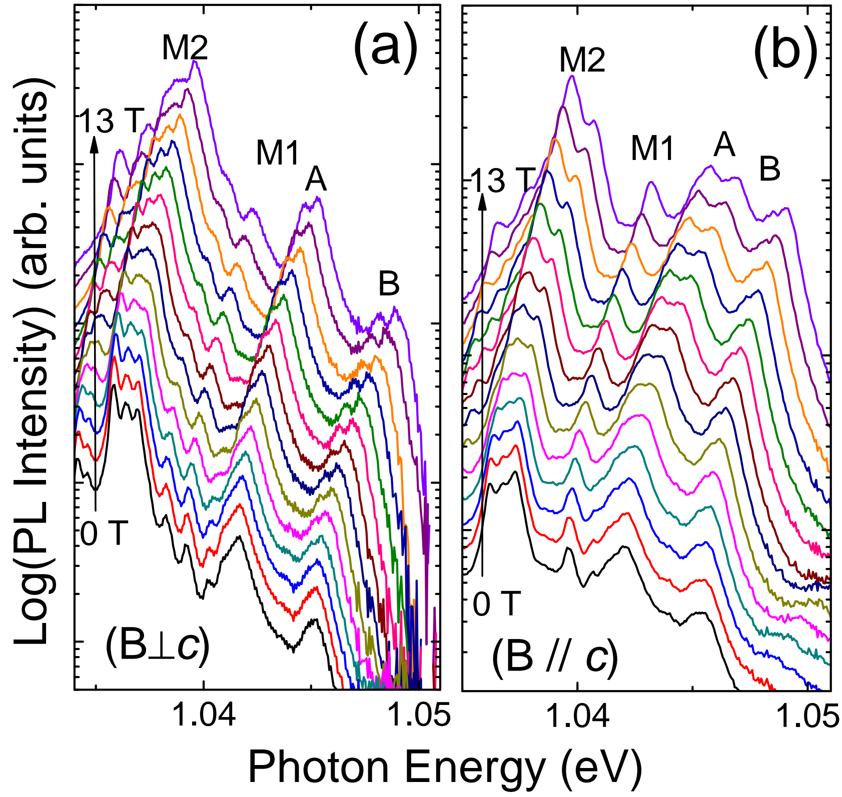

Figure 4.15: Evolution of the PL spectra of the free A, B and M1-M3 bound excitons in $CuInSe_2$ for magnetic field changing from 0 to 13 T, applied perpendicular (B//x) (a) and parallel (B//z) (b) to the c-axis.

field applied parallel to the three crystallographic directions. From this figure it can also be seen that the A exciton splits into two lines for each of the three orientations. The splitting of the A doublet for B⊥z is small, whereas for B∥z the two A exciton lines have undergone a considerably greater splitting and shift from their 0 T positions. In contrast, the difference in diamagnetic shifts for the two orientations is much smaller. The considerable difference in the non-linear shifts of the A exciton for the B⊥z and B∥z orientations indicates a high degree of anisotropy of the A free exciton reduced mass [76].

The weak magnetic field limit can be determined from Eq. 2.33. For $\gamma < 1$ the magnetic field can be treated as a perturbation and Coulomb forces dominate. Using a value of Ry^{*}=8.5 meV [103] and a reduced exciton mass of $\mu=0.08m_0$ the weak field limit can be estimated to be valid up to 7 T. The electron mass is taken as $m_e=0.09m_0$ [105] and that of the hole as $m_h=0.73m_0$ [106].

The dependence of the spectral position on magnetic field applied in directions B⊥z and B∥z can be seen in Fig. 4.17 (a) and (b) respectively. In order to determine the diamagnetic shift and the magnitude of the Zeeman splitting, the

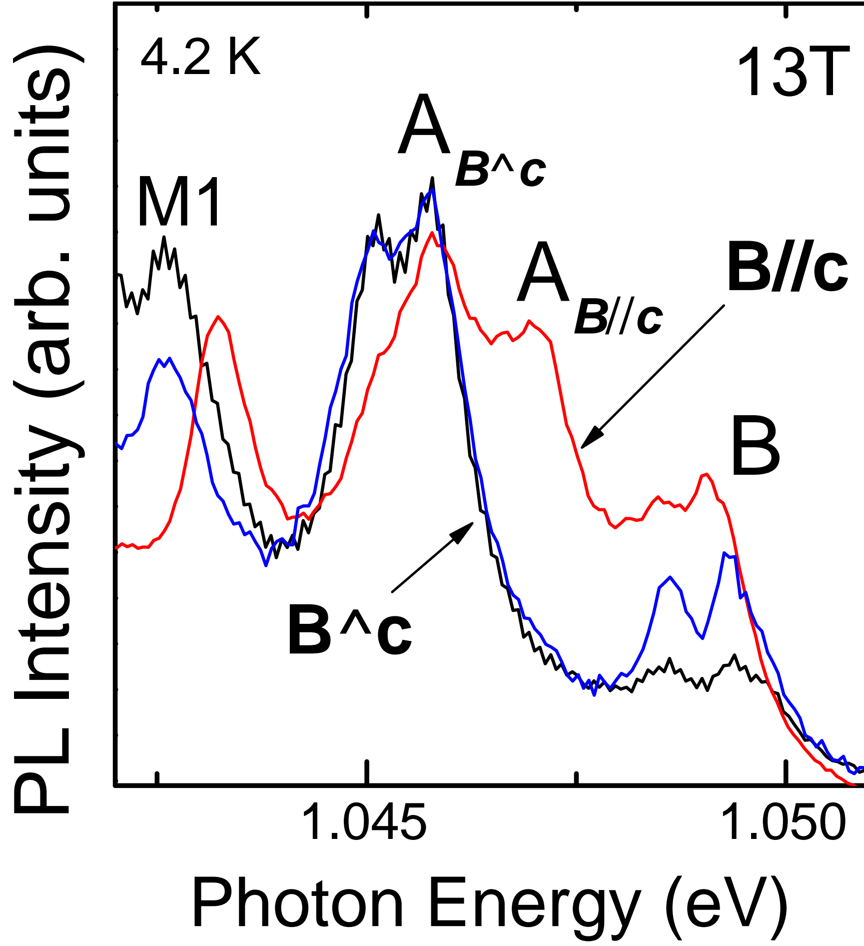

Figure 4.16: Comparison of the PL spectra taken at 13 T for B$\|x$, B$\|y$ (B$\perp$c) and B$\|z$(B$\|$c).

dependencies in Fig. 4.17 have been fitted with Eq. 4.4 (2.37):

$$E_{ex}(B) = E_{ex}(0) \pm \frac{1}{2} g \mu_B B + c_d B^2 \quad (4.4)$$

At magnetic fields greater than 7 T the quadratic function in Fig. 4.17 exceeds the experimental energies indicating that the weak field limit is no longer valid. The values of the perpendicular and parallel components of the anisotropic diamagnetic shift c_d are summarised in Table 4.6. Table 4.6 also includes the

Orientation	A (B⊥z)	A (B‖z)	B (B⊥z)	A (B‖z)
c_d (eV/T^2)x10^{-5}	2.45±0.02	3.19±0.02	2.39±0.01	2.31±0.01
|g|	1.27	1.56	1.23	1.01

Table 4.6: Diamagnetic shift rates c$_d$ and the absolute values of the exciton g-factors |g|, for the A and B free excitons, measured for B⊥z and B‖z.

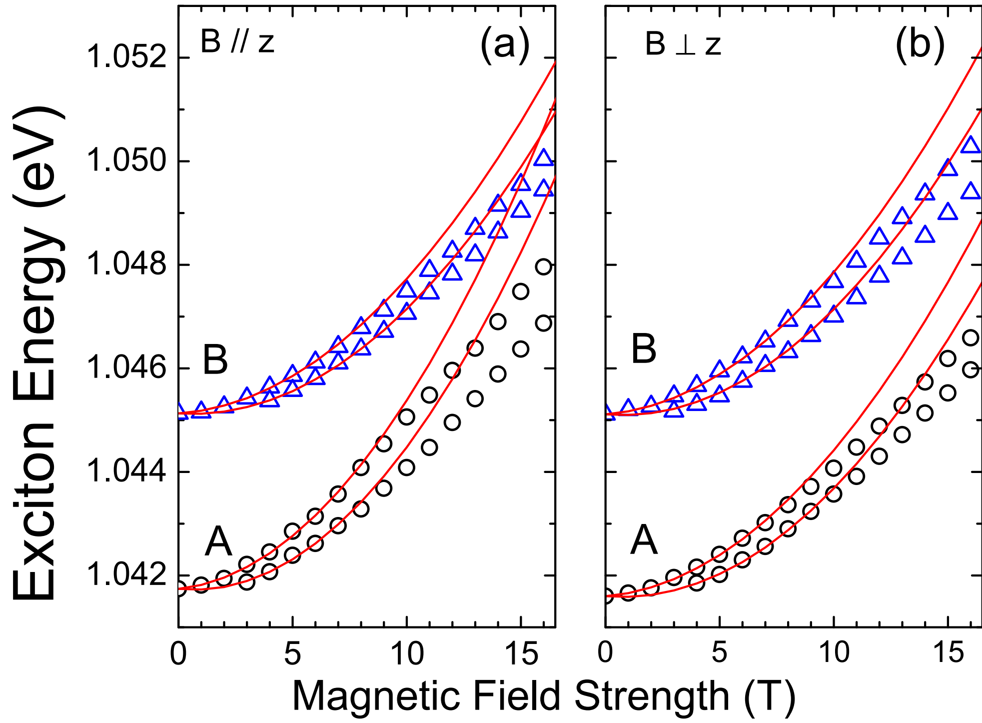

Figure 4.17: Dependence on the magnetic field strength of the A and B exciton spectral position for B||z (a) and B⊥z (b). Symbols are the experimental data points fitted with Eq. 4.4 (solid lines).

perpendicular and parallel components of the excitonic effective g-factor which combines both the electron g_e and hole g_h effective Lande-factors |g|=|$g_e \pm g_h$|. For further analysis of the g-factors a theoretical model is currently being developed by Dr. Anna Rodina of A. E. Ioffe Physico-Technical Institute.

In the case of an uniaxial crystal perturbation theory predicts that the anisotropy of the diamagnetic shift rates is solely determined by that of the excitonic reduced masses $\mu_\perp$ and $\mu_\parallel$ perpendicular and parallel to the z-direction, respectively.

The following section deals with the diamagnetic shift in an uniaxial crystal and is based on the first-order perturbation theory developed by Taguchi et al. [76], who analysed the diamagnetic shift in a biaxial crystal. Their model was further transformed by Dr. Anna Rodina for an uniaxial crystal and allows the determination of the perpendicular and parallel components of the excitonic reduced masses.

4.4.1 Diamagnetic Shift in an Anisotropic Crystal

The diamagnetic shift rates for all three crystal axes are given by:

$$c_{dx} = c_d \frac{\mu^2}{\mu_y \mu_z} \quad (4.5)$$

$$c_{dy} = c_d \frac{\mu^2}{\mu_z \mu_x} \quad (4.6)$$

$$c_{dz} = c_d \frac{\mu^2}{\mu_x \mu_y} \quad (4.7)$$

Where c_{dx}, c_{dy} and c_{dz} are the diamagnetic shift rates in the x, y and z directions of the crystal lattice, respectively. c_d is the isotropic diamagnetic shift rate, μ the average reduced mass and μ_x, μ_y and μ_z are the reduced masses along the three crystal directions. The perpendicular and parallel (to the c-axis) components of the diamagnetic shift can be expressed as:

$$c_{d\perp} = c_d \frac{\mu^2}{\mu_\perp \mu_\parallel} \quad (4.8)$$

$$c_{d\parallel} = c_d \frac{\mu^2}{\mu_\perp^2} \quad (4.9)$$

where $\mu_\perp$ and $\mu_\parallel$ are the perpendicular and parallel components of the reduced masses and c_d equals [76]:

$$c_d = \frac{4\pi^2 \hbar^4 \epsilon^2 \epsilon_0^2}{\mu^3 q^2} \quad (4.10)$$

where ϵ is the dielectric constant. The average reduced mass μ of the exciton is given by:

$$\frac{1}{\mu} = \frac{\epsilon}{3}\left(\frac{2}{\mu_\perp \epsilon_\perp} + \frac{1}{\mu_\parallel \epsilon_\parallel}\right) \quad (4.11)$$

After inserting Eq. 4.10 into 4.9, the parallel diamagnetic shift can be given by:

$$c_{d\parallel} = \frac{\mu_B^2}{2Ry} \frac{\epsilon^2 m_0^3}{\mu} \frac{1}{\mu_\perp^2} \quad (4.12)$$

where μ_B and Ry are given by:

$$\mu_B = \frac{q\hbar}{2m_0} \quad (4.13)$$

$$Ry = \frac{q^4 m_0}{32\pi^2 \epsilon_0^2 \hbar^2} = 13.6eV \quad (4.14)$$

The Rydberg energy Ry^* can then be expressed through:

$$Ry^* = Ry \frac{\mu}{m_0} \frac{1}{\epsilon^2} \tag{4.15}$$

The constants can be summarised in:

$$c_{d0} = \frac{\mu_B^2}{2Ry} = \frac{4\pi^2\hbar^4\epsilon_0^2}{m_0^3 q^2} = 1.232 \cdot 10^{-10} eV/T^2 \tag{4.16}$$

where c_{d0} is the diamagnetic shift rate of the ground state energy level of the electron in a Hydrogen atom. Eq. 4.12 can be written as:

$$c_{d\|} = c_{d0} \frac{\epsilon^2}{\mu} \frac{m_0^3}{\mu_\perp^2} \tag{4.17}$$

Inserting Eq. 4.11 into 4.17 yields:

$$c_{d\|} = c_{d0} \epsilon^2 \frac{m_0^3}{\mu_\perp^2} \frac{\epsilon}{3} \left(\frac{2}{\mu_\perp \epsilon_\perp} + \frac{1}{\mu_\| \epsilon_\|} \right) \tag{4.18}$$

where the static dielectric constant in a uniaxial crystal is given by:

$$\epsilon = \left(\epsilon_\| \epsilon_\perp^2\right)^{1/3} \tag{4.19}$$

The anisotropy of the dielectric constant can be expressed by $\eta = \frac{\epsilon_\perp}{\epsilon_\|}$ and the anisotropy of the reduced masses i.e. the diamagnetic shift rates is given by $x = \frac{\mu_\perp}{\mu_\|} = \frac{c_{d\perp}}{c_{d\|}}$. The literature values of the static dielectric constant reveal a significant scatter from 9.3 [106] to 16 [107]. For the following calculation the theoretical values of $\epsilon_\perp$=11.0 and $\epsilon_\|$=10.3 [46] were used to determine an average value (Eq. 4.19) of ϵ=10.76. Then Eq. 4.20 becomes:

$$c_{d\|} = c_{d0} \epsilon^2 \frac{m_0^3}{\mu_\perp^2} \left(\frac{2 + x\eta}{3\mu_\perp \eta^{1/3}} \right) \tag{4.20}$$

In order to calculate the perpendicular component of the reduced mass this expression can then be rearranged to:

$$\frac{\mu_\perp}{m_0} = \left(c_{d0} \epsilon^2 \frac{2 + x\eta}{3\eta^{1/3} c_{d\|}} \right)^{1/3} \tag{4.21}$$

Eq. 4.21 can be used to calculate the perpendicular component of the reduced mass. After calculating $\mu_\perp$, the parallel component of the reduced mass can now

be obtained by:

$$\frac{\mu_{\parallel}}{m_0} = \frac{1}{x}\frac{\mu_{\perp}}{m_0} \tag{4.22}$$

The reduced masses for the A and B free excitons are summarised in Table 5.7. The significant difference between the $\mu_{\perp}(A)$ and $\mu_{\parallel}(A)$ components for the A ex-

Exciton	$\mu_{p\parallel}/m_0$	$\mu_{p\perp}/m_0$	μ_p/m_0	Ry^* (meV)
A	0.097	0.074	0.081	9.5
B	0.083	0.086	0.084	9.9

Table 4.7: Parallel and perpendicular components of the reduced masses μ of the A and B free excitons.

citon reduced mass demonstrates its anisotropic nature and indicates that $\mu_{\parallel}(A)$ is the heavier component. The anisotropy of the B exciton reduced mass is much smaller and opposite to that of the A exciton, with $\mu_{\parallel}(B)$ being the lighter component. In addition, values of the Rydberg energy Ry^*, using $\mu_p = (\mu_{p\parallel}\mu_{p\perp}^2)^{1/3}$, have been calculated (Eq. 4.15) as 9.5 and 9.9 meV for the A and B free exciton, respectively. These values are in agreement with the binding energies of 8.5 and 8.4 meV determined from the spectral position of the A and B free exciton states, respectively [103].

4.4.2 Effective Hole Masses In $CuInSe_2$

The effective hole masses m_h can be calculated from the excitonic reduced mass and the literature values of the effective electron mass. The conduction band dispersion in $CuInSe_2$ was calculated by Persson [46] using a full-potential linearised augmented plane wave method. In his study, Persson suggested a small anisotropy of the effective electron mass and calculated its parallel and perpendicular components as $m_{e\parallel}$=0.09m_0 and $m_{e\perp}$=0.08m_0. These values and their anisotropy are consistent with experimental data obtained from Shubnikov-de Haas [108] and Hall [109] measurements. The value of m_e=0.09m_0 obtained by Faraday rotation measurements [105] is a bare mass whereas the magneto-PL values include a component of the carrier interaction with phonons. In a semiconductor with partially ionic character additional charge carriers will polarise the lattice. Electrons will attract ions with a positive charge and repel those with a negative charge. For holes, the situation is the other way around. This lattice distortion can be described by a superposition of LO phonons, i.e. a free carrier

is accompanied by a phonon cloud. The simultaneous existence of charge carriers and a phonon cloud is called polaron. The effective mass of a polaron is greater than that of an electron in a rigid lattice [54]

$$m_{e,h\,p} = \left(1 + \frac{\alpha_{e,h}}{6}\right) m_{e,h} \tag{4.23}$$

where $\alpha_{e,h}$ describes the Fröhlich coupling of the carrier to the LO phonon:

$$\alpha_{e,h} = \frac{q^2}{2\hbar\omega_{LO}} \left(\frac{2m_{e,h}\omega_{LO}}{\hbar}\right)^{1/2} \left(\frac{1}{\epsilon_\infty} - \frac{1}{\epsilon}\right) \tag{4.24}$$

Neglecting any possible anisotropy of the Fröhlich constant gives α_e=0.202 and α_h=0.524, assuming a longitudinal optical (LO) phonon energy of 29 meV [94] and theoretical anisotropic components of the high-frequency dielectric constant $\epsilon_{\infty\perp}$=8.2 and $\epsilon_{\infty\parallel}$=7.8 [46]. Taking the polaron concept into account yields $m_{ep\parallel}$=0.101m_0 and $m_{ep\perp}$=0.090m_0 for the parallel and perpendicular components of the effective electron mass. These values were then used to determine the values of the effective hole masses of the A and B free exciton which are given in Table 4.8. The bare value of the A-hole mass m_A^*=0.713m_0 is in good agreement

$\mathbf{m_h/m_0}$	$\mathbf{m_{A\parallel}}$	$\mathbf{m_{A\perp}}$	$\mathbf{m_A^*}$	$\mathbf{m_{B\parallel}}$	$\mathbf{m_{B\perp}}$	$\mathbf{m_B^*}$
m_p	2.479	0.434	0.775	0.461	1.796	1.141
bare	2.279	0.399	0.713	0.424	1.651	1.049

Table 4.8: Polaron and bare effective masses of the A- and B-band holes as well as the average hole masses for these bands (m_A^* and m_B^*) .

with 0.73m_0 [106] and a separate effective hole mass for the A exciton 0.71m_0 estimated by Neumann et al. [110]. In contrast the B hole masses are greater than the 0.092m_0 estimated by the same approach.

The anisotropy of the A valence band of $m_{A\parallel}/m_{A\perp}$=5.7 is in agreement with the theoretically predicted value of 4.7 [46]. The B valence band anisotropy is inverted and smaller than that of the A exciton. However, its value $m_{B\perp}/m_{B\parallel}$=3.9 is double the theoretical prediction of 2.1. Recently reported diamagnetic shift rates for the A exciton $c_d(A)$= 2.7x10^{-5}eV/T^2 and B exciton $c_d(B)$= 2.4x10^{-5}eV/T^2, measured in a non-oriented $CuInSe_2$ single crystal (Ref [111]), are in good agreement with the values shown in Table 4.6.

4.5 Summary

A study of the excitation power and temperature dependence of the PL of free and bound excitons in high quality $CuInSe_2$ has been performed. In addition, magneto-PL experiments of the A and B FE have been studied.
Excitation power and temperature dependent PL measurements identify the A and B PL lines as free exciton recombination involving holes from the A and B valence sub-bands, respectively. In addition, it is shown that M1 excitons are bound to shallow defects with a high concentration whereas most of the M2 (except $M2^{IV}$) and M3 multiplet excitons appear to be bound to more complex defects with low concentrations. The properties of $M2^{IV}$ resemble those of the M1 excitons suggesting that $M2^{IV}$ could be an additional excitonic component of the M1 multiplet.
The temperature dependence of the spectral positions of the A and B FE in PL show an anomalous behaviour which is backed-up by RF measurements. Possible explanations for this behaviour were presented. An average optical phonon energy of 26±3 meV was determined from the analysis of the temperature dependence of the A FE spectral position for temperatures larger than 70 K. In order to fully describe the RF spectra a theoretical model will be developed in future work.
The temperature quenching analysis of the A and B PL lines in the highest quality crystal leads to activation energies of 12.5 meV and 18.4 meV for the A and B free exciton, respectively. However, the temperature quenching analysis of lower quality samples resulted in smaller activation energies with minimum values of 6 and 7 meV for the A and B free exciton, respectively. In addition, a thermal redistribution of A excitons towards the B exciton at temperature above 23 K due to their small energy separation was revealed.
Thermal activation energies for the M1, M2 and M3 bound excitons have also been determined and the assignment of the holes involved in the exciton formation was suggested. It appears that the M1 excitons are composed of a conduction band electron and a B valence band hole. In contrast for the $M2^{II}$, M2 and M3 excitons the A valence band hole is involved in their formation. For $M2^{III}$ the assignment of the hole was not conclusive. The exciton corresponding to this line might be different from the others belonging to the M2 excitonic multiplet.
The analysis of the temperature dependence of the FWHM of the B FE revealed that for temperatures below 45 K acoustical phonon scattering is dominant. The resulting coupling strength was determined as 15±3 μeV/K.

The diamagnetic shifts of the A and B free exciton lines in the PL spectra of $CuInSe_2$ single crystals reveal a considerable difference for the magnetic fields applied perpendicular and parallel to the z-direction of the chalcopyrite lattice. The exciton reduced masses are calculated within the low field approximation using a first order perturbation model for non-degenerate independent excitons. The A free exciton reduced mass demonstrates a strongly anisotropic nature whereas the anisotropy of the B free exciton reduced mass is weaker and inverted with respect to the orientation. Effective hole masses of $m_{A\|} = 2.279m_0$ and $m_{A\perp} = 0.399m_0$ for the A, as well as $m_{B\|} = 0.424m_0$, $m_{B\perp} = 1.651m_0$ for the B valence sub-bands are estimated assuming literature effective electron masses.

Chapter 5

$CuInS_2$

$CuInS_2$ is a ternary chalcopyrite semiconductor with a direct band gap of 1.55 eV. It has a high potential for the application as an absorber layer in thin-film solar cells. This chapter presents the results of the PL study of different $CuInS_2$ single crystals and is divided into three parts. The first part deals with the excitation power dependence of the PL lines whereas the second part present the results of temperature dependent PL measurements. The last part discusses the results of PL measurements as a function of an applied magnetic field. The different PL measurements provide an insight into the fundamental material properties of $CuInS_2$. The spectra presented in this chapter have been measured at Strathclyde and the GHMFL using the set-ups described in Chapter 3.
The examined $CuInS_2$ single crystals were grown by the THM (see Section 3.1.2). The typical elemental composition of the crystals, determined by energy dispersive X-ray analysis (EDX), is Cu: 24, In: 26 and S: 50 at. %. The EDX measurements were performed in the group of Dr. Alexander Mudryi at the Scientific-Practical Material Research Centre of the National Academy of Science of Belarus.

5.1 Excitons in $CuInS_2$

The near band gap regions of the $CuInS_2$ RF and PL spectra, taken at 4.2 K, are shown in Fig. 5.1 (a) and (b), respectively. The RF spectrum contains a prominent resonance at about 1.536 eV which has been assigned to the ground state of the free exciton associated with the A valence sub-band [33, 112, 113]. The high-resolution PL spectrum of a high quality $CuInS_2$ single crystal, shown in Fig. 5.1 (b) reveals a number of sharp peaks which are assigned to the radiative

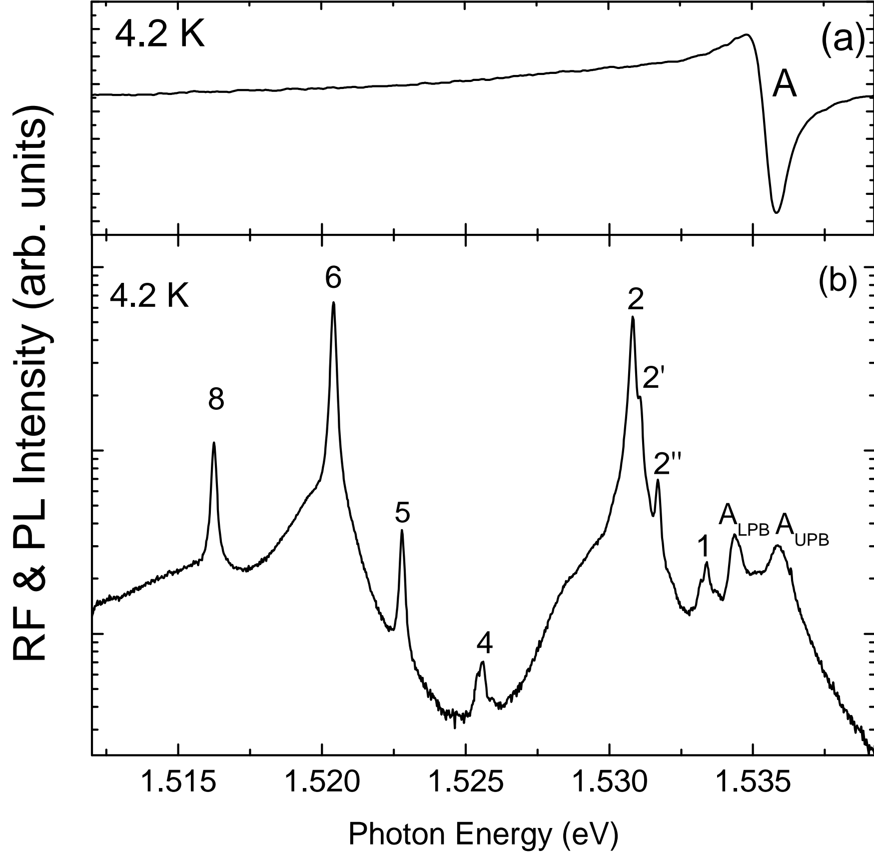

Figure 5.1: Near band gap RF (a) and PL (b) spectra of $CuInS_2$ single crystals taken at 4.2 K.

recombination of free and bound excitons following earlier reports [26, 33]. Their energy positions along with those reported by Yakushev et al. [33], Yoshino et al. [114] and Binsma et al. [26] are shown in Table 5.1. The free exciton emission exhibits a well resolved doublet structure A_{LPB} and A_{UPB}, shown in Fig. 5.1 (b). These peaks at 1.534 and 1.536 eV were assigned earlier [33, 79, 115] as the lower (LPB) and upper polariton branch (UPB) of the A exciton polariton, respectively.

Polaritons are the result of the strong coupling of free excitons with photons of the same energy in direct semiconductors with dipole-active excitons. This coupling results in a mixed-mode excitation called an exciton-polariton with a two-branch dispersion curve in k-space (see also Chapter 2.6). The exciton-photon coupling may be characterised by the longitudinal-transverse splitting Δ_A^{LT} of the A exciton ground state which corresponds to the spectral separation between the UPB and LPB. Based on the experimentally observed longitudinal-transverse splitting, the contribution of the A exciton to the polarisability $4\pi\beta_A$ of $CuInS_2$

PL line	this work	Yakushev et al. [33]	Yoshino et al. [114]	Binsma et al. [26]	Exciton
A_{UPB}	1.5359	1.5361			FE
A_{LPB}	1.5344	1.5348			FE
A	1.5362		1.5355	1.535	FE
1	1.5334	1.5336			BE
2	1.5308	1.5309	1.5298	1.53	BE
3		1.5289	1.5288		BE
4	1.5256	1.5255	1.524	1.525	BE
5	1.5228	1.5228			BE
6	1.5204	1.5203	1.5225	1.52	BE
7		1.5186	1.5173	1.5185	BE
8	1.5162	1.5162		1.5165	BE
9		1.5138		1.513	BE

Table 5.1: Peak position of the free and bound exciton lines and their assignment to free (FE) and bound excitons (BE) in $CuInS_2$.

can be estimated using [78]:

$$\Delta_A^{LT} = E_T^A \left(\sqrt{1 + \frac{4\pi\beta_A}{\epsilon}} - 1 \right) \approx E_T^A \frac{4\pi\beta_A}{2\epsilon} \tag{5.1}$$

using the Taylor expansion:

$$\sqrt{1+x} \approx 1 + \frac{1}{2}x \tag{5.2}$$

where E_T^A is the energy position of the lower polariton branch of the A exciton-polariton. The observed splitting Δ_{LT}^A between the LPB and UPB is 1.5 meV and the dielectric constant was reported as ϵ=10.2 [26, 112] which leads to a polarisability $4\pi\beta_A$ of 0.020±0.003. The same value has been determined by Mudryi et al. [79] from the polariton splitting whereas Shay et al. [47] determined the polarisability as 0.01 and 0.02 for the A and BC free excitons, respectively, from the fit of the resonances in the $CuInS_2$ reflectivity spectrum. For the related chalcopyrite compounds $AgGaSe_2$ and $CuGaS_2$ similar values for the polarisability have been determined as 0.015 [116] and 0.01 [36], respectively. The larger value of the polarisability determined from the polariton splitting could be an indication for a slightly larger exciton-photon coupling in $CuInS_2$ due to a more polar nature of the bonds.

Figure 5.2 shows the comparison between the PL spectra of different $CuInS_2$ single crystals. The three spectra have been normalised to peak BE 2. As can be seen in Fig. 5.2 different crystals exhibit different A exciton features. Fig. 5.2 (a) shows only a single peak for the A exciton whereas Figs. 5.2 (b) and (c) reveal

the doublet structures due to polaritons. The slit width was not the same in each case and the resulting spectral resolution corresponds to 0.2, 0.17 and 0.14 meV for spectra 5.2 (a), (b) and (c), respectively (see Table 3.2 in Chapter 3).

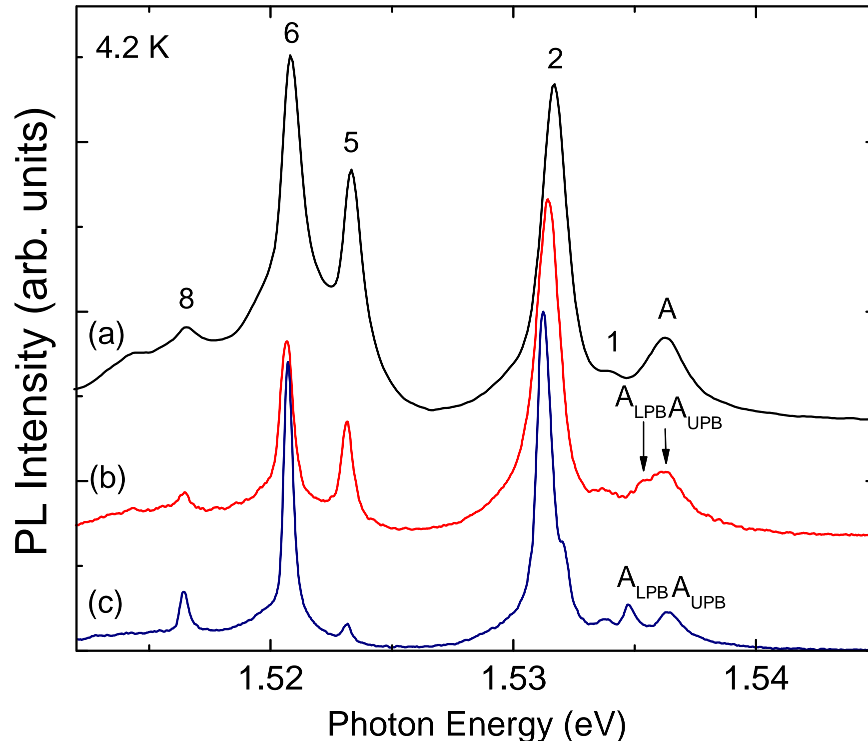

Figure 5.2: Near band gap PL [(a)-(c)] spectra of different $CuInS_2$ single crystals taken at 4.2 K The spectral resolutions of the spectra are 0.2, 0.17 and 0.14 meV, respectively. The spectra are normalised to line 2.

Defect scattering (see Chapter 2.6) provides a possible explanation why in Fig. 5.2 (a) only a single A FE peak can be observed whereas Fig. 5.2 (c) reveals a clear doublet line shape for the A exciton-polariton. From the relative intensities of the bound and free exciton lines in Fig. 5.2 (a) to (c), it can be deduced that the concentration of defects differs for the different $CuInS_2$ crystals. In particular, the intensities of the BE peak 2 relative to the A single or double peak increases from Fig. 5.2 (a) to (c), indicating a higher concentration of defects in Fig. 5.2 (c), where the exciton-polariton structure is resolved. Steiner el al. [82] (Section 2.6) suggested a scattering mechanism resulting from elastic neutral donor scattering in GaAs to be responsible for a doublet line shape of the exciton-polariton luminescence for samples with large donor concentrations. It can also be seen, that the intensity of the BE 5 peak decreases relative to the single or double A peak from Fig. 5.2 (a) to (c). The FWHM of the BE 2 line decreases from 1.3

meV in spectrum 5.2 (a) to 0.6 meV in spectrum 5.2 (c), indicating an increase in crystal quality. Thus, the presence of certain defects as well as a high crystal quality leads to a polaritonic doublet peak in the PL spectrum.

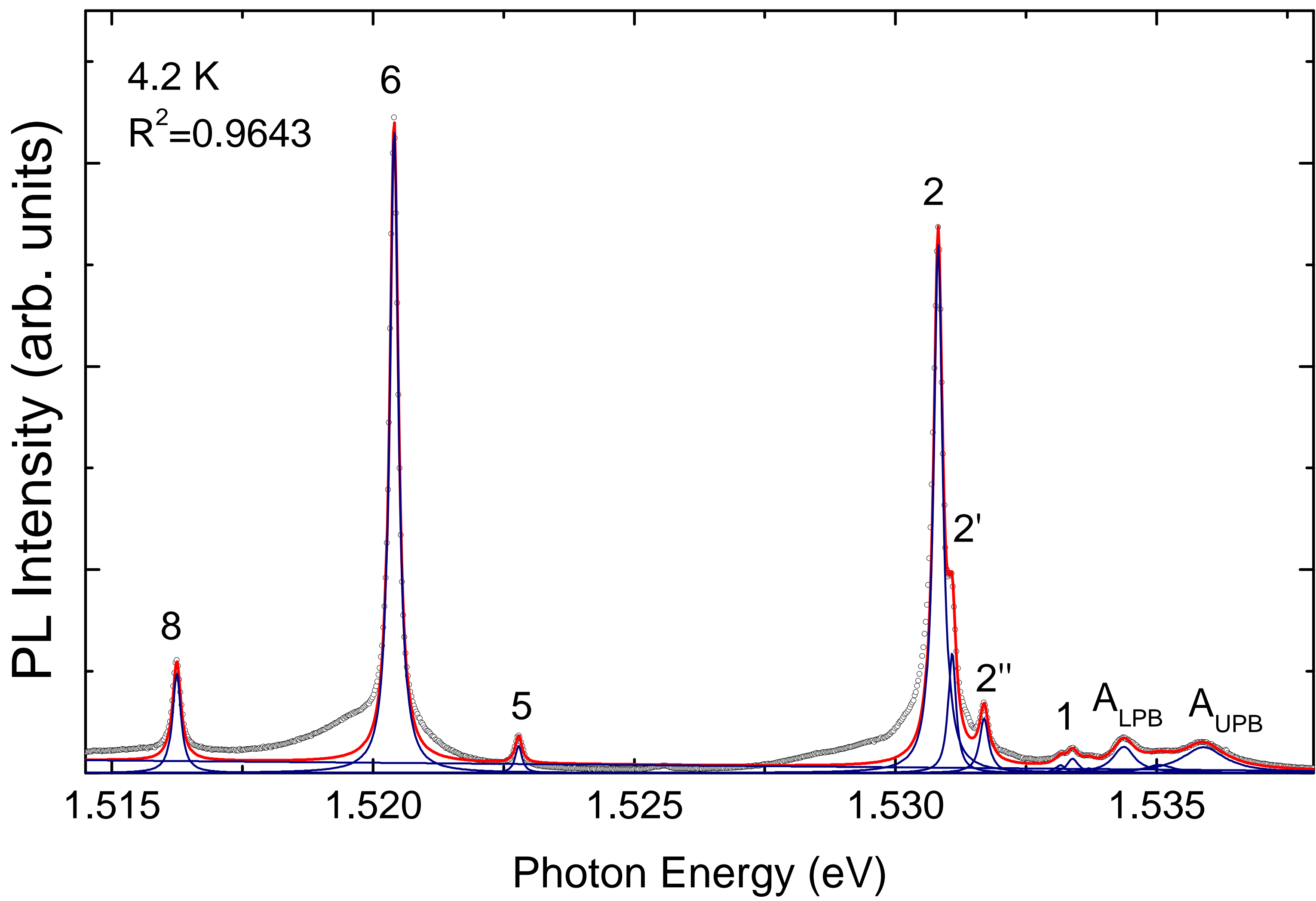

Figure 5.3: PL spectrum of high quality $CuInS_2$ fitted with Lorentzian curves (circles - experimental data, blue - individual Lorentzian and red - fit line) taken at 4.2 K.

For the detailed analysis of the $CuInS_2$ PL lines each spectrum has been fitted with Lorentzian curves as shown in Fig. 5.3 and 5.4. Lorentzian curves have been found to describe the excitonic line shapes very well. This indicates low exciton-phonon coupling in $CuInS_2$ and a low concentration of crystal imperfections and impurities [67] (see Chapter 2.4.1).

Figs. 5.3 and 5.4 show that at low temperatures both the BE lines 2 and 1 exhibit 3 components. Lines such as 1^{I}, 1^{II}, 2^{I} and 2^{II} have not yet been reported for $CuInS_2$. In addition, a non-resolved PL line, labelled as A_F in Fig. 5.4, appears at about 1.535 eV between the two polariton branches. This feature could be an additional free exciton component associated with a forbidden transition in the A exciton-polariton dispersion.

The spectral position and FWHM of all lines included in the fit in Fig. 5.3 and 5.4 are show in Table 5.2. The FWHM for the UPB and LPB is 0.5 and 1.0 meV, respectively, whereas the FWHM ranges between 0.18 and 0.3 meV for the BE lines. The small values of the FWHM of the BE lines suggest their excitonic nature. In order to confirm this assignment and study the fundamental properties of the excitons in $CuInS_2$ the PL spectra were measured as a function of excitation power and temperature.

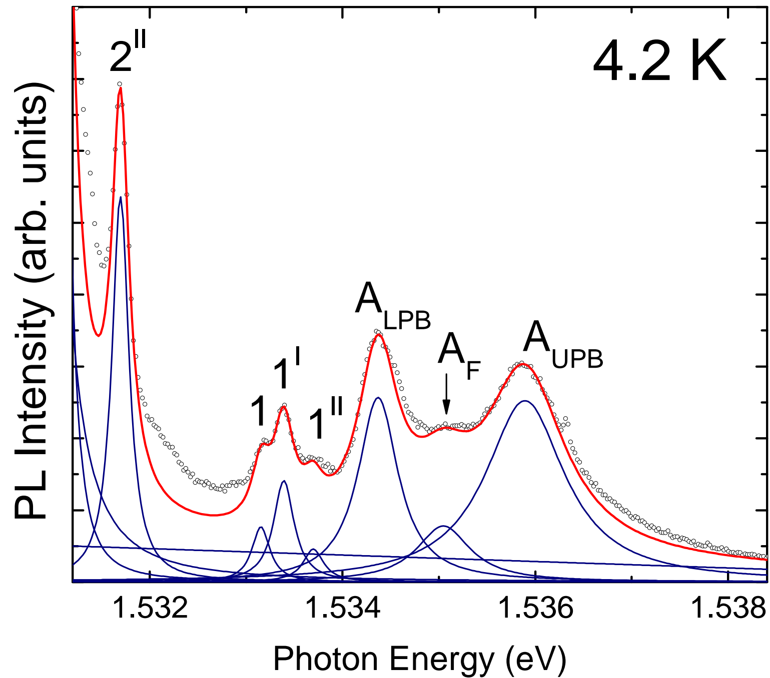

Figure 5.4: The polariton region of the high quality $CuInS_2$ PL spectrum fitted with Lorentzian curves (circles - experimental data, blue - individual Lorentzian and red - fit line) taken at 4.2 K.

PL line	Energy (eV)	FWHM (meV)
A_{UPB}	1.5359	1.0
A_F	1.5351	0.7
A_{LPB}	1.5344	0.5
1^{II}	1.5337	0.3
1^{I}	1.5334	0.3
1	1.5332	0.2
2^{II}	1.5317	0.2
2^{I}	1.5311	0.18
2	1.5308	0.2
5	1.5228	0.2
6	1.5204	0.2
8	1.5162	0.2

Table 5.2: Spectral Position and FWHM of the PL lines, obtained by the fit in Fig. 5.3 with Lorentzian line shapes.

5.2 Excitation Power Dependence

Excitation power dependent PL measurements were performed at 4.2 K for excitation powers ranging from 10 to 160 mW (laser output), corresponding to power densities from 22 to 340 W/cm^2 on the sample. Fig. 5.5 shows the evolution of the $CuInS_2$ spectra (spectrum (c) in Fig. 5.2) with increasing excitation power. The spectral positions of the excitonic PL lines do not change with increasing excitation power. A slight increase of about 10% of the FWHM above 40 mW is observed. This increase in the FWHM might be due to a slight increase in sample temperature at higher excitation powers. Each PL spectrum, shown in Fig. 5.5, has been least-square fitted with Lorentzian curves as shown in Fig. 5.3.

5.2.1 Emission Intensity as a Function of Excitation Power

The dependence of the integrated intensity I on the excitation power P of the A exciton-polariton branches UPB and LPB has been obtained from the fit of each individual PL spectrum with Lorentzian curves and is shown in Fig. 5.6. The dependence of the PL intensity on the excitation power follows the power law $I \sim P^k$. As mentioned in Section 2.4.3, for excitonic transitions a power coefficient k between *1* and *2* is expected [74]. For both the UPB and LPB a power coefficient $1<k<2$ has been obtained, suggesting their excitonic nature.
The determined power coefficients as well as the spectral positions of the A

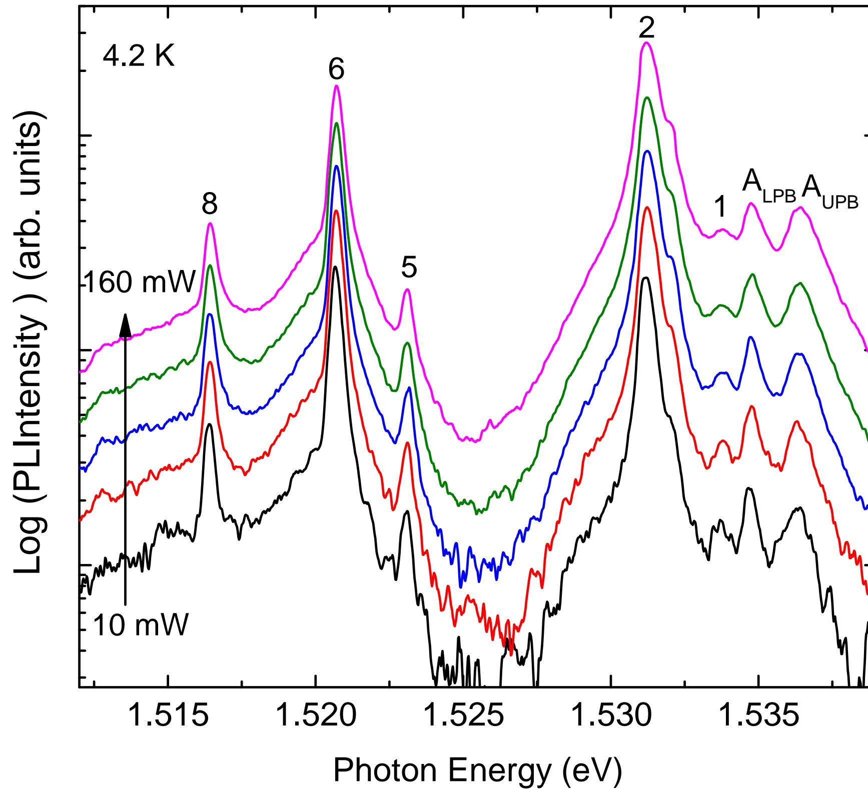

Figure 5.5: Evolution of the $CuInS_2$ PL spectrum (spectrum (c) in Fig 5.2) with excitation powers increasing from 10 to 160 mW, taken at 4.2 K.

PL line	Energy (eV)	k
A_{UPB}	1.5364	1.23
A_{LPB}	1.5348	1.10

Table 5.3: Spectral positions and k coefficients of the A exciton-polariton branches A_{UPB} and A_{LPB}.

exciton-polariton branches UPB and LPB are summarised in Table 5.3. The power coefficient for the UPB is slightly larger than that of the LPB, which could be due to an increase in the population of the UPB with increasing excitation power, as it has been suggested for polariton emission in AlN [117]. According to Ref. [117] the UPB is sensitive to both temperature and excitation power due to its low density of states. Therefore, the filling of the UPB increases with increasing temperature and/or excitation power. A thermal redistribution of charge carriers from LPB will be discussed in Section 5.3.2. Figure 5.7 shows the excitation power dependence of the integrated intensity of the bound excitons in $CuInS_2$. As seen in Fig. 5.7 for excitation powers higher than 40 mW a decrease in the slope occurs for the bound excitons under study. This change might be

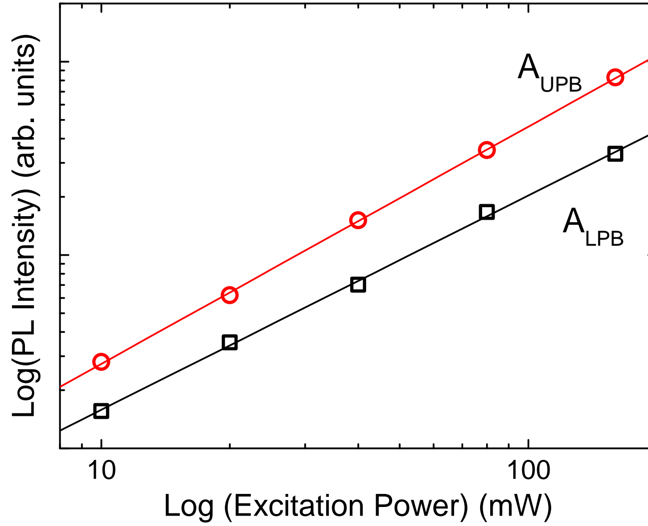

Figure 5.6: Log-Log plot of the integrated intensity versus the excitation power for the A exciton-polariton branches A_{UPB} and A_{LPB}, fitted linearly (open symbols - data, solid line - linear fit.

due to an increase in sample temperature with increasing excitation power which affects the bound excitons more strongly than the A free exciton. The increase of the FWHM by about 10 % for the bound excitons backs up this suggestion. For excitation powers below 40 mW, $1 < k_1 < 2$ has been determined for the bound excitons 1, 2 and 5 confirming their excitonic nature. For the bound excitons 6 and 8 the linear fit of the log (I)-log (P) plot yields power coefficients smaller than unity which, according to Ref. [74] can be a characteristic of free-to-bound and/or DAP transitions. However, the values of the FWHMs of both lines are very small at 4.2 K. Binsma et al. [26] assigned line 6 to a donor level valence band transition. However, the width of the reported line was ranging between 2 and 12 meV, which is one order of magnitude larger than that observed here for line 6 . The power coefficient for excitation powers below 40 mW (k_1) and above 40 mW (k_2) as well as the spectral positions for the bound excitons are summarised in Table 5.4.

Weber et al. [95] reported a similar behaviour, namely $k < 1$ and changes in the slope of the line in the logarithmic plot, for excitons bound to isoelectronic defects in silicon. This suggests that lines 6 and 8 may originate from excitons bound to isoelectronic defects. Krustok el al. [97] reported emission of excitons bound to defects acting as isoelectronic traps in $CuInS_2$, which were closely situated DAP acting as neutral defects. Thus the change of the slope at higher excitation powers could be due to a rise in sample temperature and/or by the saturation of the

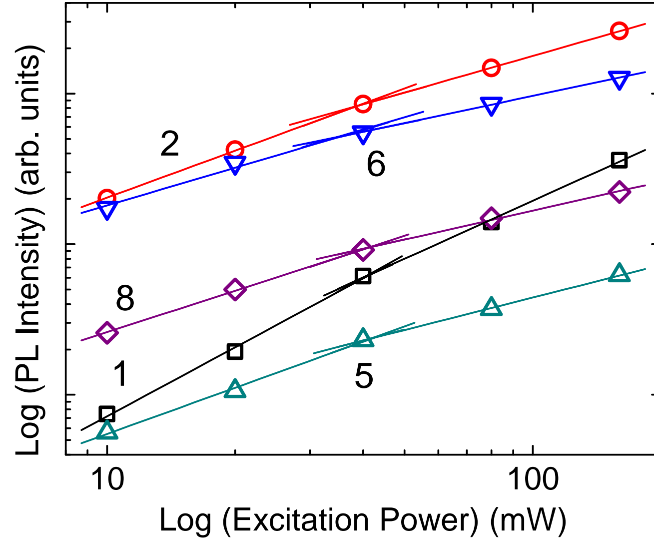

Figure 5.7: Log-Log plot of the integrated intensity versus the excitation power for the bound excitons in $CuInS_2$, fitted linearly (open symbols - data, solid line - linear fit.

defects involved in the formation of the BE. Excitons bound to complex defects with a low concentration have also been found in $CuInSe_2$ as reported earlier in Chapter 4.2 and Ref. [90].

PL line	Energy (eV)	k_1	k_2
1	1.5337	1.52	1.3
2	1.5312	1.02	0.8
5	1.5231	1.02	0.7
6	1.5207	0.83	0.6
8	1.5164	0.91	0.6

Table 5.4: Spectral positions and k_1 and k_2 (where k_1 corresponds to excitation powers below 40 mW and k_2 to excitation powers above 40 mW) coefficients of the bound excitons in $CuInS_2$.

5.3 $CuInS_2$ Temperature Dependence

The temperature evolution of the PL spectra has been studied for a number of $CuInS_2$ single crystals. Fig. 5.8 shows the evolution of the near band-edge PL spectra with a single peak for the A free exciton (spectrum (a) in Fig.5.2), for temperatures from 4.2 to 110 K. The different bound exciton lines are seen to quench at different rates. Fig. 5.8 shows that at about 32 K the bound exciton

lines 5, 6 and 8 have nearly disappeared. In contrast the bound exciton line 2 and the A free exciton lines are still visible up to 80 K. The rapid thermal quenching of the 5, 6 and 8 lines confirms their assignment to the radiative recombination of bound excitons [26, 33, 114]. For temperatures larger than 80 K the exciton line 2 has nearly disappeared whereas the A FE is still visible up to 110 K. The evolution of the near band-edge PL spectrum, containing the A exciton-polariton structure (Fig. 5.2 (c)), with increasing temperature from 4.2 to 90 K can be seen in Fig. 5.9. The 5, 6 and 8 PL lines quench at a faster rate than line 2 and the exciton-polariton peaks. At about 50 K the PL lines 5, 6 and 8 have nearly completely disappeared whereas the PL line 2 can be still clearly seen at 70 K and the exciton-polariton structure at 90 K. Although, the exciton-polariton structure is still visible at 90 K, the LPB and UPB peaks broaden and merge together with increasing temperature. In addition, it seems that the rate of the intensity decrease of LPB is much faster than that of the UPB which would suggest a redistribution of exciton-polariton from the LPB to the UPB which was suggested earlier in Section 5.2.1.
The spectra in Figs. 5.8 and 5.9 were recorded with different slit widths which correspond to spectral resolutions of 0.2 and 0.14 meV, respectively. The BE lines 5, 6 and 8 have nearly disappeared at 32 K in Fig. 5.8, whereas they are visible up to 50 K in Fig. 5.9. In contrast, the FE lines are visible up to 110 and 90 K in Figs. 5.8 and 5.9, respectively. The different quenching rates of the BE in the two sample reflects on their difference in quality. In Fig. 5.9 three components of line 2 are visible indicating a higher quality of this sample.

5.3.1 Spectral Position of the A Free Exciton as a Function of Temperature

The evolution of the spectral position of the A FE (spectrum (a) in Fig. 5.2) under increasing temperatures from 4.2 to 110 K is shown in Fig. 5.10. For temperatures up to 20 K the spectral position of the A FE does not change significantly. The A FE exhibits a blueshift of ∼2.2 meV above 20 K with a maximum in the spectral position of the A FE line at about 100 K. For temperatures higher than 100 K, the blueshift of the A FE line stopped. An increase of ∼2 meV of the band gap energy with temperatures up to about 100 K has also been reported for PL measurements by Binsma et al. [26] and for photoreflectance measurements by Shirakata et al. [115].This anomalous behaviour of the band gap was also observed

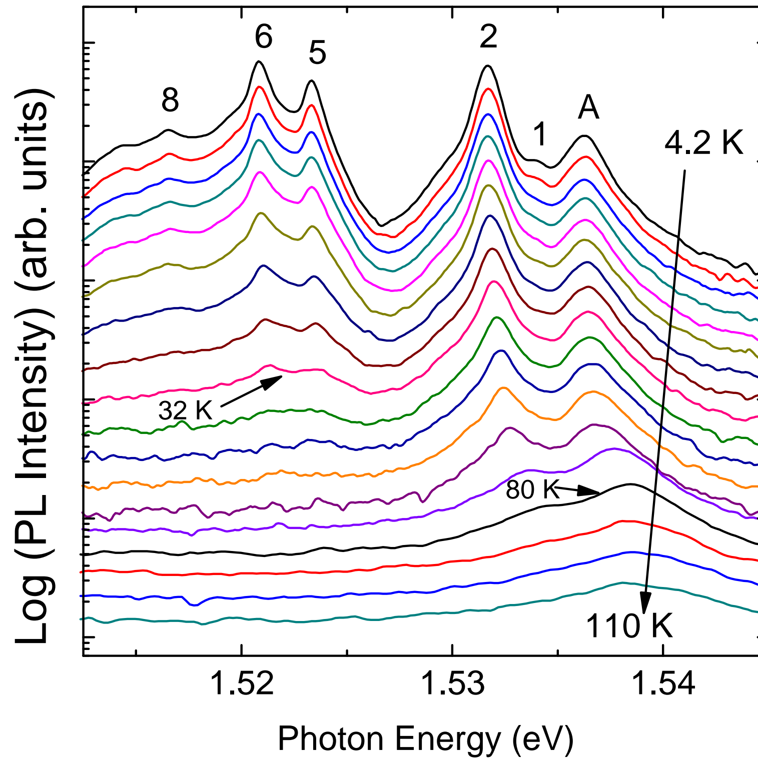

Figure 5.8: Evolution of the $CuInS_2$ PL spectrum ((a) in Fig5.2) with a single peak for the A free exciton with temperature increasing from 4.2 to 110 K. The resolution was changed from 0.2 to 0.3 meV at 60 K.

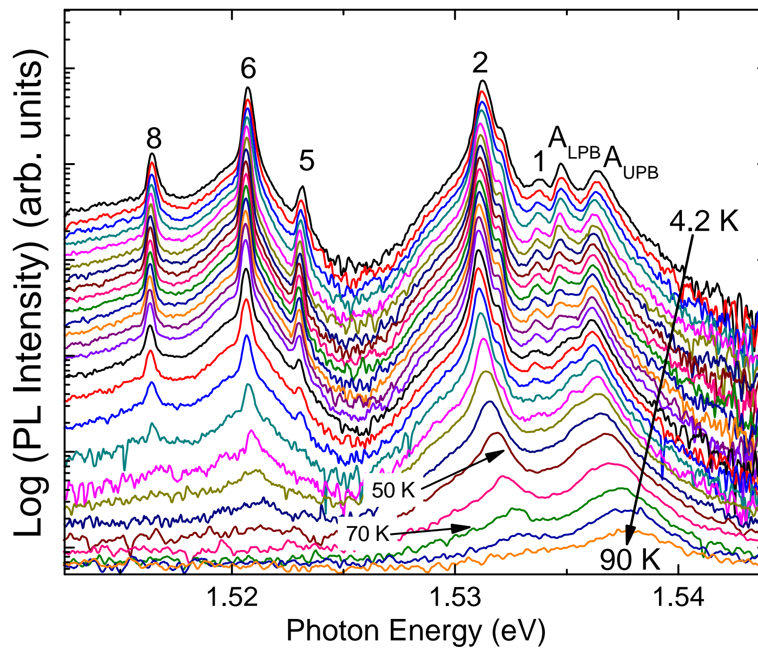

Figure 5.9: Evolution of the $CuInS_2$ PL spectrum ((c) in Fig. 5.2) with doublet peak associated with the exciton-polariton of the A FE with temperatures increasing from 4.2 K to 90 K. The resolution changes at 40 K from 0.14 to 0.3 meV due to an increase in slit width.

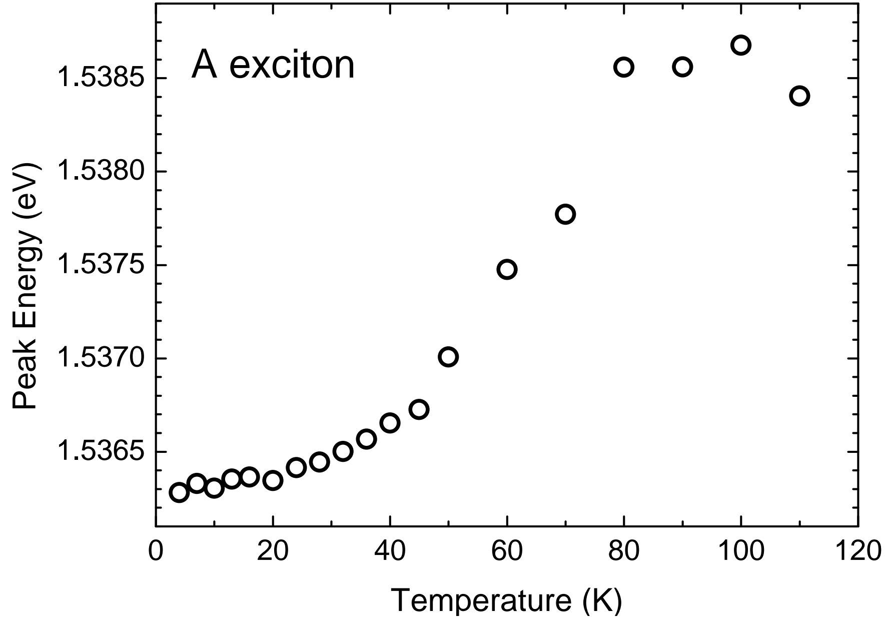

Figure 5.10: Temperature dependence of the spectral position of the A free exciton (spectrum (a) in Fig. 5.2).

for $CuInSe_2$ in Chapter 4.3, for $AgGaS_2$ [118] and $AgInSe_2$ [48]. Generally, no increase of the band gap energy is expected with increasing sample temperature. O'Donnell et al. observed a decrease of the band gap energy for GaAs, GaP, Si and C due to electron-phonon interactions [98].
In Fig. 5.11 the evolution of the $CuInS_2$ RF spectrum with temperature increasing from 4.2 to 100 K is shown. It can be seen in this figure that the resonance of the A exciton exhibits a temperature dependent shift of its spectral position and broadening. As mentioned in Section 4.3.1 a theoretical model is needed to fully describe the RF resonances. In contrast to the resonances of the A and B FE in $CuInSe_2$, the resonance of the A FE changes its line shape making the analysis of its minimum in dependence of the temperature unreliable. However, it can be seen from Fig. 5.11 that the temperature dependence of the spectral position of the RF minimum seems to red shift and then blue shift with increasing temperature as will be discussed for the LPB and UPB of the A FE in the following paragraph.
The evolution of the spectral positions of the LPB and UPB PL lines, measured for sample (c) in Fig. 5.2, with temperatures increasing from 4.5 to 50 K, taken with excitation powers of 40 and 100 mW, are shown in Fig. 5.12 (a) to (d). For low excitation powers (40 mW) the spectral position of the LPB and UPB exhibit a redshift of ~ 0.1 meV and ~ 0.3 meV, respectively, up to 16 K which is then

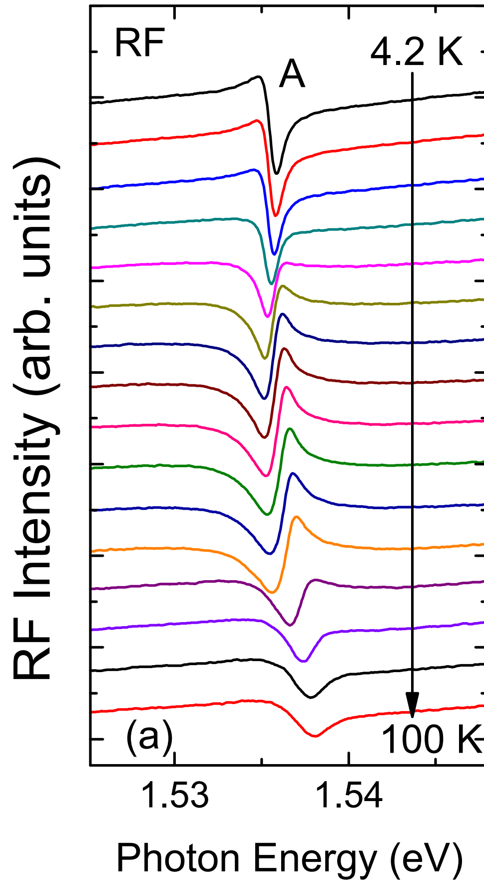

Figure 5.11: Evolution of the $CuInS_2$ RF spectrum with temperature increasing from 4.2 to 100 K.

followed by a blueshift. In contrast, for higher excitation powers (100 mW) the redshift is only $\sim$ 0.1 meV for the UPB whereas no redshift can be seen for the LPB. For temperatures greater than 20 K a blueshift of about $\sim$ 0.8 meV can be observed for both PL lines. The redshift of the excitonic spectral positions has not yet been reported.

The temperature dependent behaviour of the FE and exciton-polariton lines reflect the temperature dependence of the $CuInS_2$ band gap. The temperature shift of the band gap arises from the effects of electron-phonon interaction and also thermal lattice expansion. In addition, random alloy disorder and composition fluctuations, creating inhomogeneous potential fluctuations, can cause lower energy tail states which are common for ternary alloys. These tail states can be responsible for the red-blue-shift of the band gap energy and have been observed in, for example, ternary III-Nitride alloys such as InGaN [101] or AlGaN [102]. For temperatures below 16 K and low excitation powers, the charge carriers can relax into the lowest potential minima which leads to a decrease in the band gap

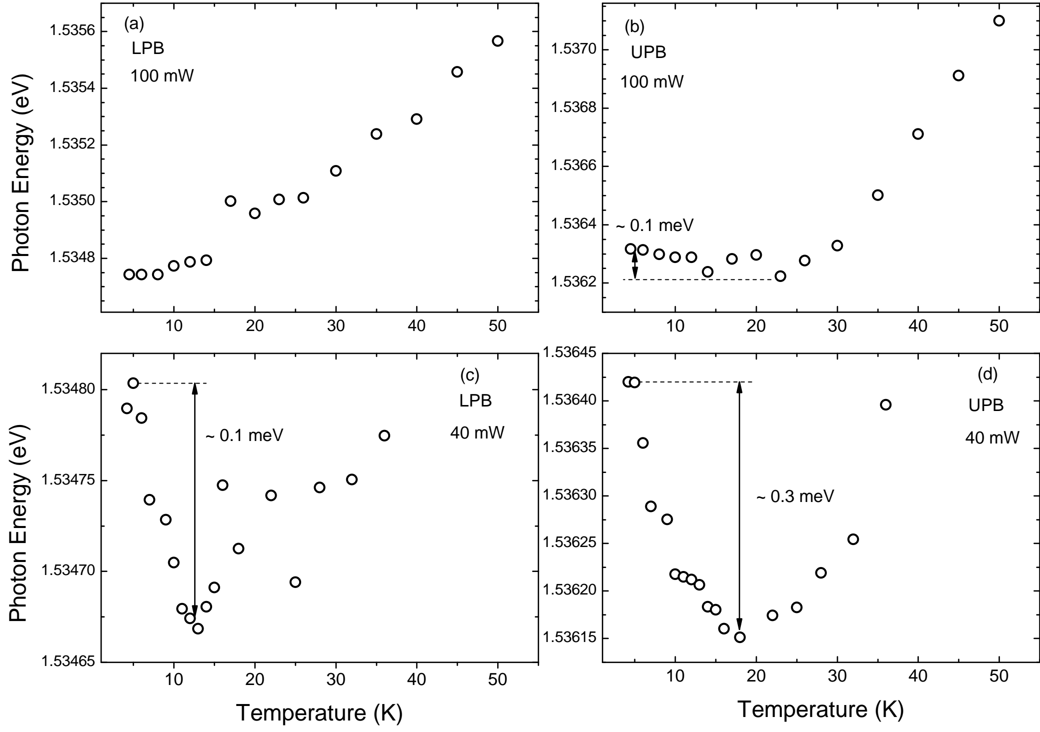

Figure 5.12: Temperature dependence of the spectral position of the LPB and UPB at 100 mW (a) and (b) and at 40 mW (c) and (d), respectively, of the A exciton-polariton ((c) in Fig. 5.2).

energy. The charge carriers do not have enough thermal energy to overcome the potential barriers and are trapped in the local minima. For temperatures above 16 K the charge carriers gain enough thermal energy and can overcome the potential barriers [102]. In addition, other nonradiative processes become dominant which cause the charge carriers to recombine before they can reach the low energy tails [101]. Since the redshift is of ~ 0.3 and ~ 0.1 meV for low and high excitation powers, respectively, it can be concluded that the influence of the potential fluctuations in $CuInS_2$ is very small in comparison to that in InGaN/GaN quantum wells, where the redshift can be tens of meV [101].

Another possible explanation for the blueshift is given by Nagaoka et al. [100]. They measure the thermal expansion of the lattice with temperature increasing from 10 to 300 K. Below 100 K a negative thermal expansion of the lattice has been observed for $CuInS_2$ single crystals. The decrease in thermal expansion leads to an increase in bond strength which causes the band gap to increase. Negative expansion coefficients were also reported by Deus et al. [99] for $CuInSe_2$ and for $AgGaSe_2$ [119].

In addition, it was reported by Shay et al. [47] that the behaviour of the band gap

is influenced by the p-d hybridization. The band gap of the I-III-VI_2 chalcopyrites is lowered with respect to the corresponding II-IV compounds (see Chapter 2.1.2) due to the hybridization of the copper d-levels with the chalcogen p-levels. As mentioned in Chapter 4.3 an increase of the band gap can occur with increasing temperature due to the decrease in p-d hybridization.
The two expansion effects are of opposite character. If the lattice expansion decreases the distance between the atoms decreases which would results in an increase of the p-d hybridization. Thus, it can be concluded either the negative thermal expansion or the decrease in p-d hybridization due to a positive lattice expansion dominates.

5.3.2 Temperature Quenching of the Exciton PL Intensity

This section presents the dependence of the integrated intensity of the A FE, exciton-polariton and the BE (line 2 to 8) on the temperature. The study of the temperature dependenc of excitonic luminescence can provide information on the underlying recombination processes (see Chapter 2.4.2).

5.3.2.1 A Free Exciton

Fig. 5.13 plots the integrated intensity of the A FE versus inverse sample temperature. The temperature dependent quenching of the PL peak is due to the thermally activated level depopulation and/or to the activation of non-radiative recombination centres [71]. An Arrhenius plot can be used to determine the activation energy E_{a1} of the process involved. Using Eq. 2.20 (Chapter 2.4.2) to fit the temperature quenching of the A FE line for $CuInS_2$ yields an activation energy and process parameter of E_{a1}=14±2 meV and a_1=21±6, respectively.
Previously, Binsma et al. [26] reported a value of 20 meV as activation energy for the A FE which is slightly larger than the determined value of 14 meV. However, the activation energy E_{a1} is expected to be similar to the binding energy which was determined as 18.5 meV by Yakushev et al. [112] from the analysis of the free exciton excited states in $CuInS_2$.

5.3.2.2 A exciton-polariton

The temperature dependent quenching of the UPB line (low temperature spectrum shown in Fig. 5.2 (b)) can be seen in Fig. 5.14. In contrast to the A FE line, an increase of the intensity above 12 K can be observed, suggesting a thermal

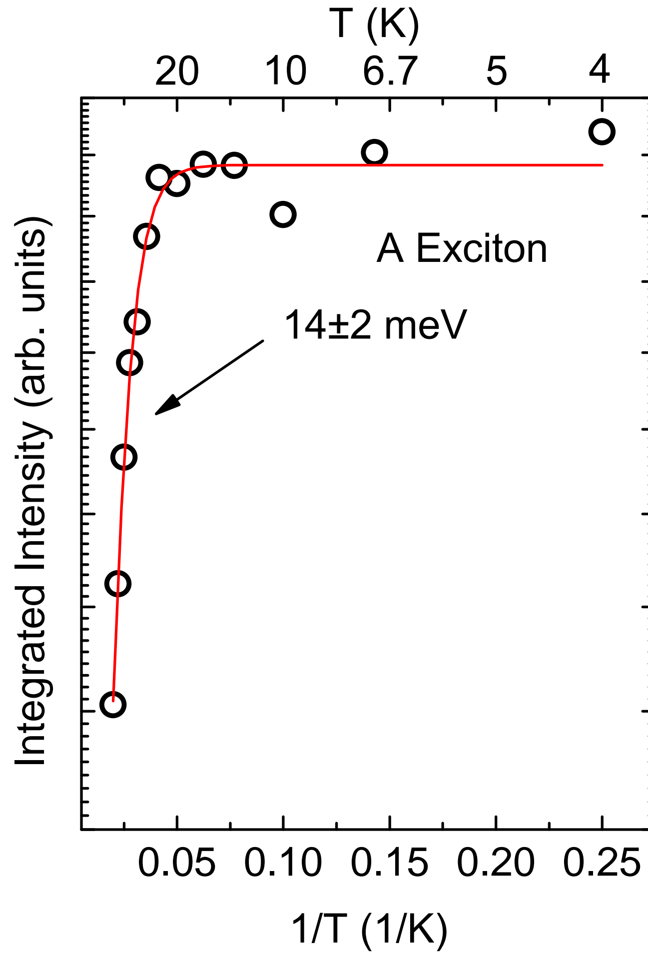

Figure 5.13: Arrhenius plot of the integrated intensity of the A free exciton fitted using Eq. 2.20.

transfer of exciton-polaritons or bound excitons towards the UPB. The increase is then followed by a decrease of the intensity at about 30 K. Assuming that LPB exciton-polaritons as well as bound excitons thermally redistribute towards the UPB, based on a 2 level model, Eq. 2.32 (Chapter 2.4.2) has been used to fit the experimental points of the UPB. The fit yields a value of 5±2 meV for Γ, the activation energy needed to transfer charge carriers from level 1 to 2, above 12 K. Above 30 K, the PL integrated intensity decreases and an activation energy of 15±2 meV has been obtained for E_{a1}.
The first activation energy Γ of 5 meV is very similar to the energy separation of the BE 2 and the UPB. In addition, the spectral distance between the LPB and UPB for the spectrum in Fig. 5.2(b) is ∼1 meV. Therefore, it is suggested that the intensity increase of the UPB above 12 K is due to the thermal transfer of excitons from BE 2 towards the UPB of the A exciton. Due to the small spectral distance between the LPB and UPB, a thermal transfer of excitons from the LPB

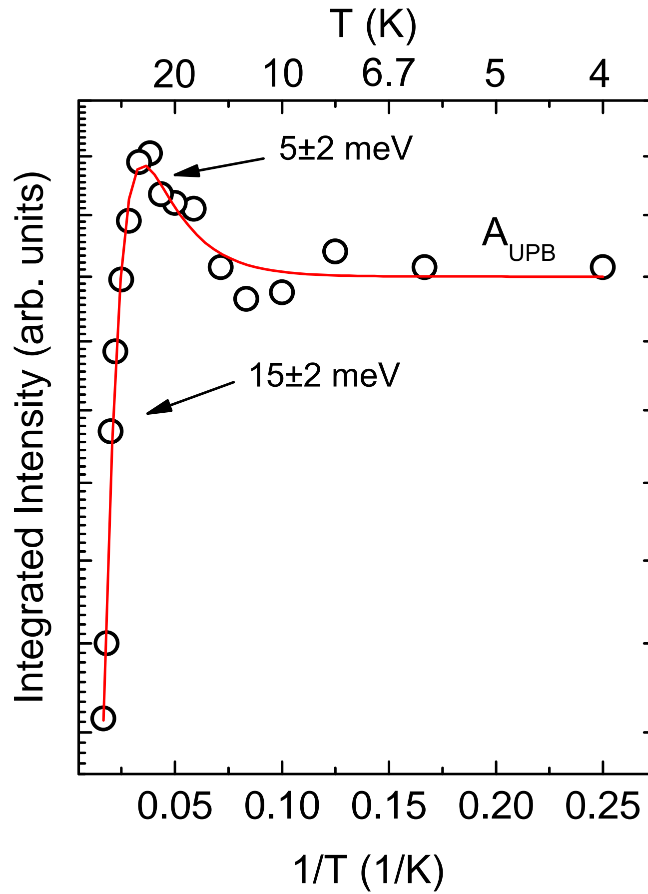

Figure 5.14: Arrhenius plot of the integrated intensity of the UPB fitted with Eq. 2.32 (from the temperature evolution of the spectrum (b) in Fig. 5.2).

to the UPB is also likely. The second activation energy E_{a1} determined as 15±2 meV for temperatures greater than 30 K is close to the value of the binding energy reported by Yakushev et al. [112] and similar to the activation energy of the A FE found earlier. The LPB in spectrum (b) in Fig. 5.2 is not well resolved. With increasing temperature the LPB broadened and merged with the UPB. Therefore a determination of an activation energy was not possible.

The two polariton branches are well resolved in spectrum (c) in Fig. 5.2. The temperature dependence of their integrated intensities are plotted in Fig. 5.15 (a). The integrated intensity of the LPB starts to quench at about 9 K, whereas that of the UPB increases, suggesting the thermal transfer of excitons from the LPB towards the UPB of the A exciton-polariton. The experimental points of the LPB have been fitted using Eq. 2.20 and an activation energy of 2.5±0.6 meV was obtained. This value is close to the spectral distance of 1.6 meV between the LPB and UPB of the A exciton-polariton. The integrated intensity of the UPB was measured up to 50 K which was not sufficient to observe any thermal

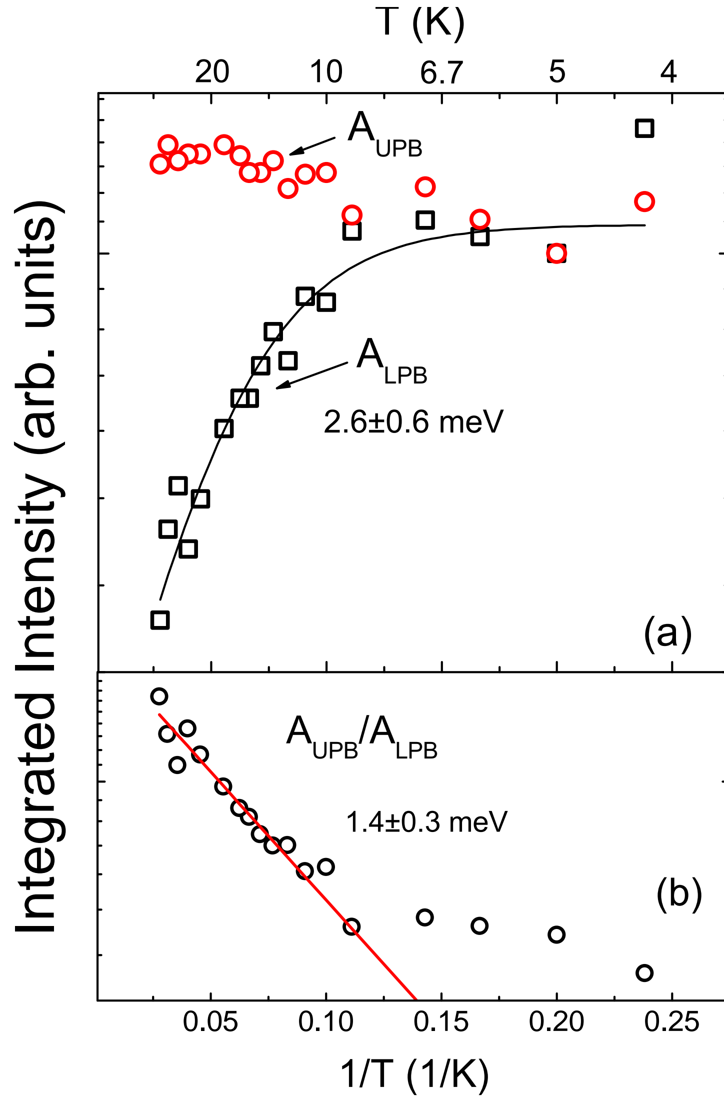

Figure 5.15: Arrhenius plot of the integrated intensity of the UPB and LPB (spectrum (c) in Fig. 5.2) of the A free exciton (a) and the ratio of the integrated intensities of the UPB and LPB (b).

quenching of the UPB and hence no activation energy could be determined.
Fig. 5.15 (b) shows an Arrhenius plot of I_{UPB}/I_{LPB}, the intensity ratio of the UPB and LPB. A significant increase of the UPB with respect to the LPB above 9 K can be seen. For temperatures greater than 9 K the UPB/LPB ratio corresponds to a Boltzmann factor $exp(\Delta/k_BT)$ with an activation energy of Δ=1.4±0.3 meV which matches the spectral distance of 1.6 meV between the LPB and UPB of the A exciton-polariton. Such an agreement confirms the thermalisation process of the LPB excitons towards the UPB as indicated by the excitation power dependence of these lines in Section 5.2 and observed for the A and B free exciton in $CuInSe_2$ (see Chapter 4) as well as in GaN [71].

5.3.2.3 Bound Excitons

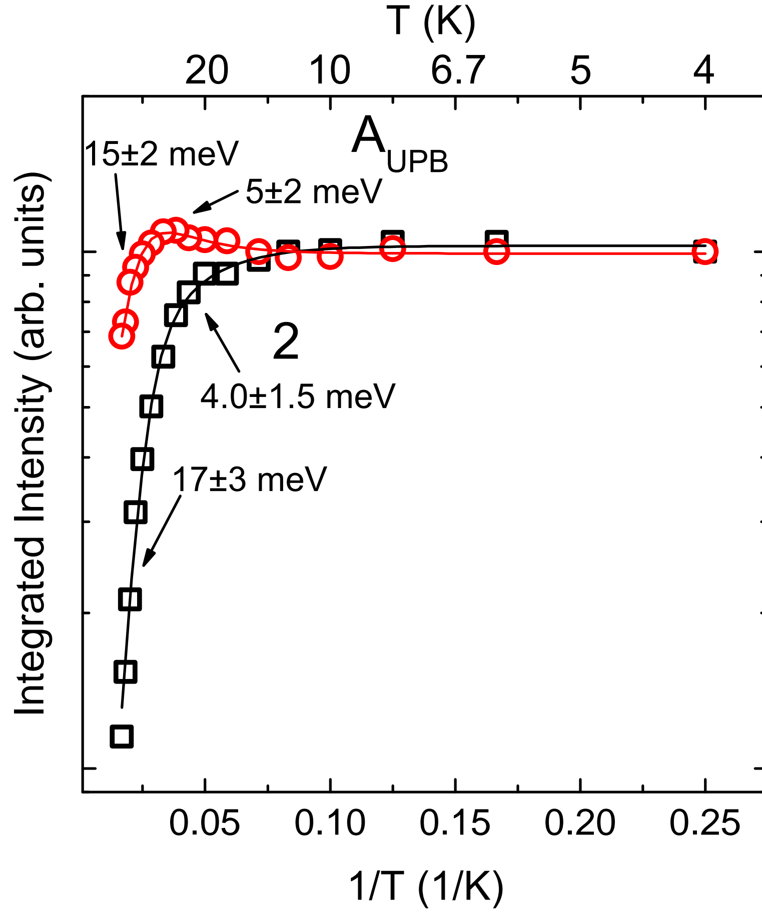

Figure 5.16: Arrhenius plot of the integrated PL intensity of the bound exciton 2 and A_{UPB} (spectrum (b) in Fig. 5.2) fitted using Eqs. 2.21 and 2.32, respectively.

The Arrhenius plot of the UPB of the A exciton in comparison with that of the bound exciton 2 (from low temperature spectrum (b) in Fig. 5.2) is shown in Fig. 5.16. In order to obtain a satisfactory fit, the experimental points of the bound exciton 2 have been fitted with Eq. 2.21 which assumes a dissociation process involving two non-radiative activation channels [72]. Fitting the experimental points of the BE 2 using Eq. 2.21 results in the two activation energies E_{a1} and E_{a2} which are summarised in Table 5.5 together with the process parameters a_1 and a_2 as well as the spectral distances between BE 2 and the UPB and LPB of the A exciton-polariton and the A FE. The values of the activation energies and process parameters are the averages across the spectra (a) to (c) in Fig. 5.2. For temperatures below 30 K an activation energy of E_{a1} of 4.0 meV has been determined. This value lies in between the spectral separation of the BE 2 and UPB and LPB of the A exciton-polariton and is similar to that of the BE 2 and

the A FE. Therefore the first decrease of the BE 2 PL intensity can be associated with thermal detrapping of this exciton towards the A exciton. This process can also lead to the UPB intensity increase above 12 K as shown in Fig. 5.16. The second activation energy has been determined as E_{a2}=17 meV for the BE 2. This second non-radiative activation channel becomes effective at temperatures above 30 K where the quenching of the UPB of the A exciton-polariton is also effective. The dissociation of the UPB into a free electron and a free hole would assume that $E_{a2} = E_{a1} + E_a^{UPB}$ [72] with E_a^{UPB} being the dissociation energy of the UPB. E_a^{UPB} has been found as 15±2 meV from the fit of the UPB. From Table 5.5, it can be seen that E_{a2} is close to the sum of the first activation energy and the dissociation energy of the UPB.

PL line	$E_A - E_{BE}$ (meV)	$E_{UPB} - E_{BE}$ (meV)	$E_{LPB} - E_{BE}$ (meV)	E_{a1} (meV)	E_{a2} (meV)	a_1	a_2
2	4.6	5.2	3.6	4.0 ± 1.5	17 ± 3	3	277

Table 5.5: Spectral distances of the BE 2 from the A FE and the UPB and LPB of the A exciton-polariton, $E_A - E_{BE2}$, $E_{UPB} - E_{BE2}$, $E_{LPB} - E_{BE2}$, respectively, and the activation energies E_{a1} and E_{a2} and process parameters $a_1$and a_2 of the bound exciton line 2 in $CuInS_2$. The values of the activation energies E_{a1} and E_{a2} were averaged across the spectra (a) to (c) in Fig. 5.2.

The integrated intensities of the bound excitons 5, 6 and 8 are plotted against inverse temperature in Fig. 5.17. The bound excitons 5, 6 and 8 have nearly disappeared at about 36 K. At this temperature the UPB of the A exciton-polariton has only just started to quench and thus has a very small influence on the quenching of the bound exciton lines 5, 6 and 8. The experimental data in Fig. 5.17 can be well fitted, assuming only a single channel, with Eq. 2.20 and the resulting activation energies, which were averaged across spectra (a) to (c) in Fig. 5.2, are summarised in Table 5.6. Wakita et al. [120] estimated activation energies of the BE 5 and 6 from the thermal quenching analysis of their corresponding PL lines as 11 and 16 meV, respectively. The reported activation energies of BE 5 and 6 are similar to those determined in this study. For the bound excitons 5 and 6 the error interval of the obtained activation energies includes the spectral distances between the bound exciton lines and the upper and lower branches of the A exciton-polariton, suggesting that the 5 and 6 PL lines can be associated with a hole from the A valence sub-band. The activation energy obtained for BE 8 is slightly smaller than the spectral distances between the two polariton branches and the A FE but it is likely to be associated with the A FE.

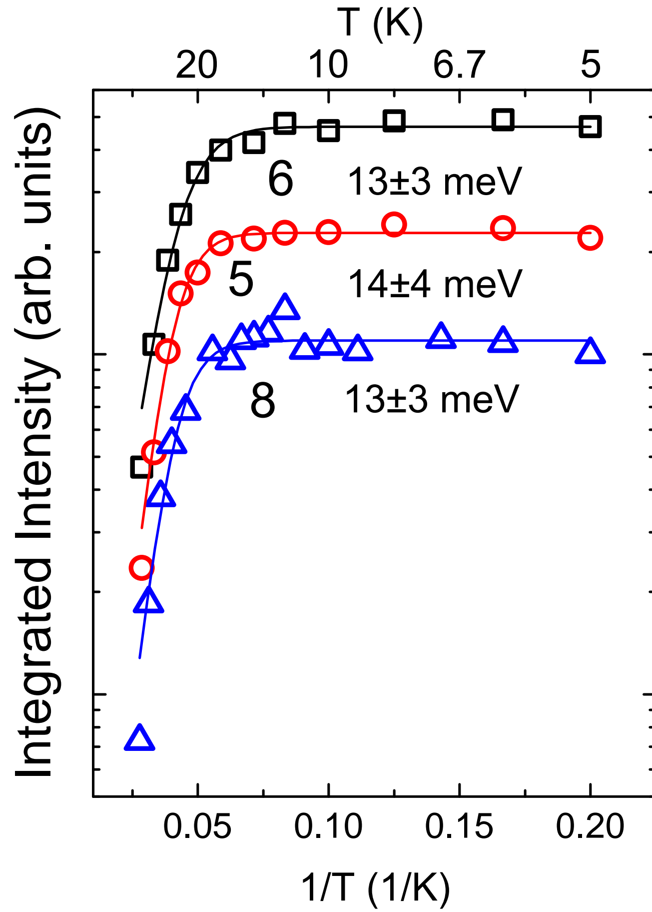

Figure 5.17: Arrhenius plot of the integrated PL intensity of the bound excitons 5, 6 and 8 fitted using Eq. 2.20.

5.3.3 FWHM as a Function of Temperature

The temperature dependence of the FWHM of the A free exciton is shown in Fig. 5.18. The FWHM of the A free exciton line is increasing with increasing temperature due to exciton-phonon scattering. In Fig. 5.18 it can be seen that at temperatures up to 45 K the increase of the FWHM is linear. At temperatures higher than 45 K, a change in the linear dependence of the FWHM on the temperature occurs. A similar behaviour of the FWHM was observed for the B FE in Section 4.3.3 for $CuInSe_2$. The linear increase at temperatures below 45 K suggests that acoustic phonon scattering dominates in this region (Chapter 2.4.1) and the temperature dependence of the FWHM of the exciton can be described by [69]:

$$\Gamma(T) = \Gamma_0 + \Gamma_a T \tag{5.3}$$

The linear fit of the experimental data yields an exciton-acoustic-phonon coupling strength of Γ_a=22±2 μeV/K and a broadening parameter of Γ_0=1.94±0.02 meV

PL line	$E_A - E_{BE}$ (meV)	$E_{UPB} - E_{BE}$ (meV)	$E_{LPB} - E_{BE}$ (meV)	E_{a1} (meV)	a_1 (meV)
5	12.9	13.3	11.7	14 ± 4	393
6	15.4	15.7	14	13 ± 3	256
8	19.7	19.9	18.4	13 ± 3	523

Table 5.6: Spectral distances of the BE 5, 6 and 8 from the A FE and the UPB and LPB of the A exciton-polariton, $E_A - E_{BE}$, $E_{UPB} - E_{BE}$, $E_{LPB} - E_{BE}$, respectively, and the activation energy E_{a1}, process parameter a_1 of the bound exciton lines 5, 6 and 8 in $CuInS_2$.

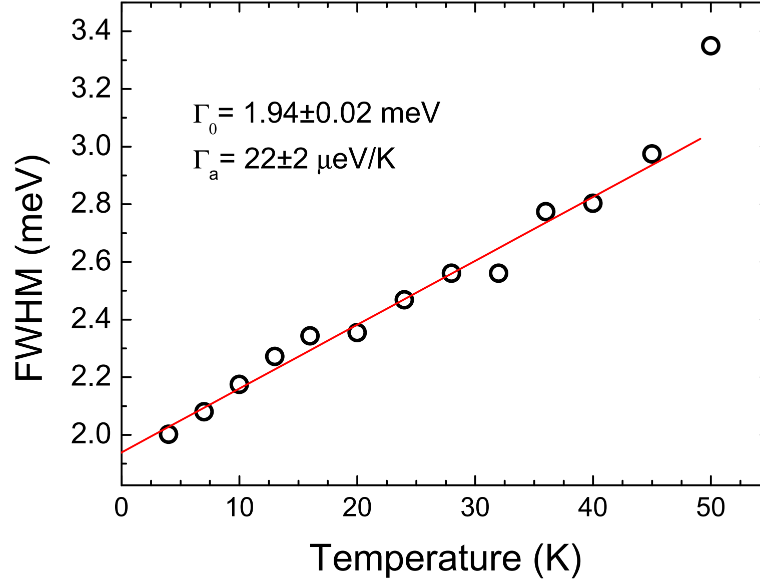

Figure 5.18: Evolution of the FWHM of the A free exciton with increasing temperature from 4.2 to 50 K, fitted with Eq. 5.3.

for the A free exciton. The coupling strengths obtained (not shown here) for the UPB and LPB lie within the obtained error interval of Γ_a for the A FE. The exciton-acoustic-phonon coupling strength is slightly larger than that of Γ_a=15±3 μeV/K determined for $CuInSe_2$ in Section 4.3.3 and Γ_a=9±5 μeV/K for $CuGaSe_2$ in Section 6.3.3.

For temperatures above 45 K the influence of optical phonons should increase and the dependence of the FWHM on the temperature should follow an exponential function. However, there are not enough data points above 45 K to estimate a value of the optical phonon energy.

5.4 Magneto-Photoluminescence of $CuInS_2$

The evolution of the A exciton-polariton PL in $CuInS_2$ under the influence of a magnetic field from 0 to 20 T, taken at 4.2 K, is shown in Fig. 5.19. The PL

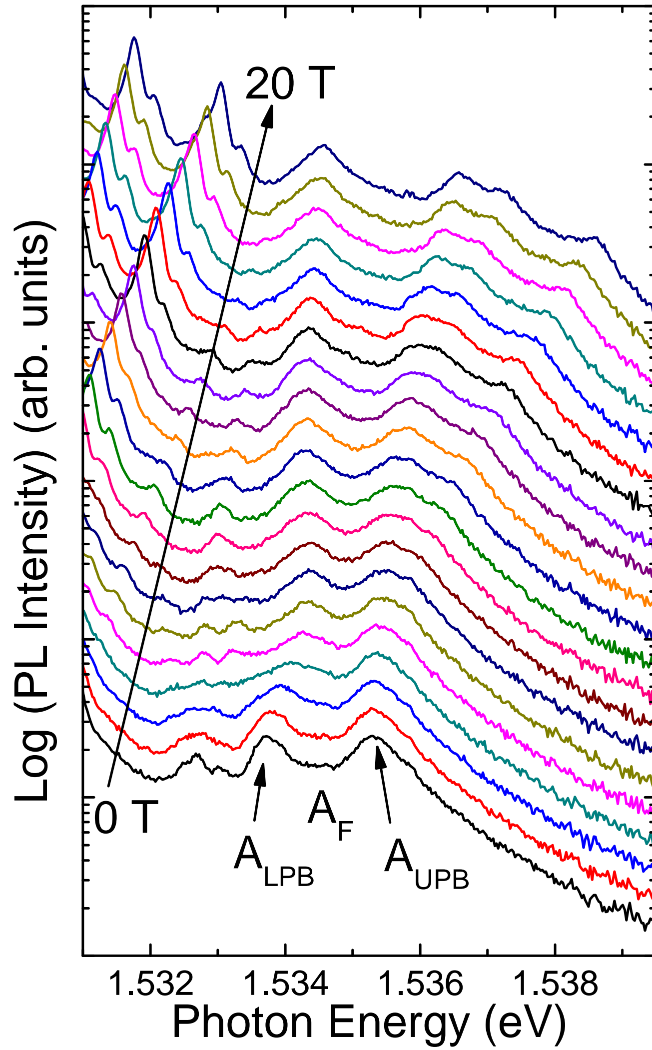

Figure 5.19: Evolution of the PL spectra of the A exciton-polariton under an applied magnetic field from 0 to 20 T, taken at 4.2 K.

spectra were measured for magnetic fields applied along the z-direction within an uncertainty of 20°. With increasing magnetic field strength a non-linear blueshift and Zeeman splitting of the UPB of the A exciton-polariton becomes visible. In contrast, the LPB exhibits a blueshift of ~ 0.6 meV up to 6 T. At magnetic fields greater than 6 T the LPB seems to deviate from the non-linear blue shift of the UPB and exhibits a small redshift of 0.1 meV until 13 T which is then followed by a small blueshift of 0.3 meV.

The dependencies of the spectral positions of the UPB and LPB on the magnetic field are shown in Fig. 5.20. It can be seen in Fig. 5.20 that the UPB splits into three components which shift towards higher energy at different rates, in particular UPB". In contrast, the LPB does not exhibit any splitting. The nature of the UPB splitting is not clear at this time. A theoretical model, explaining

the Zeeman splitting of the UPB is necessary and currently being developed by Dr. Anna Rodina of A. E. Ioffe Physico-Technical Institute.

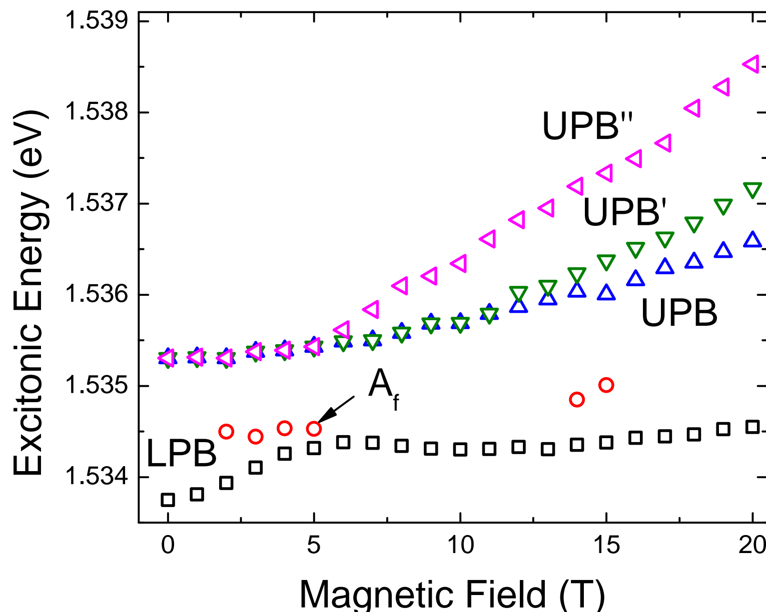

Figure 5.20: Dependence of the UPB and LPB spectral positions on the applied magnetic field.

5.4.1 Diamagnetic Shift of Polaritons in $CuInS_2$

In order to estimate the extent of the low-field region the reduced mass was estimated as μ=0.142 m_0 using m_e=0.16 m_0 and m_h=1.3 m_0 [26]. Using the experimental value of the binding energy, 18.5 meV [112], as Ry^* gives a value of γ=0.31 at 14 T. For $\gamma \ll 1$ the coulomb interaction dominates and the magnetic field can be treated as a perturbation (Chapter 2.5). This suggests that the weak field limit may be valid up to 14 T. The quadratic expression (Eq. 2.34) was used to least square fit the experimental data shown in Fig. 5.21. The experimental data points are the mid-points between the components UPB and UPB', UPB and UPB" as well as between UPB' and UPB". The best fit for (UPB+UPB')/2 and (UPB'+UPB")/2, corresponding to the maximum value of the square of the correlation coefficient R^2=0.996 and 0.992, respectively, was obtained for the data points up to 20 T. Whereas the best fit for (UPB+UPB")/2, corresponding to the maximum of R^2=0.991 was obtained for the data points up to 14 T. This suggests that the weak field approximation works well for (UPB+UPB')/2 and (UPB'+UPB")/2 up to 20 T but only up to 14 T for (UPB+UPB")/2. The diamagnetic shift rates of the fits in Fig. 5.21 are summarised in Table 5.7. The

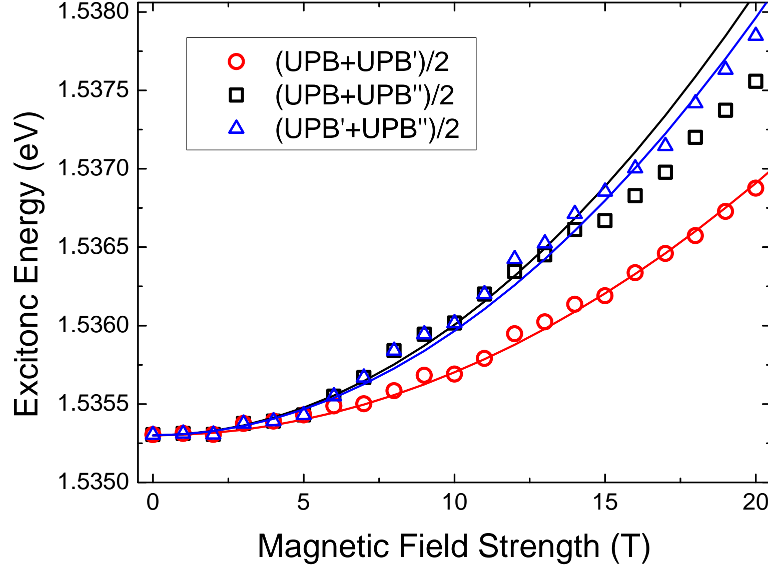

Figure 5.21: Mid-points between the components UPB and UPB', UPB and UPB" as well as between UPB' and UPB" fitted with Eq. 2.34 .

reduced masses were calculated using Eq. 2.35 and the literature value of the static dielectric constant ϵ=10.2 [26,112] as 0.147 m_0, 0.122 m_0 and 0.124 m_0 for (UPB+UPB')/2 (UPB+UPB")/2 and (UPB'+UPB")/2 respectively.

Polariton Branch	(UPB+UPB')/2	(UPB'+UPB")/2	(UPB+UPB")/2
c_d (eV/T^{2}x10^{-6})	4.00 $\pm$ 0.05	6.6 $\pm$ 0.1	7.0 $\pm$ 0.2
μ/m_0	0.147 $\pm$ 0.001	0.124 $\pm$ 0.001	0.122 $\pm$ 0.002

Table 5.7: The experimental values of the diamagnetic shift rates c_d and the calculated reduced masses μ calculated using Eq. 2.35.

Yakushev et al. [121] reported a value of 0.142 m_0 for the reduced mass of the UPB of the exciton-polariton which was determined from magneto-PL measurements up to 10 T. The authors did not resolve any Zeeman splitting of the polariton lines. Their reduced mass value is the same as the value calculated from the literature values of the electron and hole mass [26]. The reduced mass value for UPB (corresponding to (UPB+UPB')/2) determined here is slightly larger than the literature values. The reduced masses of the high energy components UPB' and UBP" (corresponding to (UPB'+UPB")/2 and (UPB+UPB")/2, respectively) were determined as 0.124 m_0 and 0.122 m_0, respectively. These two values coincide within their errors.
Using the literature value of the effective electron mass m_e=0.16 m_0 [26], a value of the effective hole mass for the UPB can be estimated as m_h=1.76 m_0. For the

UPB' and UPB" hole masses of m_h=0.55 m_0 and m_h=0.51 m_0, respectively, have been obtained. As can be seen from Fig. 5.20 UPB' and UBP" are additional components of the UPB of the exciton-polariton, exhibiting lighter hole masses than the UPB.

The Rydberg energies Ry^* can be calculated using Eq. 2.8, the determined reduced masses and a static dielectric constant of ϵ=10.2 [26, 112] as 19.2, 16.2 and 15.9 meV for UPB, UPB' and UPB", respectively. The values for UPB (corresponding to (UPB+UPB')/2) are in good agreement with those determined by Yakushev et al. [112] as 18.5 and 19.9 meV, from the spectral position of the first two excited states. In contrast, the Rydberg energies of the UPB' and UPB" components(corresponding to (UPB'+UPB")/2 and (UPB+UPB")/2, respectively) are much smaller than the literature values. The exciton Bohr radius (Eq. 2.10) of UPB is estimated as 3.7 nm which is in excellent agreement with the literature value [112] whereas the radii for UPB' and UPB" are larger. Person Ref [46], however, theoretically estimated a value of 0.40 m_0 for the effective hole mass which is similar to those of UPB' and UPB". The results of this section are summarised in Table 5.8.

Component	c_d(eV/T^2)	μ/m_0	Ry^* (meV)	a_B (nm)	m_h/m_0
UPB [(UPB+UPB')/2]	4.0x10^{-6}	0.147	19.2	3.7	1.76
UPB' [(UPB'+UPB")/2]	6.6x10^{-6}	0.124	16.2	4.4	0.55
UPB" [(UPB+UPB")/2]	7.0x10^{-6}	0.124	15.9	4.4	0.51

Table 5.8: Effective Rydberg Ry^*, Bohr radius a_B, effective hole mass m_h, and reduced mass μ of the three components of UPB of the A exciton-polariton calculated from the rate of the diamagnetic shift c_d.

If the average of all 4 transitions (UPB, UPB, UPB" and LPB) is fitted from 5-20 T then the diamagnetic shift and reduced mass are 3.94±0.04x10^{-6} eV/T^2 and 0.147 m$_0$, respectively. These coincide with the values for (UPB +UPB')/2 and are close to the literature values.

In conclusion, from Table 5.8 it can be seen that only values for the UPB component which correspond to the mid-points (UPB+UPB')/2 are in agreement with the literature values of the reduced mass, binding energy and Bohr radius. For both data sets involving the UPB" component ((UPB'+UPB")/2 and (UPB+UPB")/2) the determined values of the reduced mass, Rydberg energy and Bohr radius deviate from the literature values suggesting a different origin of UPB" which is agreement with its larger diamagnetic shift.

5.5 Summary

A PL study of the free and bound excitons in $CuInS_2$ as a function of excitation power, temperature and applied magnetic field has been performed. The comparison of the PL spectra of different samples and/or spots on the sample shows that the defect concentration has an influence on the A FE exciton luminescence. A high defect concentration associated with the BE line 2 and low defect concentration associated with BE 5 results in a resolved doublet structure for the A FE which was associated with the upper and lower polariton branch of the A exciton-polariton.

Excitation power dependent PL measurements resulted in a slightly larger power coefficient of the UPB suggesting an increase in the UPB population with increasing excitation power. In addition it was shown that the BE lines 1, 2 and 5 are excitons bound to hydrogenic shallow defects whereas BE line 6 and 8 appear to be excitons bound to more complex defects with a lower concentration than those associated with lines 1, 2 and 5.

The temperature quenching analysis of the A FE, UPB and LPB PL lines leads to activation energies of 14, 15 and 2.6 meV for the A FE, UPB and LPB, respectively. In addition, a thermal redistribution of excitons from the LPB towards the UPB at temperatures above 9 K due to their small energetic separation was revealed.

Thermal activation energies for the 2, 5, 6 and 8 bound excitons have also been determined. It has been suggested that a hole from the A valence sub-band is involved in the exciton formation.

The analysis of the FWHM of the A FE line revealed that below 45 K acoustic phonon scattering is dominant. The resulting coupling strength was determined as 22 μeV/K.

Magneto-PL measurements revealed that the UPB of the A exciton-polariton splits into three components under an applied magnetic field whereas no splitting was observed for the LPB. Only the results of the reduced mass, Rydberg energy and Bohr radius for the mid-points of the UPB and UPB' agreed with the literature values whereas UPB" was suggested to be of a different origin.

Chapter 6

$CuGaSe_2$

$CuGaSe_2$ is a ternary chalcopyrite compound with a direct band gap of ∼1.7 eV. In order to match the band gap to the solar radiation spectrum, $CuGaSe_2$ is alloyed with $CuInSe_2$ forming $Cu(In,Ga)Se_2$ (CIGS) which is used as an absorber layer in thin-film solar cells. The alloying results in an improved performance of the CIGS-based solar cells which demonstrate the highest efficiencies amongst the thin-film photovoltaic devices.
The results of PL measurements on the chalcopyrite compound $CuGaSe_2$ as a function of excitation power, temperature and an applied magnetic field are presented in this chapter. The detailed analysis of the results yielded information on the fundamental properties of $CuGaSe_2$ which are summarised in this chapter.
The excitation power and temperature dependent PL measurement were performed at Strathclyde whereas the magneto-PL was obtained at the GHMFL using the set-ups described in Chapter 3. The magneto-PL results have been published in [122].
The examined $CuGaSe_2$ single crystal was grown from a stoichiometric mixture of Cu, Ga, and Se elements of 99.999% purity using the vertical Bridgman technique (see Chapter 3).

6.1 Excitons in $CuGaSe_2$

The near band-gap region of the RF and PL spectra taken in $CuGaSe_2$ at 5 K and 4.4 K, respectively, are shown in Fig. 6.1. The RF spectrum reveals a prominent resonance at 1.727 eV, assigned to the ground state of the A free exciton. The A, B, and C free exciton resonances, corresponding to the three valence sub-bands, have been observed in reflectivity spectra at 1.729 eV, 1.813 eV, and 2.016 eV at

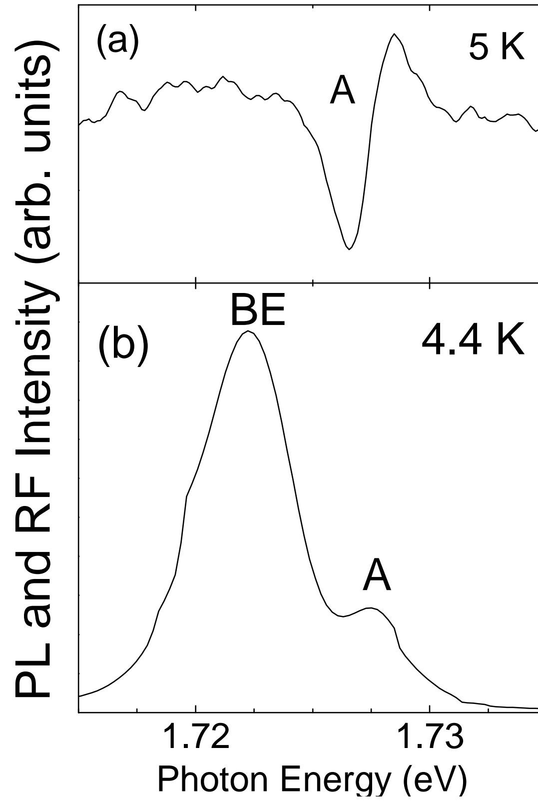

Figure 6.1: RF (a) and PL (b) near band-gap spectra for CuGaSe2 single crystals, taken at 5 K and 4.2 K, respectively.

77 K, respectively, by Ref. [36]. The peak at similar energy in the PL spectrum as the A exciton resonance in the RF spectrum can be attributed to the A free exciton. The higher intensity peak at 1.722 eV, visible in the PL spectrum, has also been observed at 10 K in the literature [31, 123] and was assigned to bound exciton recombination which will be confirmed by the temperature dependent PL measurements in section 6.3.
Several authors observed excitonic emission in $CuGaSe_2$ single crystals [31,34,124] as well as in epitaxial layers on GaAs [31,32,125]. However, only a few studies on well resolved free and bound exciton PL lines have been performed so far [31,123]. This work presents results of PL measurements as a function of excitation power, temperature and applied magnetic field on a $CuGaSe_2$ single crystal. Excitation power and temperature dependent PL measurements on $CuGaSe_2$ single crystals have been performed by Bauknecht et al. [31]. Free and bound excitonic recombination was identified but no activation energies of the free and bound exciton were determined and the temperature dependence of the PL FWHM was not studied.
In order to analyse the excitonic lines in more detail, the PL spectrum has been

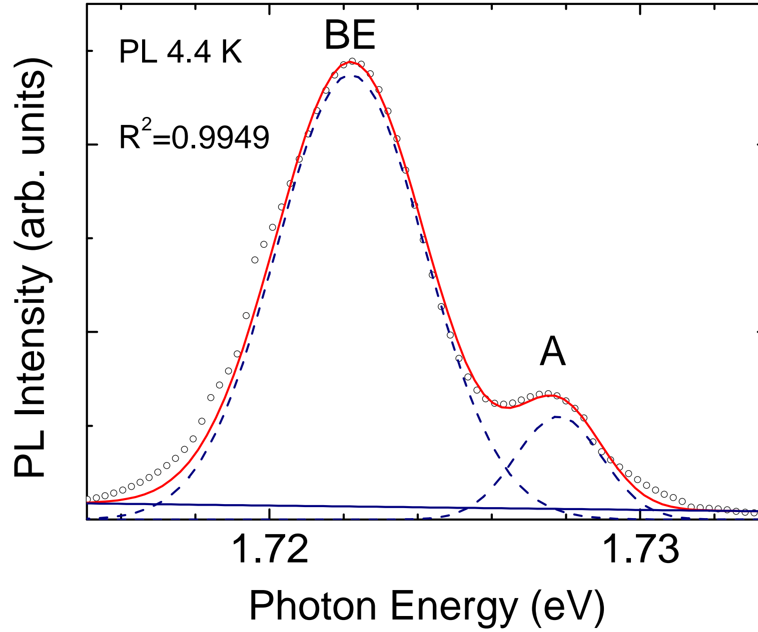

Figure 6.2: Fit of the $CuGaSe_2$ PL spectrum with Gaussian line shapes (circles-data, blue-individual Gaussian and red-fit line).

fitted with a Gaussian line shape, as shown in Fig. 6.2. Generally, excitonic lines can be well described by Lorentzian curves but for the $CuGaSe_2$ PL spectrum in Fig. 6.2 Gaussian curves have been found to describe the BE and FE peaks well. Strong exciton-phonon coupling, crystal imperfections, impurities and strain can cause inhomogeneous broadening of the excitonic lines. Gaussian curves are generally expected when the inhomogeneous broadening has a significant influence (see Chapter 2.4.1). Further details on the line broadening in $CuGaSe_2$ will be given in section 6.3.3.

The observed Gaussian shapes of the excitonic lines suggest that the studied $CuGaSe_2$ single crystal exhibits either stronger exciton-phonon coupling or a higher concentration of defect and impurities compared to the studied $CuInSe_2$ and $CuInS_2$ single crystals where Lorentzian line shapes were observed for the excitonic PL lines (Chapters 4 and 5).

The spectral positions and the FWHM obtained by least-square fitting the $CuGaSe_2$ PL spectrum, as displayed in Fig 6.2, are shown in Table 6.1. The FWHM of the A free exciton line is about 2.9 meV whereas the FWHM of the BE is about 4.9 meV. Compared to bound excitons in $CuInSe_2$ and $CuInS_2$ (see Chapters 4 and 5), where FWHMs are generally below 1 meV, the FWHM of the observed bound exciton line in $CuGaSe_2$ is rather large. This large FWHM of the BE PL line suggests that the line may consist of several unresolved bound exciton lines.

In addition, a high concentration of defects, alloy disorder and composition fluctuation, which are common in ternary alloys, could be responsible for the large FWHM of the excitons. Further discussions can be found in Section 6.3.2.
In order to study the properties of the excitonic lines in $CuGaSe_2$ PL spectra as a function of excitation power, temperature dependence and applied magnetic field have been recorded.

PL line	Energy (eV)	FWHM (meV)	Exciton Type
A	1.728	2.9	FE
BE	1.722	4.9	BE

Table 6.1: Spectral positions, FWHM and the assignment of the PL lines obtained by least-square fitting the $CuGaSe_2$ spectrum, taken at 4.4 K, with Gaussian curves.

6.2 Excitation Power Dependent Photoluminescence

Excitation power dependent PL measurements were performed for excitation powers ranging from 6.4 to 200 mW (corresponding to power densities from 13 to 430 W/cm^2 on the sample) at 4.3 K and are shown in Fig. 6.3. The spectral position of the excitonic peaks does not change with variations in the excitation power. In addition, the changes of the FWHM of both PL lines are small. Each spectrum shown in Fig. 6.3 has been least-square fitted with Gaussian curves as shown in Fig.6.2 in order to gain information about the excitation power dependent behaviour of the two excitonic lines.

6.2.1 Integrated Emission Intensity as a Function of Excitation Power

From the fit of each individual PL spectrum, the dependencies of the integrated PL intensity I of the free and bound excitons on the excitation power P have been obtained and are shown in Fig. 6.4. The dependence of the PL intensity on the excitation power follows the power law $I \sim P^k$ and $1<k<2$ is expected for exciton-like transitions as discussed in Section 2.4.3. Power coefficients of 1.39 and 1.4 were determined for the A free and the bound exciton, respectively, suggesting their excitonic nature and are summarised in Table 6.2.

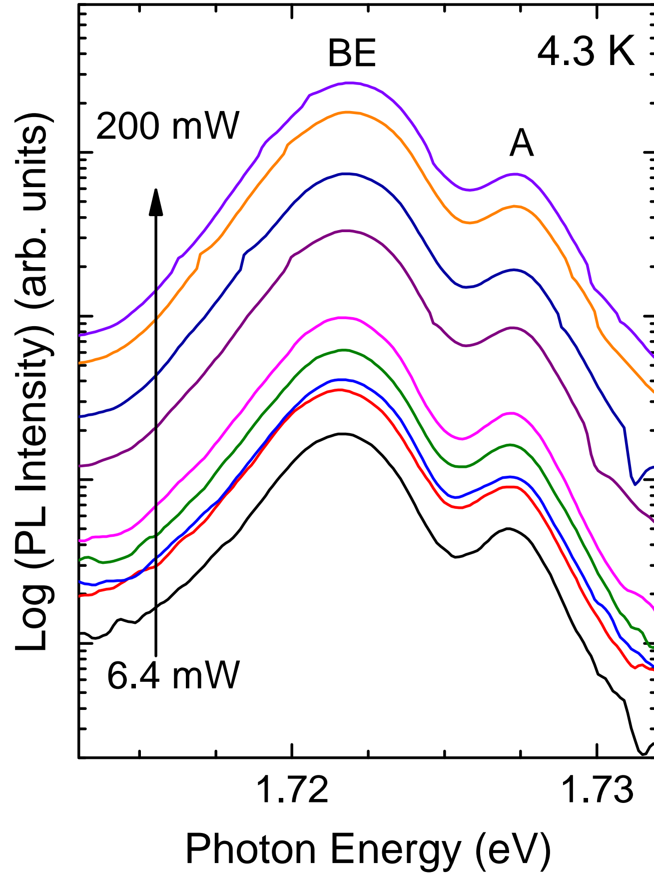

Figure 6.3: Excitation power dependence of the excitons in $CuGaSe_2$.

PL line	Energy (eV)	*k*
A	1.728	1.39
BE	1.722	1.4

Table 6.2: Spectral positions and k coefficients of the A free and bound exciton.

The power coefficients of the A FE and the bound exciton coincide which is not expected. For both $CuInSe_2$ (Section 4.2) and $CuInS_2$ (Section 5.2), the BE k coefficients have been found to differ from those of the FE. For the FE in $CuInSe_2$ k coefficients of 1.36 and 1.40 for the A and B FE, respectively, have been found which are in agreement with that of the A FE in $CuGaSe_2$. In contrast, the power coefficients in $CuInS_2$ were determined as 1.10 and 1.23 for the LPB and UPB, respectively. With increasing excitation power the FWHM of the A FE and the BE increases by about 5 and 8 %, respectively. The increase of the FWHMs could be due to an increase in sample temperature at high excitation power. This behaviour could be a reason for the similar power coefficients. As suggested before the BE PL line could consists of multiple unresolved bound exciton lines

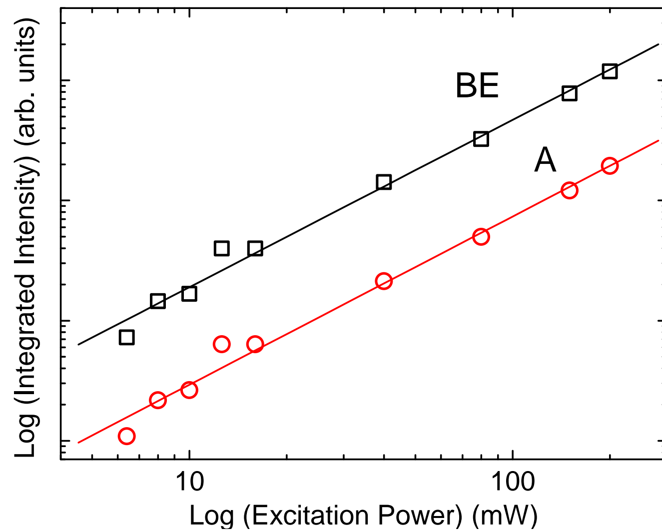

Figure 6.4: Dependence of the PL intensity on the excitation power of the A free and bound exciton, fitted linearly (open symbols - data, line - linear fit.

which could have an influence on the excitation power dependence.

6.3 Temperature Dependent Photoluminescence

Fig. 6.5 shows the evolution of the $CuGaSe_2$ PL spectra as a function of temperature. It can be seen that the BE peak quenches at a faster rate than the free exciton peak with increasing temperature. At about 120 K the BE peak has nearly disappeared whereas the A peak can still be seen at 180 K. The faster thermal quenching of the BE line confirms its assignment as a bound exciton. In contrast to the BE line, the A line is still present at 180 K which confirms the assignment of the A line to a free exciton associated with the A valence sub-band. In addition, three broad PL bands at about 1.688, 1.677 and 1.645 eV can be seen in Fig. 6.5. Similar peaks were observed by Bauknecht et al. in Ref. [31] and identified as free-to-bound transitions.

6.3.1 Spectral Position of the A exciton as a Function of Temperature

The evolution of the spectral position of the A exciton peak under increasing temperature from 4.4 to 180 K is shown in Fig. 6.6. Up to about 40 K the FE peak position remains constant. For temperatures above 40 K the peak position of the A exciton decreases due to phonon interaction which results in a reduced

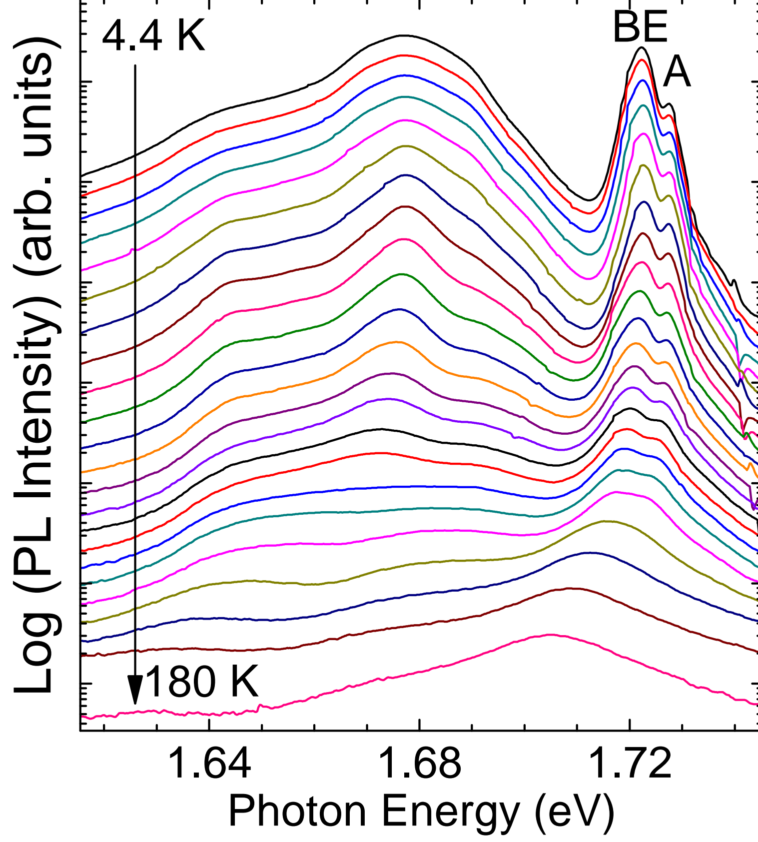

Figure 6.5: Temperature dependence of the spectral position of the A free exciton in $CuGaSe_2$.

bond energy of the crystal lattice leading to a red shift of the band gap energy. In addition, the thermal expansion of the lattice affects the band gap energy. The temperature dependence of the A exciton can be described by Eq. 6.1 [98] (see also Section 4.3.1):

$$E_A(T) = E_A(0) - S\langle\hbar\omega\rangle\left[coth\left(\langle\hbar\omega\rangle/2kT\right) - 1\right] \tag{6.1}$$

The fit of the experimental points with Eq. 6.1 resulted in $S = 1.1 \pm 0.1$ and $\langle\hbar\omega\rangle = 23.2 \pm 1.2$ meV. Average phonon energies of 18 and 26 meV have been reported by Meeder et al. [34] and Yamada et al. [32] from the fit of the temperature dependence of the A FE spectral position. In addition, Rincon et al. [126] reported nine optical phonon modes at room temperature, varying from 60 cm^{-1} (7.4 meV) to 273 cm^{-1} (33.8 meV). However, the strongest mode was found at 184 cm^{-1} which corresponds to 22.8 meV. The determined average phonon energy of 23.2 ± 1.2 agrees well with the values reported in literature.

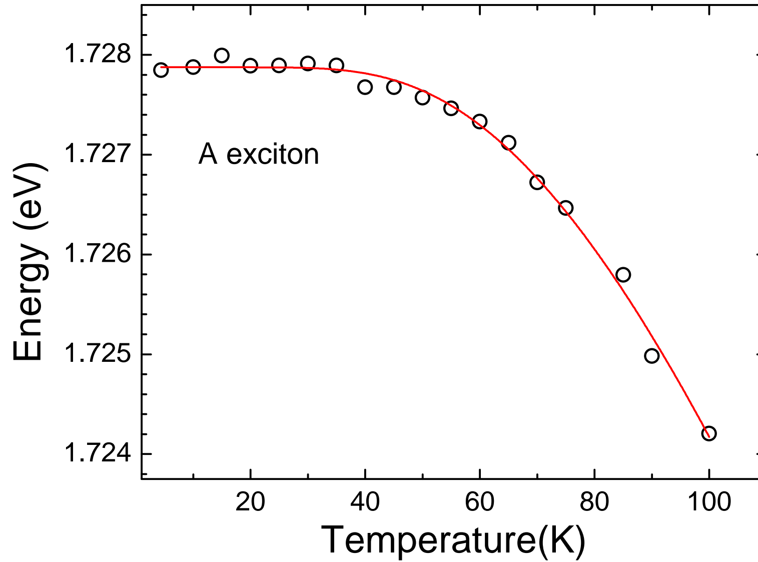

Figure 6.6: Temperature dependence of the A exciton peak (circles-data and red-fit line with Eq. 6.1).

The value of the electron-phonon coupling parameter S is close to the value of 1.29 determined by Meeder et al. [34] but lower than that for semiconductors such as Si, GaAs, GaP and C [98]. For $CuInSe_2$ a smaller value of the Huang-Rhys parameter of 0.66±0.05 was determined in Section 4.3.1. It can be concluded that the interaction between excitons and phonons in $CuGaSe_2$ is weaker than in Si, GaAs, GaP and C but slightly larger than in $CuInSe_2$.

6.3.2 Integrated Emission Intensity as a Function of Temperature

6.3.2.1 A Free Exciton

The integrated intensity plotted versus the inverse temperature for the A free exciton is shown in Fig. 6.7. The least-square fit of the experimental points, using Eq. 2.20 from Section 2.4.2, yields an activation energy of E_{a1}=14.6±1.6 meV and a process parameter of a_1=75±30 for the A free exciton. These values agree well with those reported in the literature. Yamada et al. [32] estimated an activation energy of 16.2 meV from the temperature quenching analysis of the A FE PL line in $CuGaSe_2$ films on GaAs. However, their FE PL line was not clearly resolved. In contrast, Bauknecht et al. [31] determined a binding energy of 13 ± 2 meV from the spectral position of the A exciton excited states. Using a reduced mass of μ=0.125m_0 [31] and a static dielectric constant of ϵ=11 [31]

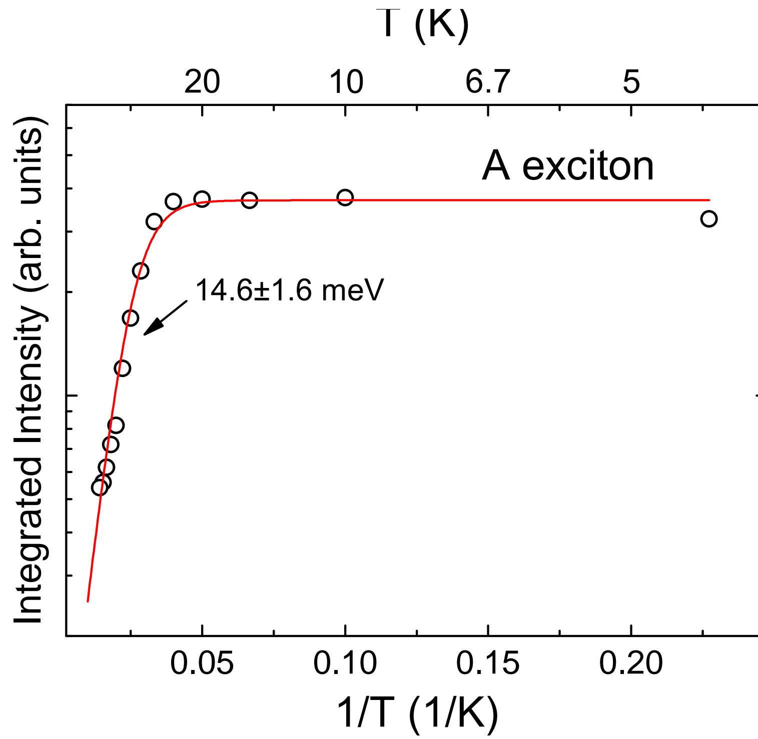

Figure 6.7: Arrhenius plot of the integrated intensity of the A free exciton fitted with Eq. 2.20 (circles - data, red - fit line).

results in a value of about 14 meV for the Rydberg energy Ry^* (Eq.2.8). This agrees well with the determined activation energy of the A exciton, in contrast to the other two compounds studied in this thesis, as discussed in Chapter 7.

6.3.2.2 Bound Exciton

The Arrhenius plot of the integrated intensity of the A FE in comparison with that of the BE is shown in Fig. 6.8. The integrated intensity of the BE has been fitted with Eq. 2.21, assuming two non-radiative activation channels, as suggested by Bimberg et al. for bound excitons in GaAs [72]. In Chapters 4 and 5 Eq. 2.21 has also been used for the shallowest BE in $CuInSe_2$ and $CuInS_2$, respectively.

Fitting the experimental points of the integrated intensity with Eq. 2.21 resulted in two activation energies E_{a1} and E_{a2}, as shown in Table 6.3 together with the spectral distance between the BE and FE. For temperatures below 30 K (∼0.03 1/K) an activation energy E_{a1} of 8.8 meV has been determined for the BE. This value is larger than the spectral distance between the BE and FE of 5.8 meV.

The first decrease of the BE line intensity could be interpreted as thermal detrapping of these excitons towards the A FE. However, no intensity increase of

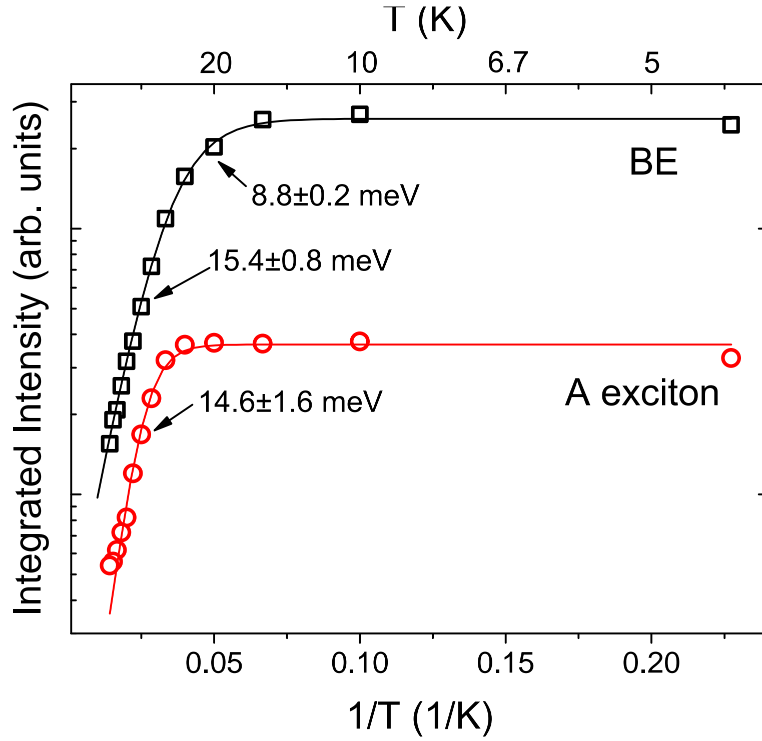

Figure 6.8: Arrhenius plot of the integrated intensity of the bound exciton fitted with Eq. 2.21 (circles - data, red - fit line).

the A FE was observed as was seen for $CuInSe_2$ and $CuInS_2$ in Chapters 4 and 5, respectively. The second activation energy E_{a2} has been determined as 15.4 meV for the BE exciton. This second non-radiative activation channel becomes effective at temperatures above 30 K (~0.03 1/K) where the quenching of the PL intensity of the A FE is also effective. As seen in Chapters 4 and 5 the dissociation of the A FE into one free hole and one free electron would suggest that E_{a2}=E_{a1}+E_a^A [72] with E_a^A being the dissociation energy of the A FE. E_a^A has been found as 14.6±1.6 meV from the fit of the A FE as described earlier in this chapter. The values in Table 6.3 show that the sum E_{a1}+E_a^A is larger than E_{a2}. However, this difference could be explained by the larger activation energy E_{a1} of the BE for temperatures below 30 K. The large FWHM of the BE line suggested that it could contain multiple bound exciton lines. Therefore the determined activation energy E_{a1} could account for more than one BE line with different activation energies which could be a reason for the deviation of the activation energy from the spectral distance between the FE and BE. Bauknecht et al. [31] estimated a binding energy of 17 meV for the observed bound exciton which is larger than the activation energy determined here and also larger than their determined binding energy of 13 meV for the A FE . The value of 17 meV

reported by Ref. [31] should be regarded as the total energy of the bound exciton complex, which is the sum of the binding energy of the FE as well as the binding energy to the defect of 4 meV (spectral distance between the BE and FE).

PL line	$\mathbf{E_{BE} - E_{FE}}$ (meV)	$\mathbf{E_{a1}}$ meV	$\mathbf{a_1}$ meV	$\mathbf{E_{a2}}$ meV	$\mathbf{a_2}$ meV
A	-	14.6 ± 1.6	75	-	-
BE	5.8	8.8±0.2	41	15.4±0.8	90

Table 6.3: Spectral distance of the BE from the A free exciton, $E_{BE} - E_{FE}$, activation energies E_{a1} and E_{a2} and process parameters a_{a1} and a_{a2}.

6.3.3 FWHM as a Function of Temperature

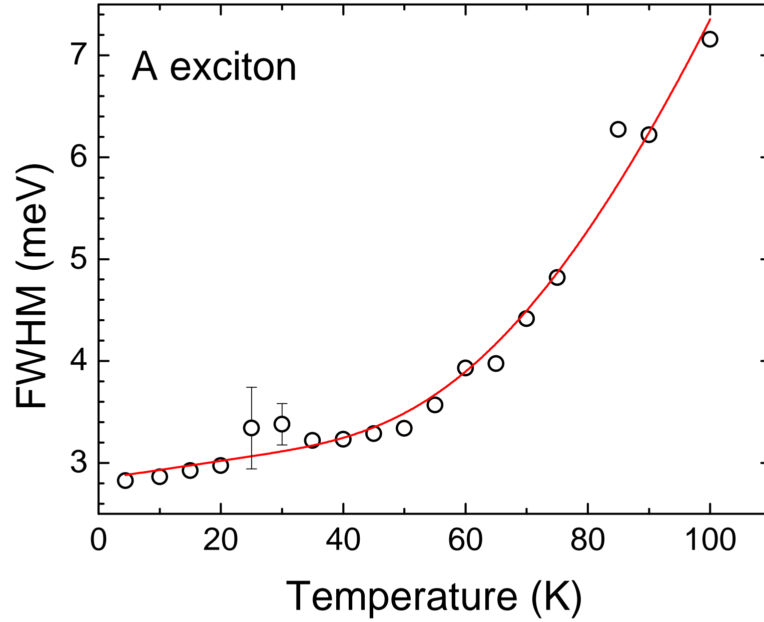

Figure 6.9: Evolution of the FWHM of the A free exciton PL line with temperatures increasing from 4.4 to 180 K, fitted with Eq. 6.2 (circles - data, red - fit line).

The evolution of the FWHM of the A free exciton with temperatures increasing from 4.4 to 100 K can be seen in Fig. 6.9. The FWHM of the A free exciton PL line is increasing with increasing temperature due to exciton-phonon scattering. It can be seen that at lower temperature (<70 K) the increase of the FWHM is nearly linear which indicates the influence of acoustic phonons. At temperatures higher than 70 K, the increase of the FWHM is nearly exponential which suggests that LO phonons should be included (see Section 2.4.1 and Refs. [68–70]). The

experimental points have been fitted with:

$$\Gamma(T) = \Gamma_0 + \Gamma_a T + \frac{\Gamma_{LO}}{\left(exp\left[\frac{\hbar\omega_{LO}}{kT}\right] - 1\right)} \tag{6.2}$$

where Γ_0 is the zero temperature broadening parameter, which can contain information about exciton-exciton interactions in addition to scattering by defects and impurities [69]. Γ_a is the coupling strength of the exciton-acoustic-phonon interaction [69] and Γ_{LO} is a parameter describing the exciton-LO-phonon interaction [70]. $\hbar\omega_{LO}$ is the energy of the LO phonons. The fit yields Γ_0=2.8 ± 0.2 meV, Γ_a=9 ± 5×10^{-3} meV/K, Γ_{LO}=58 ± 30 meV and $\hbar\omega_{LO}$=24 ±5 meV.
A similar value of 20 meV was determined by Yamada et al. [32] from the fit of the FWHM of the free exciton in $CuGaSe_2$ grown on GaAs. The LO phonon energy obtained here agrees well with the value determined in Section 6.3.1 from the fit of the temperature dependence of the spectral position of the A exciton. In addition, the value is close to that reported by Meeder et al. [34] and agrees with 22.8 meV which corresponds to the strongest optical phonon mode observed in Raman spectroscopy by Rincon et al. [126].

6.4 Magneto-Photoluminescence of $CuGaSe_2$

The evolution of the $CuGaSe_2$ PL spectra under the influence of a magnetic field from 0 to 20 T taken at 4.2 K is shown in Fig. 6.11. Increasing the magnetic field strength results in non-linear blue shifts of both the BE and the A free exciton lines. In order to accurately determine the dependence of the spectral position of the A free exciton on the magnetic field strength, the A and BE peaks have been fitted with Gaussians as shown in Fig.6.2 (Section 6.1). The total shift of the A free exciton peak from 0 to 20 T, was measured to be 3.4 meV. The FWHM of the A free exciton peak was determined as 4.5 meV and did not change with increasing magnetic field. The FWHM of the A exciton peak is slightly larger than the one determined in Section 6.1 which could be due to a less resolved A exciton peak and higher defect concentration of the measured sample area. No field-induced peak splittings were resolved in the spectra, which is probably due to the relatively large FWHM.

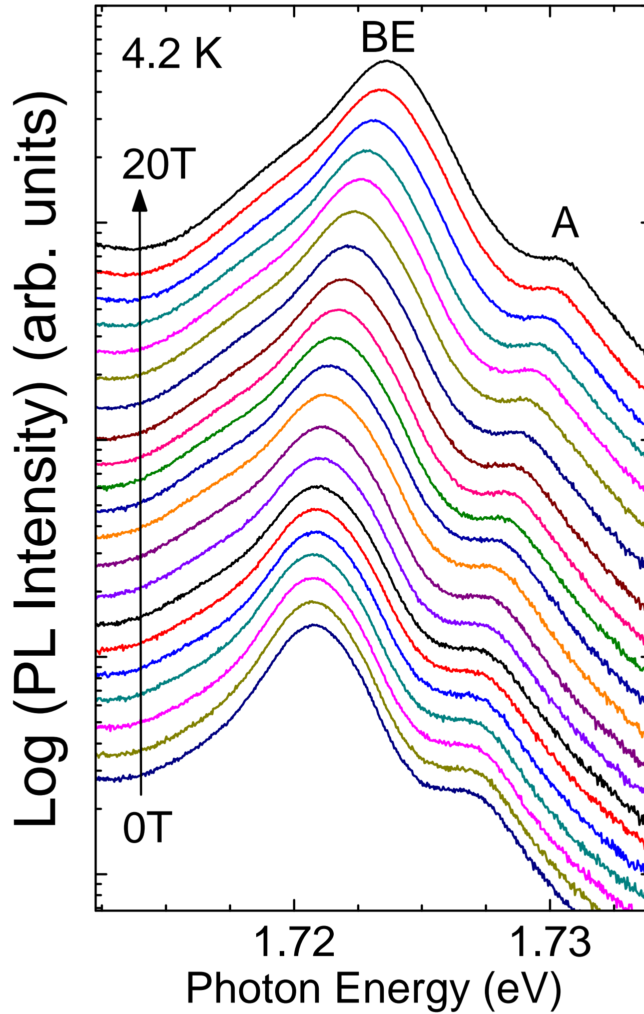

Figure 6.10: PL spectra of the free A exciton and the BE under magnetic fields from 0 to 20 T taken at 4.2 K.

6.4.1 Diamagnetic Shift of the A Free Exciton in $CuGaSe_2$

The evolution of the spectral position of the A exciton peak under increasing magnetic fields from 0 to 20 T is shown in Fig. 6.11.

To estimate the extent of the low-field region the available values of the effective electron and hole masses in $CuGaSe_2$ are used to estimate the A exciton reduced mass as $\mu = 0.125\ m_0$. A hole effective mass of $m_h = 1.2\ m_0$ has been selected as the most reliable value from the wide range of $CuGaSe_2$ effective hole masses. Using the experimental value of the A exciton binding energy (13 meV [31]) as Ry^* gives a value of γ of 0.36 at 10 T. This suggests that up to about 10 T the Coulomb energy dominates and the external magnetic field can be treated as a perturbation, with Eq. 2.34 describing the diamagnetic shift.

The quadratic expression in (2.34) was used to least square fit the experimental

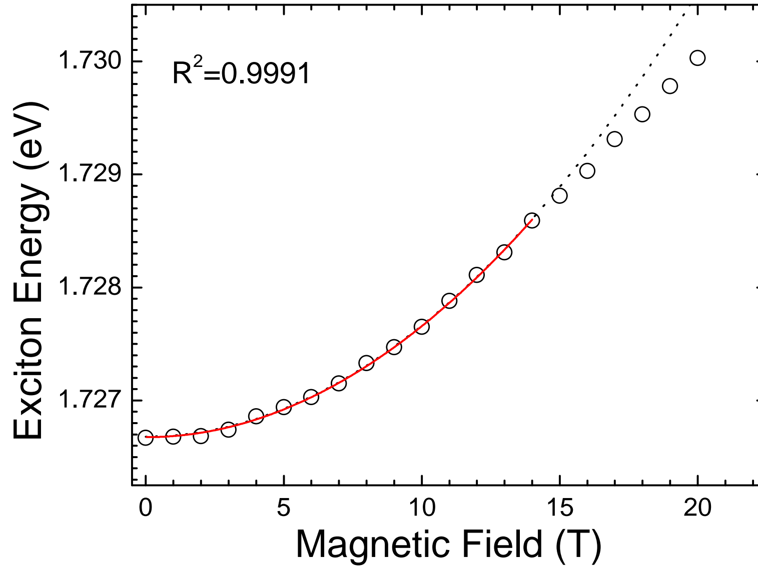

Figure 6.11: The evolution of the free A exciton PL peak position under the influence of a magnetic field. The solid line represents a quadratic fit up to 14 T.

data points up to various maximum values of the field. The best fit, corresponding to the maximum value of the square of the correlation coefficient $R^2 = 0.9991$, was obtained for the data points up to 14 T as shown in Fig. 6.11. This suggests that the weak field approximation works well up to 14 T.

The best fit in Fig. 6.11 corresponds to a diamagnetic shift rate of c_d=(9.82±0.09) x 10^{-6}eV/T^2. A reduced mass of $\mu = 0.115\ m_0$ was then calculated using Eq. 2.35 and the literature value of the static dielectric constant ϵ =11 [31].

There is no experimental value for the electron effective mass m_e in the literature. However, Persson [46] recently reported a theoretical dependence of m_e in $CuIn_{1-x}Ga_xSe_2$ on the content of gallium x as $m_e(CuIn_{1-x}Ga_xSe_2) = (m_e(CuInSe_2) + 0.05x)\ m_0$. Using the experimental value of $m_e(CuInSe_2) = 0.09m_0$ [105] gives a value of $m_e = 0.14m_0$ for the effective electron mass in $CuGaSe_2$, which is identical to the value calculated earlier using the theoretical model of Kildal [127] developed without taking into account the hybridisation of Cu-d with Se-p states. Such a coincidence suggests that Cu-d states do not have much influence on the conduction band near the Γ point. Our reduced exciton mass then leads to an estimate of the hole effective mass as $m_h = 0.64\ m_0$, which falls within the range of experimentally measured values. The value of the excitonic Rydberg energy, estimated from Eq. 2.8 using the determined $\mu = 0.115m_0$ and ϵ =11, is Ry^*= 12.9 meV. This is in good agreement with the activation energy 14.6 ± 1.6 meV determined from the temperature quenching analysis of

the A free exciton (Section 6.3.2) and the value E_b= 13±2 meV, determined from the experimentally measured energy of the A exciton first excited state [31]. The exciton Bohr radius (Eq. 2.10) is estimated as a_B= 5.1 nm. The results of this section are summarised in Table 6.4.

c_d(**eV/T**^{2})	$\mu/\mathbf{m_0}$	**Ry*** **(meV)**	$\mathbf{a_B}$ **(nm)**	$\mathbf{m_h/m_0}$
9.82x10^{-6}	0.115	12.9	5.1	0.64

Table 6.4: Effective Rydberg Ry^*, Bohr radius a_B, effective hole mass m_h, and reduced mass μ of the A exciton calculated from the rate of the diamagnetic shift c_d.

6.5 Summary

A study of the exciation power and temperature dependence of the PL of the free and bound excitons in $CuGaSe_2$ has been performed. In addition, magneto-PL experiments of the A free exciton have been studied.
Excitation power and temperature dependent PL measurements identify the A PL line as free exciton recombination involving a hole from the A valence subband. From the temperature dependence of the spectral position of the A free exciton line an average phonon energy of 23.2 meV was determined. This value is in good agreement with that of the optical phonon energy of 24 meV obtained from the analysis of the temperature dependence of the FWHM of the A PL line. The temperature quenching analysis of the A PL lines leads to an activation energy of 14.6 meV for the A free exciton. In addition, activation energies were determined for the bound exciton.
The diamagnetic shift of the A free exciton lead to the calculation of its reduced mass using a first order perturbation model. An effective hole mass of m_h=0.64 m_0 for the A free exciton was estimated assuming the literature effective mass.

Chapter 7

Discussion and Summary

In this thesis results of the optical study of the three chalcopyrite semiconductors, $CuInSe_2$, $CuInS_2$ and $CuGaSe_2$ are presented. These materials are used in the absorber layers of thin-film solar cells which have achieved record efficiencies for thin-film photovoltaic devices. In order to improve these efficiencies even further a deeper understanding of the fundamental electronic material properties is necessary. The aim of this study is to obtain information on such material properties, for example on the nature of defects and effective masses of charge carriers.
An introduction to chalcopryrite semiconductors is presented in Chapter 2, giving information on the crystal and electronic structure of these compounds as well as on excitons and their properties. A comparison of the band line-ups of the three compounds is shown in Fig. 7.1 which demonstrates the different valence band structures mentioned in Chapter 2.
In Chapter 3 the experimental techniques, including the growth and the photoluminescence techniques used in this work, are presented.
The analysis of the results of the PL measurements of $CuInSe_2$, $CuInS_2$ and $CuGaSe_2$ are presented in Chapters 4, 5 and 6, respectively. The following sections summarise and compare the results of the excitation power and temperature dependent PL as well as the magneto-PL obtained for the three chalcopyrite compounds. This thesis is concluded with suggestions for future work on the optical properties of the three chalcopyrite semiconductors.

7.1 Excitation Power Dependent PL

Excitation power dependent PL measurements identify the A and B (in the case of $CuInSe_2$) PL lines in the three chalcopyrite semiconductors as free exciton

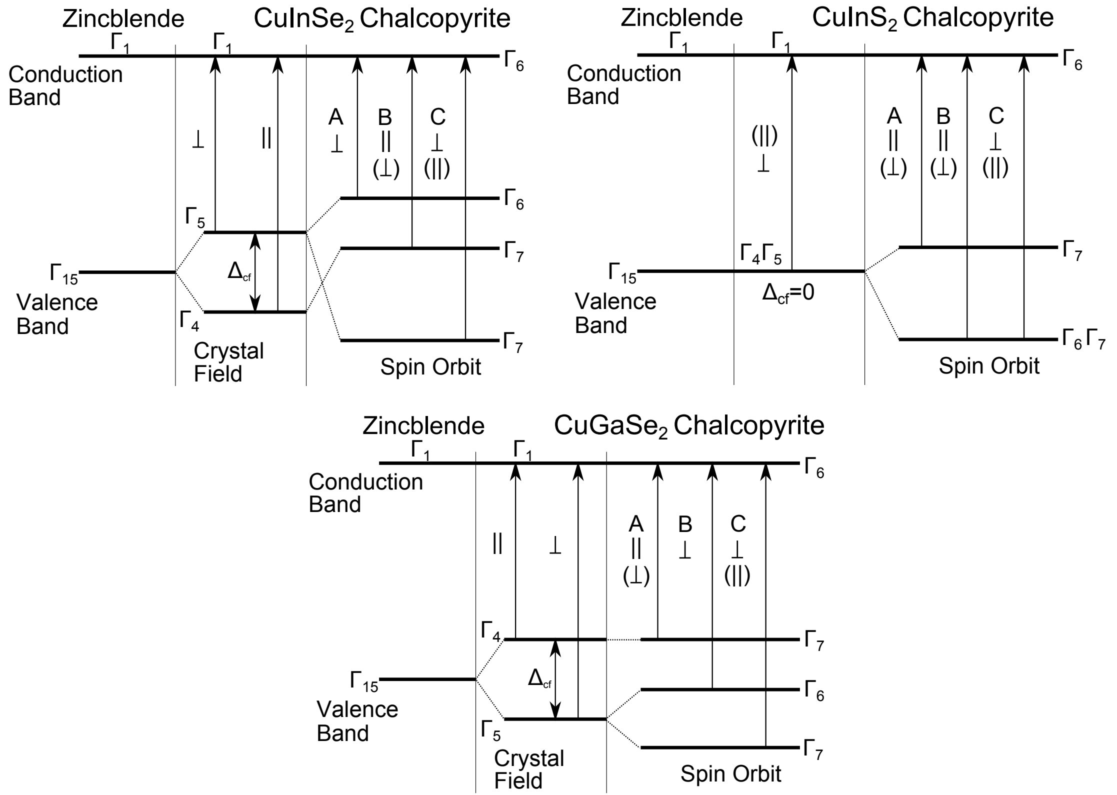

Figure 7.1: Band line-ups and selection rules for the three chalcopyrite compounds $CuInSe_2$, $CuInS_2$ and $CuGaSe_2$.

recombination involving holes from the A and B valence sub-band (Fig. 7.1), respectively. $CuInSe_2$ and $CuInS_2$ PL spectra revealed a large number of sharp lines which were associated with the radiative recombination of bound excitons whereas for $CuGaSe_2$ only one broad bound exciton peak was detected. The shallowest bound excitons in $CuInSe_2$ and $CuInS_2$ were associated with bound excitons to defects with a high concentration whereas the deeper excitons appear to be bound to more complex defects with a lower concentration. Table 7.1

Compound	$\mathbf{k_{FE}}$	$\mathbf{k_{BE}>1}$	$\mathbf{k_{BE}<1}$
$CuInSe_2$	1.4	1.05-1.85	0.6-0.9
$CuInS_2$	1.10-1.23	1.02-1.52	0.8-0.9
$CuGaSe_2$	1.4	1.39	-

Table 7.1: Power coefficients k of the free and bound excitons in $CuInSe_2$, $CuInS_2$ and $CuGaSe_2$.

summarises the power coefficients obtained in Chapters 4, 5 and 6 from $I \sim P^k$ for the free and bound excitons. The power coefficients for the free excitons in $CuInSe_2$ and $CuGaSe_2$ are the same. For $CuInS_2$ the power coefficients for the

upper and lower branch of the A free exciton-polariton are given, thus one has to be cautious with a direct comparison. For all three compounds the power coefficients of the free excitons are $1<k<2$ which is expected for exciton-like transitions [74]. In addition, values of power coefficients above and below unity are observed for the bound excitons.

7.2 Temperature Dependent PL

Different aspects of the temperature dependent PL have been studied in this work. The results of the analysis of the temperature dependence of the spectral position, the integrated intensity and the FWHM were presented in Sections 4.3, 5.3 and 6.3 and are compared in the following sections.

7.2.1 Temperature Dependence of the Spectral Position

The temperature dependent behaviour of the spectral position of the free excitons reflects the temperature dependence of the band gap. It was shown earlier (Sections 4.3, 5.3 and 6.3) that the temperature dependence of the band gap is influenced by the exciton-phonon interaction, thermal lattice expansion and the p-d hybridisation. A comparison of the temperature dependencies of the A exciton spectral position in $CuInSe_2$, $CuInS_2$ and $CuGaSe_2$ is shown in Fig. 7.2.
As seen in Fig. 7.2, for both $CuInSe_2$ and $CuInS_2$ the free exciton PL peak exhibits a blueshift for temperatures below 80 K. The maximum in the spectral position occurs for $CuInSe_2$ at about 70 K and for $CuInS_2$ above 80 K. The blueshift of the $CuInS_2$ exciton peak is ~ 2.2 meV but the blueshift of the $CuInSe_2$ exciton peak is only ~ 0.6 meV. In addition, for $CuInSe_2$ a redshift of the A and B free exciton peaks for temperatures below 23 K was observed. This redshift was not seen for the A FE in $CuInS_2$ and $CuGaSe_2$ but was observed for the UPB in $CuInS_2$ for temperatures below 16 K. Possible explanations for this anomalous behaviour (red-blue-redshift) were given in sectins 4.3.1 and 5.3.1. In contrast, the $CuGaSe_2$ band gap did not show such behaviour which is possibly due to the large FWHM of the FE peak. The FE peak position remains constant and then decreases for temperatures above 40 K.
For $CuInSe_2$ and $CuGaSe_2$ a fit (see Ref. [98]) of the temperature dependence of the spectral position of the A FE yields values for the average phonon values as well as for the exciton-phonon coupling parameter S as shown in Table 7.2. The

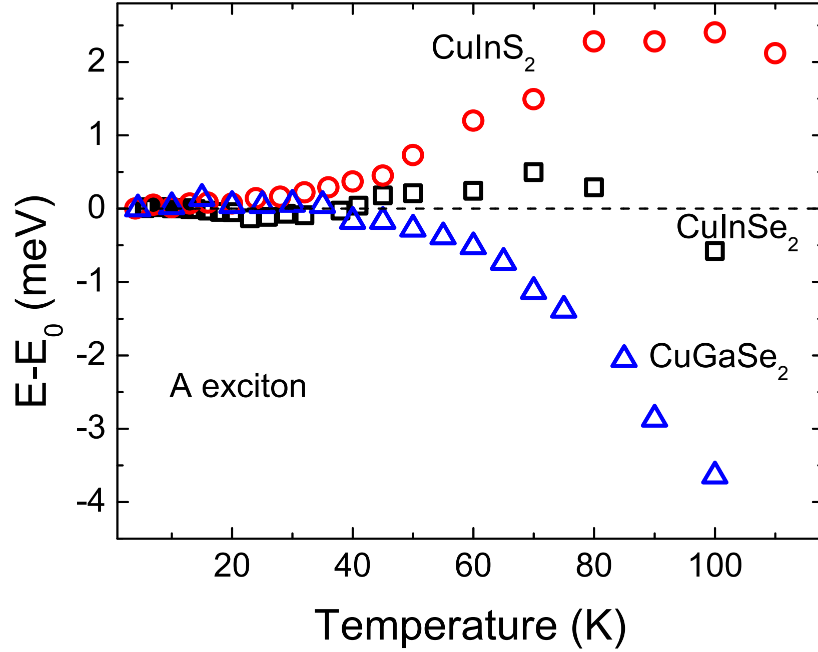

Figure 7.2: A comparison of the temperature dependencies of the A exciton spectral positions.

coupling parameter for $CuGaSe_2$ was found to be larger than that of $CuInSe_2$. Both values are lower than those in Si, GaAs, GaP and C which suggests that the interaction between excitons and phonons are weaker in the two chalcopyrite compounds.

The values of average phonon energy for $CuInSe_2$ and $CuGaSe_2$ agree well with those reported in literature [94, 126].

Compound	S (Huang-Rhys) Parameter	$\langle\hbar\omega\rangle$ (meV)
$CuInSe_2$	0.66±0.05	26±3
$CuGaSe_2$	1.1±0.1	23.2±1.2

Table 7.2: Exciton-phonon coupling parameter S and average phonon energy $\langle\hbar\omega\rangle$ determined from the temperature dependence of the spectral position of the A free exciton in $CuInSe_2$ and $CuGaSe_2$.

7.2.2 Temperature Quenching of the Exciton PL Intensity

The study of the temperature dependence of excitonic luminescence provides information on the activation energy of the underlying process. Activation energies for the free and bound excitons of the three chalcopyrite semiconductors have been obtained. Table 7.3 summarises the activation energies for the free exci-

ton from the analysis of the temperature dependent quenching of the excitonic lines. The activation energies of the A and B free excitons in the highest quality $CuInSe_2$ crystal are found to be 12.5 and 18.4 meV, respectively. As seen from Table 7.3 these activation energies are larger than the binding energy of the excitons [103].

Compound	**E_{a1} (meV)**	**E_B (meV)**
$CuInSe_2$	12.5±1.1 (A) and 18.4±1.6 (B)	8.5 and 8.5 [103]
$CuInS_2$	14±2 (A), 15±2 (UPB) and 2.6±0.6 (LPB)	18.5 [112]
$CuGaSe_2$	14.6±1.6	13 [31]

Table 7.3: Activation energies E_{a1} of the free excitons in the three chalcopyrite compounds $CuInSe_2$, $CuInS_2$ and $CuGaSe_2$ in comparison to the literature values of their binding energies E_B.

The temperature quenching analysis of the A free exciton, UPB and LPB PL lines in $CuInS_2$ leads to activation energies of 14, 15 and 2.6 meV, respectively. As seen from Table 7.3 the determined activation energies are similar to the binding energy of the A free exciton [112].
For $CuGaSe_2$ the activation energy of the A free exciton was found to agree with its binding energy [31].
Fig. 7.3 plots the difference between the thermal activation and binding energies of the three studied compounds versus the splitting between the A and B free excitons. As can be seen the activation energy of the B FE in $CuInSe_2$ exhibits the largest deviation from the exciton binding energy whereas the activation energy of the A FE in $CuGaSe_2$ is in the closest agreement with the exciton binding energy similar to those in GaN [71]. From Fig. 7.3 it seems that higher splittings between the A and B free excitons correspond to lower deviations of the thermal activation energy from the binding energy. In addition, the spectral distance between the BE and the A FE is ~4.6 and 5.8 meV for $CuInS_2$ and $CuGaSe_2$, respectively whereas the highest energy component of the M1 exciton is only separated by ~0.7 meV from the A FE and ~ 4.2 meV from the B FE in $CuInSe_2$. The small energetic separation between the A and B FE and the close proximity of the first BE could influence the thermal quenching of the FE PL lines and thus be responsible for the deviation between the activation and binding energy in $CuInSe_2$. A thermal redistribution of the A excitons towards B at temperatures above 23 K was revealed in Section 4.3.2. A similar thermal redistribution of excitons from the LPB towards the UPB at temperature above 9 K was also

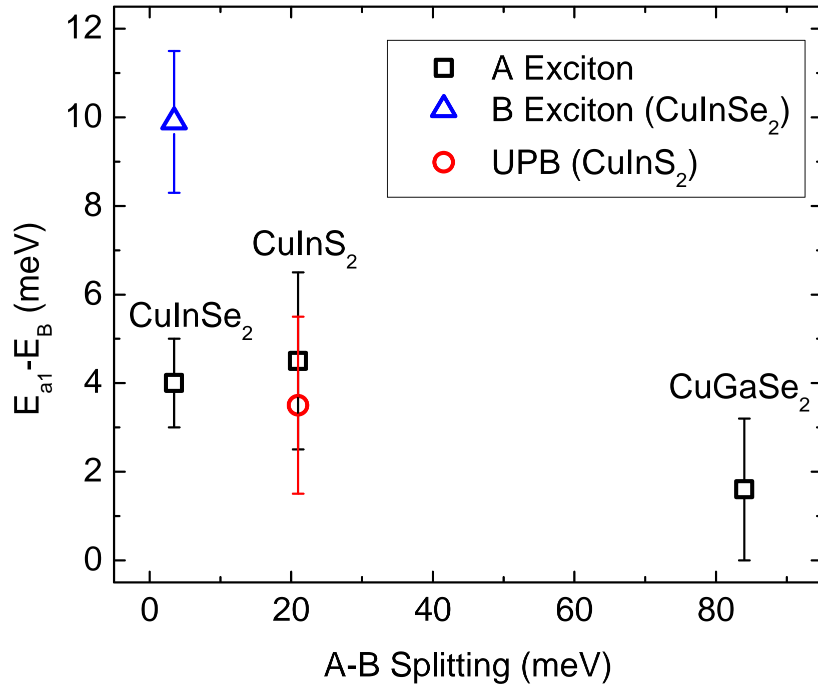

Figure 7.3: Difference between the thermal activation energy and the exciton binding energy versus the splitting between the A and B free exciton in $CuInSe_2$, $CuInS_2$ and $CuGaSe_2$ obtained from low temperature RF resonances (e.g Fig. 4.1 for $CuInSe_2$, Ref. [112] for $CuInS_2$ and unpublished data for $CuGaSe_2$).

observed in $CuInS_2$ in Section 5.3.2. In addition, bound excitons were suggested to thermally redistribute towards the FE in $CuInSe_2$ and $CuInS_2$ in Sections 4.3.2 and 5.3.2, respectively.

Thermal activation energies for the M1, M2 and M3 bound excitons in $CuInSe_2$ have also been determined in Section 4.3.2 and the assignment of the holes involved in the exciton formation was suggested. A similar analysis was performed for $CuInS_2$ and the activation energies for the 2, 5, 6 and 8 bound exciton were presented in Section 5.3.2. The activation energy of the bound exciton line in $CuGaSe_2$ was determined in Section 6.3.2.

7.2.3 Temperature Dependence of the FWHM

The study of the temperature dependence of the FWHM can be used to obtain information about the dominant scattering processes and offers the possibility to quantitatively determine their contribution (see Section 2.4.1). Table 7.4 shows the comparison of the inhomogeneous broadening parameter and coupling strengths of the exciton-acoustic-phonon interactions for the three chalcopyrite compounds. The largest inhomogeneous broadening was observed for

Compound	$\mathbf{\Gamma_0}$ (meV)	$\mathbf{\Gamma_a}$ μ**eV/K**	$\mathbf{\Gamma_{LO}}$ **(meV)**
$CuInSe_2$	1.30±0.02	15±3	
$CuInS_2$	1.94±0.02 (A), 1.3 ± 0.3 (UPB) and 0.5 ± 0.1 (LPB)	22±2	
$CuGaSe_2$	2.8±0.2	9±5	24±5

Table 7.4: Inhomogeneous broadening parameter, coupling strengths of the exciton-acoustic-phonon interactions and optical phonon energies determined from the temperature dependence of the FWHM of the FE PL lines for the three chalcopyrite compounds $CuInSe_2$, $CuInS_2$ (spectrum (a) for the A FE and (c) for the UPB and LPB PL line in Fig. 5.2) and $CuGaSe_2$.

$CuGaSe_2$ which suggests that scattering of excitons by defects and impurities, which was already indicated by the Gaussian exciton line shape in Section 6.1, is high in this compound compared to $CuInSe_2$ and $CuInS_2$. As shown in the Table 7.4 the highest coupling strength Γ_a was obtained for $CuInS_2$ whereas the coupling strengths for $CuInSe_2$ and $CuGaSe_2$ are similar within their error intervals. Exciton-acoustic-phonon coupling strengths of 15 and 13.7 μeV/K have been observed for GaN [68] and CdTe/CdMnTe [69] multi-quantum well structures, respectively, which are similar to those observed for the three chalcopyrite compounds.

In addition, a value of the optical phonon energy has been determined for $CuGaSe_2$ which is in very good agreement with the values determined from the fit of the temperature evolution of the spectral position in $CuGaSe_2$ and $CuInSe_2$ and reported in literature [126].

7.3 Magneto-Photoluminescence

The results of the Magneto-PL measurements of the A free exciton of the three examined chalcopyrite compounds $CuInSe_2$, $CuInS_2$ and $CuGaSe_2$ are summarised in Table 7.5. For $CuInS_2$ the diamagnetic shift rate was determined to be $4.00\text{x}10^{-6}$ eV/T^2 which is smaller than that found in $CuGaSe_2$ and $CuInSe_2$ and can be explained by the small Bohr radius a_B of the free A exciton. The estimated diamagnetic shift rate of $CuGaSe_2$ falls between those of $CuInSe_2$ and $CuInS_2$ in accordance with its intermediate value of the Bohr radius.

From the diamagnetic shift rates (the average has been used for $CuInSe_2$),the reduced masses of the excitons have been calculated using a first order perturbation approach introduced in Section 2.5. Using the values of the reduced masses, the excitonic Rydberg energies, Bohr radii and effective hole masses have been

determined and are shown in Table 7.5.
The largest Rydberg energy was found for $CuInS_2$ which is in agreement with the small value of the Bohr radius of the excitons. In contrast, $CuInSe_2$ has the smallest Rydberg energy but the largest Bohr radius of the three chalcopyrite semiconductors. The values of the Rydberg energy and Bohr radius of the three compounds are in agreement with those reported in literature [31, 111, 121].
In addition, the diamagnetic shifts of the A and B free exciton lines in the PL spectra of $CuInSe_2$ single crystals reveal a considerable difference for magnetic fields applied perpendicular and parallel to the z-direction of the chalcopyrite lattice. The exciton reduced masses were calculated within the low field approximation. The A free exciton reduced mass demonstrates a strong anisotropy whereas that of the B free exciton reduced mass is weaker and inverted.

Compound	$\mathbf{c_d (eV/T^2)}$	$\mu/\mathbf{m_0}$	$\mathbf{Ry^*}$ **(meV)**	$\mathbf{a_B}$ **(nm)**	$\mathbf{m_h/m_0}$
$CuInSe_2$	2.68 x10^{-5}	0.081	9.5	7.0	0.78
$CuInS_2$	4.00x10^{-6}	0.147	19.2	3.7	1.76
$CuGaSe_2$	9.82x10^{-6}	0.115	12.9	5.1	0.64

Table 7.5: Effective Rydberg Ry^*, Bohr radius a_B, effective hole mass m_h, and reduced mass μ of the free A exciton calculated from the rate of the diamagnetic shift c_d for the three chalcopyrite compounds $CuInSe_2$, $CuInS_2$ and $CuGaSe_2$.

The effective mass of charge carriers is a fundamental concept in solid physics. Its values and anisotropy have an important influence on important parameters such as the charge carrier mobility, conductivity and density of states. As mentioned in Chapter 1 the conversion efficiency is influenced by the semiconductor band gap as well as by material properties such as the diffusion coefficients and the effective densities of states in the conduction and valence band. These material properties depend on the value of the effective mass of the charge carriers. Therefore an anisotropy of the effective hole mass as observed for $CuInSe_2$ has a profound influence on such material properties.
Among the materials studied in this work, thin-film solar cells based on $CuIn_{1-x}Ga_xSe_2$ have shown the highest efficiencies as reported in literature. Knowing the properties of the end point ternaries of the compositional range of $CuIn_{1-x}Ga_xSe_2$ i.e. $CuInSe_2$ and $CuGaSe_2$ can facilitate the understanding of the material properties of the quaternary compound with x varying between 0 and 1.
In contrast, solar cells based on $CuInSe_2$ and $CuInS_2$ demonstrated efficiencies of about 14 and 12 %, respectively, which is lower than that of the 20 % reported for

$CuIn_{1-x}Ga_xSe_2$. The band gap of $CuInS_2$ has already an optimum value of about 1.5 eV. However, alloying with gallium has shown promising results towards an increase in efficiency [2].

7.4 Future Work

In order to further improve the efficiencies of CIGS/CIS thin-film solar cells more research on the material properties is needed. The anisotropy in $CuInS_2$ and $CuGaSe_2$ could be studied and compared with the theoretically predicted values [46]. The quality of the $CuInS_2$ crystal studied in this work would be sufficient for this analysis whereas the width of the free exciton PL line in $CuGaSe_2$ could be too large. At the same time information about the excitonic Zeeman splitting could be obtained and a theoretical model is needed to explain their splitting. A model to explain the Zeeman splitting of the free excitons in $CuInSe_2$ is currently being developed by Dr. Anna Rodina. This model could then be extended to $CuInS_2$ and $CuGaSe_2$. In addition, the Zeeman splitting of the bound excitons in conjunction with a theoretical model could reveal more information on their nature. This analysis would simplify the assignment of lower energy PL peaks to phonon replica of certain bound excitons. $CuGaSe_2$ single crystal or epitaxial films of improved quality could facilitate the excitation power and temperature dependent analysis as well as the analysis of the magneto PL. Values for the effective hole masses have been determined from the analysis of the diamagnetic shift. Values of the effective electron masses could be determined from optical spectrocopy of Landau levels in the three chalcopyrites.

Further studies on the optical properties of actual CIGS/CIS solar cells could be conducted. Similar work has been performed on CIGS on polyimide [13] and could be extended to $CuInSe_2$, $CuInS_2$, $CuGaSe_2$ and CIGS solar cells on glass or alternative substrates. The influence of growth parameters or new technological processes on the luminescence could be studied and the optical properties of these cells can then be correlated with the photovoltaic parameters of solar cells.

In future techniques such as those used in this thesis should be employed to study potential new absorber materials. One example is $Cu_2ZnSn(Se,S)_4$, which has recently attracted a lot of attention as an alternative to CIGS for thin-film solar absorber layers due to the absence of indium. Record efficiencies of 10.1 %

have been reported for $Cu_2ZnSn(Se,S)_4$ based devices [128]. So far there are only a few reports on the excitonic emission in this material [129, 130] due to its low quality. Optical spectroscopy of higher quality material could provide the opportunity of determining fundamental material properties and therefore accelerate the progress of $Cu_2ZnSn(Se,S)_4$-based technologies.

Bibliography

[1] J. A. M. AbuShama, S. Johnston, T. Moriarty, G. Teeter, K. Ramanathan, and R. Noufi, "Properties of ZnO/CdS/$CuInSe_2$ solar cells with improved performance," *Progress in Photovoltaics*, vol. 12, p. 39, 2004.

[2] R. Klenk, J. Klaer, R. Scheer, M. C. Lux-Steiner, I. Luck, N. Meyer, and U. Ruhle, "Solar cells based on $CuInS_2$ - an overview," *Thin Solid Films*, vol. 480, p. 509, 2005.

[3] D. L. Young, J. Keane, A. Duda, J. A. M. AbuShama, C. L. Perkins, M. Romero, and R. Noufi, "Improved performance in ZnO/CdS/$CuGaSe_2$ thin-film solar cells," *Progress in Photovoltaics*, vol. 11, p. 535, 2003.

[4] P. Jackson, D. Hariskos, E. Lotter, S. Paetel, R. Wuerz, R. Menner, W. Wischmann, and M. Powalla, "New world record efficiency for Cu(In,Ga)Se_2 thin-film solar cells beyond 20%," *Progress in Photovoltaics: Research and Applications*, vol. 19, p. 894, 2011.

[5] S. Irvine, *Solar Cells and Photovoltaics.* Springer Handbook of Electronic and Photonic Materials, Springer-Verlag US, 2007.

[6] D. A. Neamen, *Semiconductor Physics and Devices.* Boston: McGraw-Hill Higher Education, 3rd ed., 2003.

[7] S. M. Sze, *Physics of semiconductor devices.* John Wiley and Sons Inc., 1981.

[8] C. H. Henry, "Limiting efficiencies of ideal single and multiple energy-gap terrestrial solar-cells," *Journal of Applied Physics*, vol. 51, p. 4494, 1980.

[9] M. A. Green, K. Emery, Y. Hishikawa, W. Warta, and E. D. Dunlop, "Solar cell efficiency tables (version 39)," *Progress in Photovoltaics*, vol. 20, p. 12, 2012.

[10] D. M. Bagnall and M. Boreland, "Photovoltaic technologies," *Energy Policy*, vol. 36, p. 4390, 2008.

[11] U. Rau and H. W. Schock, "Electronic properties of Cu(In,Ga)Se_2 heterojunction solar cells-recent achievements, current understanding, and future challenges," *Applied Physics A*, vol. 69, p. 131, 1999.

[12] A. Chirila, S. Buecheler, F. Pianezzi, P. Bloesch, C. Gretener, A. R. Uhl, C. Fella, L. Kranz, J. Perrenoud, S. Seyrling, R. Verma, S. Nishiwaki, Y. E. Romanyuk, G. Bilger, and A. N. Tiwari, "Highly efficient Cu(In,Ga)Se_2 solar cells grown on flexible polymer films," *Nature Materials*, vol. 10, p. 857, 2011.

[13] H. Zachmann, S. Puttnins, M. V. Yakushev, F. Luckert, R. W. Martin, A. V. Karotki, V. F. Gremenok, and A. V. Mudryi, "Fabrication and characterisation of Cu(In,Ga)Se_2 solar cells on polyimide," *Thin Solid Films*, vol. 519, p. 7264, 2011.

[14] J. R. Tuttle, A. Szalaj, and J. Keane, "A 15.2 % amo/1433 w/kg thin-film Cu(In,Ga)Se_2 solar cell for space applications," in *Photovoltaic Specialists Conference. Conference Record of the Twenty-Eighth IEEE*, p. 1042, 2000.

[15] W. Shockley and H. J. Queisser, "Detailed balance limit of efficiency of p-n junction solar cells," *Journal of Applied Physics*, vol. 32, p. 510, 1961.

[16] S. B. Zhang, S.-H. Wei, A. Zunger, and H. Katayama-Yoshida, "Defect physics of the $CuInSe_2$ chalcopyrite semiconductor," *Physical Review B*, vol. 57, p. 9642, 1998.

[17] C. Rincon and R. Marquez, "Defect physics of the $CuInSe_2$ chalcopyrite semiconductor," *Journal of Physics and Chemistry of Solids*, vol. 60, p. 1865, 1999.

[18] J. J. M. Binsma, L. J. Giling, and J. Bloem, "Luminescence of $CuInS_2$: 1. the broad-band emission and its dependence on the defect chemistry," *Journal of Luminescence*, vol. 27, p. 35, 1982.

[19] S. Siebentritt and U. Rau, "Shallow defects in the wide gap chalcopyrite $CuGaSe_2$ wide-gap chalcopyrites," vol. 86 of *Springer Series in Materials Science*, p. 113, Springer Berlin Heidelberg, 2006.

[20] P. Yu, "Radiative recombination in melt-grown and Cd-implanted $CuInSe_2$," *Journal of Applied Physics*, vol. 47, p. 677, 1976.

[21] F. Abou-Elfotouh, H. Moutinho, A. Bakry, T. Coutts, and L. Kazmerski., "Characterization of the defect levels in copper indium diselenide," *Solar Cells*, vol. 30, p. 151, 1991.

[22] C. Rincon, J. Gonzalez, and G. Sanchez Perez, "Luminescence and impurity states in $CuInSe_2$," *Journal of Applied Physics*, vol. 54, p. 6634, 1983.

[23] P. Migliorato, J. L. Shay, H. M. Kasper, and W. Sigurd, "Analysis of the electrical and luminescent properties of $CuInSe_2$," *Journal of Applied Physics*, vol. 46, p. 1777, 1975.

[24] J. Krustok, H. Collan, M. Yakushev, and K. Hjelt, "The role of spatial potential fluctuations in the shape of the PL bands of multinary semiconductor compounds," *Physica Scripta*, vol. T79, p. 179, 1999.

[25] D. G. Thomas and J. J. Hopfield, "Exciton spectrum of cadmium sulfide," *Physical Review*, vol. 116, p. 573, 1959.

[26] J. J. M. Binsma, L. J. Giling, and J. Bloem, "Luminescence of $CuInS_2$: 2. exciton and near edge emission," *Journal of Luminescence*, vol. 27, p. 55, 1982.

[27] S. Chatraphorn, K. Yoodee, P. Songpongs, C. Chityuttakan, K. Sayavong, S. Wongmanerod, and P. O. Holtz, "Photoluminescence of a high quality $CuInSe_2$ single crystal," *Japanese Journal of Applied Physics Part 2-Letters*, vol. 37, p. L269, 1998.

[28] J. H. Schön and E. Bucher, "Excitonic luminescence in $CuInSe_2$," *Applied Physics Letters*, vol. 73, p. 211, 1998.

[29] C. Rincon, S. M. Wasim, E. Hernandez, M. A. Arsene, F. Voillot, J. P. Peyrade, G. Bacquet, and A. Albacete, "Photoluminescence in p-type $CuInSe_2$ single crystals," *Journal of Physics and Chemistry of Solids*, vol. 59, p. 245, 1998.

[30] A. V. Mudriy, I. V. Bodnar, I. A. Viktorov, V. F. Gremenok, M. V. Yakushev, R. D. Tomlinson, A. E. Hill, and R. D. Pilkington, "Optical properties of high-quality $CuInSe_2$ single crystals," *Applied Physics Letters*, vol. 77, p. 2542, 2000.

[31] A. Bauknecht, S. Siebentritt, J. Albert, Y. Tomm, and M. C. Lux-Steiner, "Excitonic photoluminescence from $CuGaSe_2$ single crystals and epitaxial layers: Temperature dependence of the band gap energy," *Japanese Journal of Applied Physics*, vol. 39, p. 322, 2000.

[32] A. Yamada, Y. Makita, S. Niki, A. Obara, P. Fons, H. Shibata, M. Kawai, S. Chichibu, and H. Nakanishi, "Band-edge photoluminescence of $CuGaSe_2$ films grown by molecular beam epitaxy," *Journal of Applied Physics*, vol. 79, p. 4318, 1996.

[33] M. V. Yakushev, A. V. Mudryi, I. V. Victorov, J. Krustok, and E. Mellikov, "Energy of excitons in $CuInS_2$ single crystals," *Applied Physics Letters*, vol. 88, p. 011922, 2006.

[34] A. Meeder, A. Jager-Waldau, V. Tezlevan, E. Arushanov, T. Schedel-Niedrig, and M. C. Lux-Steiner, "Temperature dependence of the exciton gap in monocrystalline $CuGaSe_2$," *Journal of Physics-Condensed Matter*, vol. 15, p. 6219, 2003.

[35] M. V. Yakushev, R. W. Martin, and A. V. Mudryi, "Temperature dependence of excitonic emission in $CuInSe_2$," *Physica Status Solidi C*, vol. 6, p. 1082, 2009.

[36] J. L. Shay and J. H. Wernick, *Ternary Chalcopyrite Semiconductors: Growth, Electronic Properties, and Applications*, vol. 7 of *International series of monographs in the science of the solid state.* New York: Pergamon Press, 1975.

[37] J. E. Jaffe and A. Zunger, "Theory of the band-gap anomaly in ABC_2 chalcopyrite semiconductors," *Physical Review B*, vol. 29, p. 1882, 1984.

[38] H. Hahn, G. Frank, W. Klingler, A. D. Meyer, and G. Storger, "Untersuchungen uber ternare chalkogenide: 5. Uber einige ternare chalkogenide mit chalkopyritstruktur," *Zeitschrift Fur Anorganische Und Allgemeine Chemie*, vol. 271, p. 153, 1953.

[39] H. W. Spiess, U. Haeberle, G. Brandt, A. Rauber, and Schneide.J, "Nuclear magnetic-resonance in I-III-VI_2 semiconductors," *Physica Status Solidi B*, vol. 62, p. 183, 1974.

[40] S. C. Abrahams and J. l. Bernstein, "Piezoelectric nonlinear optic $CuGaSe_2$ and $CdGeAs_2$ - crystal-structure, chalcopyrite microhardness, and sublattice distortion," *Journal of Chemical Physics*, vol. 61, p. 1140, 1974.

[41] S. C. Abrahams and J. l. Bernstein, "Piezoelectric nonlinear optic $CuGaS_2$ and $CuInS_2$ crystal-structure - sublattice distortion in $A^IB^{III}C_2^{VI}$ and $A^{II}B^{IV}C_2^V$ type chalcopyrites," *Journal of Chemical Physics*, vol. 59, p. 5415, 1973.

[42] J. Parkes, R. D. Tomlinso, and M. J. Hampshir, "Crystal data for $CuInSe_2$," *Journal of Applied Crystallography*, vol. 6, p. 414, 1973.

[43] J. J. Hopfield, "Fine structure in the optical absorption edge of anisotropic crystals," *Journal of Physics and Chemistry of Solids*, vol. 15, p. 97, 1960.

[44] J. E. Rowe and J. L. Shay, "Extension of the quasicubic model to ternary chalcopyrite crystals," *Physical Review B*, vol. 3, p. 451, 1971.

[45] J. L. Shay and B. Tell, "Energy band structure of I-III-VI_2 semiconductors," *Surface Science*, vol. 37, p. 748, 1973.

[46] C. Persson, "Anisotropic hole-mass tensor of $CuIn_{1-x}Ga_x(S,Se)_2$: Presence of free carriers narrows the energy gap," *Applied Physics Letters*, vol. 93, p. 072106, 2008.

[47] J. L. Shay and H. M. Kasper, "Direct observation of Cu d levels in I-III-VI_2 compounds," *Physical Review Letters*, vol. 29, p. 1162, 1972.

[48] J. L. Shay, B. Tell, H. M. Kasper, and L. M. Schiavone, "Electronic structure of $AgInSe_2$ and $CuInSe_2$," *Physical Review B*, vol. 7, p. 4485, 1973.

[49] B. Tell and P. M. Bridenbaugh, "Aspects of band-structure of $CuGaS_2$ and $CuGaSe_2$," *Physical Review B*, vol. 12, p. 3330, 1975.

[50] K. Yoodee, J. C. Woolley, and V. Sa-yakanit, "Effects of p-d hybridization on the valence band of I-III-VI_2 chalcopyrite semiconductors," *Physical Review B*, vol. 30, p. 5904, 1984.

[51] J. E. Jaffe and A. Zunger, "Anion displacements and the band-gap anomaly in ternary ABC_2 chalcopyrite semiconductors," *Physical Review B*, vol. 27, p. 5176, 1983.

[52] P. Y. Yu and M. Cardona, *Fundamentals of Semiconductors*. Berlin Heidelberg New York: Springer-Verlag, 3rd ed., 2005.

[53] P. J. Dean and D. C. Herbert, *Bound Excitons in Semiconductors*. Excitons, Berlin Heidelberg New York: Springer-Verlag, 1979.

[54] C. F. Klingshirn, *Semiconductor Optics*. Berlin Heidelberg New York: Springer-Verlag, 1995.

[55] H. Ibach and H. Lüth, *Festkörperphysik*, vol. 7. Berlin Heidelberg: Springer-Lehrbuch, 2009.

[56] M. A. Gilleo, P. T. Bailey, and D. E. Hill, "Free-carrier and exciton recombination radiation in GaAs," *Physical Review*, vol. 174, p. 898, 1968.

[57] E. W. Williams and H. B. Bebb, *Transport and Optical Phenomena*, vol. 8 of *Semiconductor and Semimetals*. New York: Academics, 1972.

[58] J. R. Haynes, "Experimental proof of the existence of a new electronic complex in silicon," *Physical Review Letters*, vol. 4, p. 361, 1960.

[59] J. J. Hopfield, "The quantum chemistry of bound exciton complexes," in *Physics of Semiconductors*, vol. 7, (Paris), 1964.

[60] R. R. Sharma, "Binding energy of the excitonic molecule," *Physical Review*, vol. 170, p. 770, 1968.

[61] J. R. Haynes, "Experimental observation of the excitonic molecule," *Physical Review Letters*, vol. 17, p. 860, 1966.

[62] R. R. Sharma and S. Rodriguez, "Theory of excitons bound to ionized impurities in semiconductors," *Physical Review*, vol. 153, p. 823, 1967.

[63] H. Atzmuller, F. Froschl, and U. Schroder, "Theory of excitons bound to neutral impurities in polar semiconductors," *Physical Review B*, vol. 19, p. 3118, 1979.

[64] J. J. Pankove, *Optical Processes in Semiconductors*. Courier Dover Publications, 1971.

[65] B. Gil, P. Bigenwald, P. P. Paskov, and B. Monemar, "Internal structure of acceptor-bound excitons in wide-band-gap wurtzite semiconductors," *Physical Review B*, vol. 81, p. 085211, 2010.

[66] M. Fox, *Optical Properties of Solids*. Oxford University Press, 2nd ed., 2010.

[67] Y. Toyozawa, "Theory of line-shapes of the exciton absorption bands," *Progress of Theoretical Physics*, vol. 20, p. 53, 1958.

[68] K. P. Korona, A. Wysmolek, K. Pakula, R. Stepniewski, J. M. Baranowski, I. Grzegory, B. Lucznik, M. Wroblewski, and S. Porowski, "Exciton region reflectance of homoepitaxial GaN layers," *Applied Physics Letters*, vol. 69, p. 788, 1996.

[69] R. Hellmann, M. Koch, J. Feldmann, S. T. Cundiff, E. O. Gobel, D. R. Yakovlev, A. Waag, and G. Landwehr, "Homogeneous linewidth of excitons in semimagnetic CdTe/$Cd_{1-X}Mn_x$Te multiple-quantum wells," *Physical Review B*, vol. 48, p. 2847, 1993.

[70] M. O'Neill, M. Oestreich, W. W. Ruhle, and D. E. Ashenford, "Exciton radiative decay and homogeneous broadening in CdTe/$Cd_{0.85}Mn_{0.15}$Te multiple-quantum wells," *Physical Review B*, vol. 48, p. 8980, 1993.

[71] M. Leroux, N. Grandjean, B. Beaumont, G. Nataf, F. Semond, J. Massies, and P. Gibart, "Temperature quenching of photoluminescence intensities in undoped and doped GaN," *Journal of Applied Physics*, vol. 86, p. 3721, 1999.

[72] D. Bimberg, M. Sondergeld, and E. Grobe, "Thermal dissociation of excitons bounds to neutral acceptors in high-purity GaAs," *Physical Review B*, vol. 4, p. 3451, 1971.

[73] T. Gühne, Z. Bougrioua, M. Nemoz, R. Chmielowski, T. Bretagnon, B. Gil, and M. Leroux, "Polarized photoluminescence from nonpolar (11-20) (Ga,In)n multi-quantum-wells," in *29th International Conference on the Physics of Semiconductors* (M. J. Caldas and N. Studart, eds.), vol. 1199, (Brazil), p. 191, American Institute of Physics, 2008.

[74] T. Schmidt, K. Lischka, and W. Zulehner, "Excitation-power dependence of the near-band-edge photoluminescence of semiconductors," *Physical Review B*, vol. 45, p. 8989, 1992.

[75] P. C. Makado and N. C. Mcgill, "Energy-levels of a neutral hydrogen-like system in a constant magnetic-field of arbitrary strength," *Journal of Physics C-Solid State Physics*, vol. 19, p. 873, 1986.

[76] S. Taguchi, T. Goto, M. Takeda, and G. Kido, "Magneto-optical effects of the wannier exciton in a biaxial ZnP_2 crystal. I," *Journal of the Physical Society Japan*, vol. 57, p. 3256, 1988.

[77] J. J. Hopfield, "Theory of the contribution of excitons to the complex dielectric constant of crystals," *Physical Review*, vol. 112, p. 1555, 1958.

[78] F. Askary and P. Y. Yu, "Polariton luminescence and additional boundary conditions: comparison between theory and experiment," *Solid State Communications*, vol. 47, p. 241, 1983.

[79] A. V. Mudryi, A. V. Karotki, M. V. Yakushev, and R. W. Martin, "Photoluminescence of $CuInS_2$ single crystals grown by traveling heater and chemical vapor transport methods," *Journal of Applied Spectroscopy*, vol. 76, p. 215, 2009.

[80] R. Stepniewski, K. P. Korona, A. Wysmolek, J. M. Baranowski, K. Pakula, M. Potemski, G. Martinez, I. Grzegory, and S. Porowski, "Polariton effects in reflectance and emission spectra of homoepitaxial GaN," *Physical Review B*, vol. 56, p. 15151, 1997.

[81] Y. Toyozawa, "On the dynamical behaviour of an exciton," *Progress Theoretical Physics Supplement*, vol. 12, p. 111, 1959.

[82] T. Steiner, M. L. W. Thewalt, E. S. Koteles, and J. P. Salerno, "Effect of neutral donor scattering on the time-dependent exciton-polariton photoluminescence line-shape in GaAs," *Physical Review B*, vol. 34, p. 1006, 1986.

[83] R. D. Tomlinson, "Fabrication of $CuInSe_2$ single-crystals using melt-growth techniques," *Solar Cells*, vol. 16, p. 17, 1986.

[84] P. Gille, U. Rossner, N. Puhlmann, H. Niebsch, and T. T. Piotrowski, "Growth of $Hg_{1-X}Mn_xTe$ crystals by the traveling heater method," *Semiconductor Science and Technology*, vol. 10, p. 353, 1995.

[85] H. Miyake and K. Sugiyama, "Single-crystal growth of Cu-III-VI_2 semiconductors by THM," *Japanese Journal of Applied Physics Part 1*, vol. 32, p. 156, 1993.

[86] B. E. Warren, *X-Ray Diffraction.* Dover Pulications, 1990.

[87] E. Preuss, B. Krahl-Urban, R. Butz, and K. Julich, *Laue Atlas.* John Wiley and Sons, 1974.

[88] N. Instruments, *ENERGY-DISPERSIVE X-RAY MICROANALYSIS-An Introduction.* Middleton, Wisconsin: NORAN Instruments, 1999.

[89] J. I. Goldstein, D. Newbury, D. Joy, C. Lyman, P. Echlin, E. Lifshin, L. Sawyer, and J. Michael, *Scanning electron microscopy and x-ray microanalysis.* Springer Science, 2003.

[90] F. Luckert, M. V. Yakushev, C. Faugeras, A. V.Karotki, A. V. Mudryi, and R. W. Martin, "Excitation power and temperature dependence of excitons in $CuInSe_2$," *accepted for publication in Journal of Applied Physics*, 2012.

[91] M. V. Yakushev, F. Luckert, A. V. Rodina, C. Faugeras, A. V. Karotki, A. V. Mudryi, and R. W. Martin, "Anisotropy of effective masses in $CuInSe_2$," *in preparation*, 2012.

[92] M. V. Yakushev, Y. Feofanov, R. W. Martin, R. D. Tomlinson, and A. Mudryi, "Magneto-photoluminescence study of radiative recombination in $CuInSe_2$ single crystals," *Journal of Physics and Chemistry of Solids*, vol. 64, p. 2011, 2003.

[93] K. Wakita, Y. Ohta, and N. Ohgushi, "Time-resolved emission in $CuInS_2$ under high excitation," *Thin Solid Films*, vol. 509, p. 154, 2006.

[94] H. Tanino, T. Maeda, H. Fujikake, H. Nakanishi, S. Endo, and T. Irie, "Raman-spectra of $CuInSe_2$," *Physical Review B*, vol. 45, p. 13323, 1992.

[95] J. Weber, W. Schmid, and R. Sauer, "Localized exciton bound to an isoelectronic trap in silicon," *Physical Review B*, vol. 21, p. 2401, 1980.

[96] J. J. Hopfield, D. G. Thomas, and R. T. Lynch, "Isoelectronic donors and acceptors," *Physical Review Letters*, vol. 17, p. 312, 1966.

[97] J. Krustok, J. Raudoja, and R. Jaaniso, "Temperature dependence of very deep emission from an exciton bound to an isoelectronic defect in polycrystalline $CuInS_2$," *Applied Physics Letters*, vol. 89, 2006.

[98] K. P. O'Donnell and X. Chen, "Temperature dependence of semiconductor band gaps," *Applied Physics Letters*, vol. 58, p. 2924, 1991.

[99] P. Deus, H. Neumann, G. Kuhn, and B. Hinze, “Low-temperature thermal expansion in $CuInSe_2$,” *Physica Status Solidi A*, vol. 80, p. 205, 1983.

[100] A. Nagaoka, K. Yoshino, T. Taniyama, and H. Miyake, “Peculiarities of linear thermal expansion of $CuInS_2$ single crystals,” *Japanese Journal of Applied Physics*, vol. 50, 2011.

[101] Y. H. Cho, G. H. Gainer, A. J. Fischer, J. J. Song, S. Keller, U. K. Mishra, and S. P. DenBaars, “"S-shaped" temperature-dependent emission shift and carrier dynamics in InGaN/GaN multiple quantum wells,” *Applied Physics Letters*, vol. 73, p. 1370, 1998.

[102] A. Bell, S. Srinivasan, C. Plumlee, H. Omiya, F. A. Ponce, J. Christen, S. Tanaka, A. Fujioka, and Y. Nakagawa, “Exciton freeze-out and thermally activated relaxation at local potential fluctuations in thick $Al_xGa_{1-x}N$ layers,” *Journal of Applied Physics*, vol. 95, p. 4670, 2004.

[103] M. V. Yakushev, F. Luckert, C. Faugeras, A. V. Karotki, A. V. Mudryi, and R. W. Martin, “Excited states of the free excitons in $CuInSe_2$ single crystals,” *Applied Physics Letters*, vol. 97, 2010.

[104] H. Zimmermann, R. Boyn, and K. Piel, “Thermal quenching of bound exciton emission due to phonon-induced nonradiative-transitions - experimental-data for CdTe and InP,” *Journal of Physics-Condensed Matter*, vol. 4, p. 859, 1992.

[105] H. Weinert, H. Neumann, H. J. Hobler, G. Kuhn, and N. Vannam, “Ir faraday-effect in n-type $CuInSe_2/InSe_2$,” *Physica Status Solidi B*, vol. 81, p. K59, 1977.

[106] T. Irie, S. Endo, and S. Kimura, “Electrical-properties of p-type and n-type $CuInSe_2$ single-crystals,” *Japanese Journal of Applied Physics*, vol. 18, p. 1303, 1979.

[107] V. Riede, H. Sobotta, H. Neumann, H. X. Nguyen, W. Moller, and G. Kuhn, “Infrared lattice vibration-spectra of $CuInSe_2$ and $CuGaTe_2$,” *Solid State Communications*, vol. 28, p. 449, 1978.

[108] E. Arushanov, L. Essaleh, J. Galibert, J. Leotin, M. A. Arsene, J. P. Peyrade, and S. Askenazy, “Shubnikov-De Haas oscillations in n-$CuInSe_2$,” *Applied Physics Letters*, vol. 61, p. 958, 1992.

[109] S. M. Wasim, L. Essaleh, C. Rincon, G. Marin, J. Galibert, and J. Leotin, "Density of states effective mass of n-type $CuInSe_2$ from the temperature dependence of hall coefficient in the activation regime," *Journal of Physics and Chemistry of Solids*, vol. 66, p. 1887, 2005.

[110] H. Neumann, H. Sobotta, W. Kissinger, V. Riede, and G. Kuhn, "Hole effective masses in $CuInSe_2$," *Physica Status Solidi B*, vol. 108, p. 483, 1981.

[111] M. V. Yakushev, R. W. Martin, A. Babinski, and A. V. Mudryi, "Effects of magnetic fields on free excitons in $CuInSe_2$," *Physica Status Solidi C*, vol. 6, p. 1086, 2009.

[112] M. V. Yakushev, R. W. Martin, A. V. Mudryi, and A. V. Ivaniukovich, "Excited states of the a free exciton in $CuInS_2$," *Applied Physics Letters*, vol. 92, 2008.

[113] A. V. Mudryi, A. V. Ivanyukovich, M. V. Yakushev, R. Martin, and A. Saad, "Optical spectroscopy of free excitons in a $CuInS_2$ chalcopyrite semiconductor compound," *Semiconductors*, vol. 42, p. 29, 2008.

[114] K. Yoshino, T. Ikari, S. Shirakata, H. Miyake, and K. Hiramatsu, "Sharp band edge photoluminescence of high-purity $CuInS_2$ single crystals," *Applied Physics Letters*, vol. 78, p. 742, 2001.

[115] S. Shirakata and H. Miyake, "Photoreflectance of $CuInS_2$ single crystal prepared by traveling heater method," *Journal of Physics and Chemistry of Solids*, vol. 64, p. 2021, 2003.

[116] B. Tell, J. L. Shay, and H. M. Kasper, "Electroreflectance and absorption-edge studies of $AgGaS_2$ and $AgGaSe_2$," *Physical Review B*, vol. 6, p. 3008, 1972.

[117] H. Murotani, T. Kuronaka, Y. Yamada, T. Taguchi, N. Okada, and H. Amano, "Temperature dependence of excitonic transitions in a-plane AlN epitaxial layers," *Journal of Applied Physics*, vol. 105, 2009.

[118] P. W. Yu, W. J. Anderson, and Y. S. Park, "Anomalous temperature dependence of the energy gap of $AgGaS_2$," *Solid State Communications*, vol. 13, p. 1883, 1973.

[119] S. Ozaki, M. Sasaki, and S. Adachi, "Positive temperature variation of the bandgap energy in $AgGaSe_2$," *Physica Status Solidi A*, vol. 203, p. 2648, 2006.

[120] K. Wakita, K. Nishi, Y. Ohta, T. Onishi, and Y. Shim, "Time-resolved emission of excitons in $CuInS_2$ crystals," *Japanese Journal of Applied Physics*, vol. 47, p. 8157, 2008.

[121] M. V. Yakushev, R. W. Martin, and A. V. Mudryi, "Diamagnetic shifts of free excitons in CuInS2 in magnetic fields," *Applied Physics Letters*, vol. 94, 2009.

[122] F. Luckert, M. V. Yakushev, C. Faugeras, A. V. Karotki, A. V. Mudryi, and R. W. Martin, "Diamagnetic shift of the a free exciton in $CuGaSe_2$ single crystals," *Applied Physics Letters*, vol. 97, 2010.

[123] A. Meeder, D. F. Marron, V. Tezlevan, E. Arushanov, A. Rumberg, T. Schedel-Niedrig, and M. C. Lux-Steiner, "Radiative recombination in CVT-grown $CuGaSe_2$ single crystals and thin films," *Thin Solid Films*, vol. 431, p. 214, 2003.

[124] A. V. Mudryi, I. V. Bodnar, V. F. Gremenok, I. A. Victorov, A. I. Patuk, and I. A. Shakin, "Free and bound exciton emission in $CuInSe_2$ and $CuGaSe_2$ single crystals," *Solar Energy Materials and Solar Cells*, vol. 53, p. 247, 1998.

[125] A. Meeder, D. F. Marron, V. Chu, J. P. Conde, A. Jager-Waldau, A. Rumberg, and M. C. Lux-Steiner, "Photoluminescence and sub band gap absorption of $CuGaSe_2$ thin films," *Thin Solid Films*, vol. 403, p. 495, 2002.

[126] C. Rincon and F. J. Ramirez, "Lattice-vibrations of $CuInSe_2$ and $CuGaSe_2$ by raman microspectrometry," *Journal of Applied Physics*, vol. 72, p. 4321, 1992.

[127] H. Kildal, "Band structure of $CdGeAs_2$ near $\mathbf{k}$=0," *Physical Review B*, vol. 10, p. 5082, 1974.

[128] D. A. R. Barkhouse, O. Gunawan, T. Gokmen, T. K. Todorov, and D. B. Mitzi, "Device characteristics of a 10.1% hydrazine-processed $Cu_2ZnSn(Se,S)_4$ solar cell," *Progress in Photovoltaics*, vol. 20, p. 6, 2012.

[129] K. Hones, E. Zscherpel, J. Scragg, and S. Siebentritt, “Shallow defects in Cu_2ZnSnS_4,” *Physica B-Condensed Matter*, vol. 404, p. 4949, 2009.

[130] F. Luckert, D. I. Hamilton, M. V. Yakushev, N. S. Beattie, G. Zoppi, M. Moynihan, I. Forbes, A. V. Karotki, A. V. Mudryi, M. Grossberg, J. Krustok, and R. W. Martin, “Optical properties of high quality $Cu_2ZnSnSe_4$ thin films,” *Applied Physics Letters*, vol. 99, 2011.